This is to certify that the

thesis entitled

**EXPERIMENTAL STUDY OF THE
2-D AND 3-D STRUCTURE OF A
CONCENTRATED LINE VORTEX ARRAY**

presented by

Douglas Gordon Bohl

has been accepted towards fulfillment
of the requirements for

Ph.D. degree in **Mechanical Engineering**

M. M. Koochesfahani
Major professor

Date **August 15, 2002**

DATE DUE	DATE DUE	DATE DUE

Experimental Study of the 2-D and 3-D Structure of a Concentrated Line Vortex Array

By

Douglas G. Bohl

A DISSERTATION
Submitted to
Michigan State University
in partial fulfillment of the requirements
for the degree of

DOCTOR OF PHILOSOPHY

Department of Mechanical Engineering
2002

ABSTRACT

EXPERIMENTAL STUDY OF THE 2-D AND 3-D STRUCTURE OF A CONCENTRATED LINE VORTEX ARRAY

By

Douglas G. Bohl

It is well know from previous work that when a two dimensional vortex interacts with a no-slip boundary flow along the axis of the vortex core, axial core flow is generated. To date, work on the generation and structure of axial core flow has been limited to mainly analytic investigation and qualitative experiments. In this work, Molecular Tagging Velocimetry (MTV) is used to provide quantitative measurements of the structure of a developing vortex array.

A NACA-0012 airfoil is pitched about the quarter chord point at varying amplitudes and frequencies to produce a semi-infinite vortex array with vortices of varying characteristics (i.e. circulation, peak vorticity, core size, etc.). Two-component MTV is used to detail the initial formation of the vortex array for the first chord length downstream of the airfoil trailing edge. MTV results combined with flow visualization images indicate that the unsteady Kutta condition is not valid for high reduced frequencies in this flow field. Mean drag results show that the mean force switches from drag to thrust as the reduced frequency is increased. The condition of zero mean drag does not occur when the vortices are aligned, as predicted by thrust calculations from the mean flow field along the tunnel midspan, but rather at a reduced frequency that is 30% higher. This difference is due to the velocity fluctuations and lateral pressure distribution p(y) in the flow field which are not accounted for when the mean profile only is used.

Cutting walls are placed into the flow field at half a chord downstream of the trailing edge to initiate axial flow within the vortex cores. A combination of line tagging (single component velocity perpendicular to the tagged line) and stereoscopic (three component velocity) MTV measurements are used to detail the interaction of the vortex array with the cutting walls. As expected the results show that axial flow is generated within the vortex core and that fluid moves away from the cutting walls. The maximum axial flow speeds are nominally equal to the maximum swirl speeds. Evidence for the presence of area varying waves is given by a local change in the vortex core area that propagates away from the cutting walls. The spatial location of the area varying waves correlates to local spikes in the peak vorticity and the axial core flow. Two wave speeds, the speed of the axial flow front and the speed of area varying waves on the vortex core, are calculated and found to increase with increasing reduced frequency. These two speeds are however different with the area varying wave increasingly lagging behind the axial flow front.

Reverse spanwise flow (i.e., flow opposite to the direction of the axial core flow) is observed outside of the vortex cores. The reverse flow indicates a large scale recirculation is set-up to return fluid towards the wall, satisfying the conservation of mass. The vortex array structure changes in character as it convects downstream. The peak vorticity level is reduced and the core radius increases. The vorticity profile changes from Gaussian to non-Gaussian. At some span locations and reduced frequencies "hollow core" vortices are observed. The vortices eventually loose coherence and the spanwise flow, initially limited to the vortex core regions (i.e. the axial core flow), is found throughout the flow field. This break-up of the vortical structures begins near the wall and propagates towards the center of the tunnel.

This book is dedicated, with love, to Coreen and Bailey who somehow managed to live and grow with me through this long strange journey. And to Noah who joined us for the final sprint.

ACKNOWLEDGEMENTS

I have found that the idea of a Ph.D. representing individual research and work to be false. No work of this magnitude could ever be accomplished without the help and support of many people. I would like to acknowledge the following people for their contributions to my "individual" work.

My local family Coreen and Bailey who kept me grounded and helped me keep my priorities straight during the maddening processes. My extended family, including but not limited to, my mom (Marilyn), dad (Gordon), brother (Dave), and mother-in-law (Sue), who gave me places to go far away from East Lansing to get away. My happy place is the family farm in Wisconsin. Thanks To Grandma and Grandpa Bohl for letting us visit and Uncle Kenny who let me clean cow stalls while on "vacation". My local friends: Amy who I could be bitter with, Darryl and Shela who let me sit in their woods during the fall, and Chuck and Elaine who have been great friends to Coreen and myself.

From "the office" I would like to thank Mike who built (and rebuilt) much of my experiment, and made my days brighter with friendly conversation. Ann and Darla from MRSEC, without whom ordering (and returning) equipment would have been a nightmare. Special thanks to Ann for keeping me involved with kids and science! Jill, who was always helpful with departmental issues. And Hu Hui and Chee Lum who provided a lot of support (technical and moral) in the lab.

Much of the experimental technique used in this work is a result of long hours of work by Chuck Gendrich and Richard Cohn. I have added to the technique, but much of the difficult work developing MTV is theirs.

Finally, thanks to Manooch. A student advisor relationship is a lot like a parent child relationship during the teen years. Thanks for being a good "dad".

TABLE OF CONTENTS

LIST OF FIGURES IX
LIST OF SYMBOLS XV

CHAPTER 1
INTRODUCTION 1

CHAPTER 2
EXPERIMENTAL METHODS 14
- 2.1 Facility 14
- 2.2 Two Component Planar Molecular Tagging Velocimetry 17
  - 2.2.1 Technique Description 17
  - 2.2.2 Optical Arrangement 19
  - 2.2.3 Imaging Details 20
  - 2.2.4 Instantaneous Planar MTV Error Estimation 25
- 2.3 Stereoscopic MTV 26
  - 2.3.1 Angular Stereoscopic Method Description 26
  - 2.3.2 Generalized Undistortion Reconstruction 28
  - 2.3.3 sMTV Acquisition / Processing 31
  - 2.3.4 sMTV Experimental Validation 34
  - 2.3.5 sMTV Optical Issues 36
  - 2.3.6 sMTV Error Estimation 36
- 2.4 Line Tagging MTV 38
  - 2.4.1 Technique Description 38
  - 2.4.2 Error Analysis 40
- 2.5 Data Acquisition 42
- 2.6 Phase Averaging 44
- 2.7 Calculation of Statistical Quantities 45

CHAPTER 3
CENTERSPAN PLANAR MEASUREMENTS, NO CUTTING WALLS 48
- 3.1 Static Airfoil Characteristics 49
- 3.2 Oscillating Airfoil 54
  - 3.2.1 Time Averaged Data 54
  - 3.2.2 Mean Force Calculation 65
  - 3.2.3 Trailing Edge Phase Averaged Data 67
  - 3.2.4 Downstream Phase-Averaged Data 71
  - 3.2.5 Vortex/Cutting Wall Initial Conditions 89

CHAPTER 4
VORTEX / SIDE-WALL INTERACTION 90
- 4.1 Vortex / End Wall Interaction 90

CHAPTER 5

VORTEX / CUTTING WALL INTERACTION 101
5.1 Line Tagging Results 103
5.2 Stereoscopic Results 111
5.2.1 Mean Flow Field, k=5.2, 11.5 113
5.2.2 Phase Averaged Flow Field, k=5.2. 126
5.2.3 Phase Averaged Flow Field, k=11.5. 137
5.2.4 Area Varying Waves on the Vortex Cores 148
CONCLUSIONS 151
REFERENCES 155

APPENDIX A

MEAN FORCE EQUATION DEVELOPMENT 159

LIST OF FIGURES

Figure 1-1: Schematic representation of flow field investigated. 2

Figure 1-2: Top view dye visualization in the flow behind a pitching NACA0012 airfoil from Koochesfahani (1989). Flow is right to left, the airfoil is upstream of the right side of the image. Flow facility side walls, not shown, were above and below the dye traces. 2

Figure 1-3: Schematic of rotational flow over a fixed solid boundary. Adapted from Figure 10-1 from Schlicting (1960). Figure courtesy of Kind Design, Inc. 5

Figure 1-4: Schematic of initial vortex array formation flow field. 10

Figure 2-1: Definition of the airfoil motion. 14

Figure 2-2: Schematic of the Turbulent Mixing and Unsteady Aerodynamics Laboratory 10,000L water tunnel at Michigan State University. Cameras A and B shown positioned for stereoscopic measurements. Camera C shown positioned for single line tagging experiments. 15

Figure 2-3: Representative example of real airfoil motion (A = 2°, k=8.6) with a comparison to programmed functionality. Difference between the real and programmed in counts. 17

Figure 2-4: Typical MTV image pairs and the resultant 2-component velocity vector field. The flow shown is from a vortex ring impacting a flat wall at normal incidence. The axis of symmetry is indicated by the dashed lines.(a) Undelayed grid imaged 1ms after the laser pulse ("undelayed" image) (b) same grid imaged 8ms later ("delayed" image) (c) velocity field derived from (a) and (b). Gendrich and Koochesfahani (1996). 18

Figure 2-5: Schematic representation of optical set-up for planar and stereoscopic MTV experiments. 19

Figure 2-6: Timing diagram for the "double shot" camera operation. Each Fsynch pulse indicates the start of a new image. 21

Figure 2-7: Mean image pattern from a SCO intensified camera. 23

Figure 2-8: Deviation from a uniform displacement, without (a) and with (b) background correction. 24

Figure 2-9: Uncertainty level in MTV planar technique for SCO intensified cameras as a function of camera gain. 26

Figure 2-10: Schematic of angular displacement stereoscopic method. Distances and angles are derived independently for each camera. 27

Figure 2-11: Sample left and right image calibration grid at z = 0. 30

Figure 2-12: Representative derivatives of mapping function, F, for the right camera, x-direction. (a) $F^1_{1,1}$, (b) $F^1_{1,2}$, (c) $F^1_{1,3}$. Distances in real units (cm, mm, inches etc.). Derivative units are (pixels) / (real distance unit). 31

Figure 2-13: Instantaneous (a) left camera, (b) right camera, and (c) combined velocity field for flow under the rotating disk. 33

Figure 2-14: Schematic of the rotating disk experiment. 34

Figure 2-15: Comparison of V_θ from stereoscopic MTV with planar reference MTV data. Data at y = -0.43 cm 35

Figure 2-16: Stereoscopic camera set-up with liquid prism. 37

Figure 2-17: Ratio of the out-of-plane and in-plane error to the correlation technique error level as a function of the camera angle, j. 38

Figure 2-18: Example of undelayed and delayed lines for a single tagged line. Delay time: 16 msec; A=2°, k= 11.5; x=0.85c, z=0.85c. 39

Figure 2-19: Intensity profiles taken from Figure 2-11, in the region spanwise displacement. Curves shown are best fit 2nd order polynomial to ± 5 data points about the peak intensity location. 40

Figure 2-20: Phase averaged spanwise flow profiles for vortex / side wall interaction. A=2°, k=2.84; x=1.27c, z=0.85c. 41

Figure 2-21: Simulation of an Oseen vortex with a Gaussian distribution of axial flow (a) and the expected measured axial velocity distribution considering equation (8) (b)....................43

Figure 2-22: Phase ordered u and v velocity components for the 2 degree, k=11 case at x=6 cm downstream of the trailing edge. Note 2 cycles are shown. 46

Figure 2-23: Sample map of experiment fields of view combined to create large data sets in phase space. 46

Figure 3-1: Mean u, v and ω_z fields for the stationary airfoil at AOA=0°, tunnel midspan. 50

Figure 3-2: Mean velocity vectors in the near wake of the static airfoil. (a) vector length proportional to velocity, (b) vector length uniform. 51

Figure 3-3: Flow visualization of recirculation bubble in the near wake of a stationary NACA-0012 airfoil at AOA=0°. 51

Figure 3-4: Profile of $\bar{u}$, $\bar{v}$ and $\bar{\omega}_z$ for the stationary airfoil at x=c/2 (a) and x=c (b), midspan. Every 3rd point shown. 53

Figure 3-5: RMS u and v fields for the stationary airfoil at AOA=0°, tunnel midspan. ..53

Figure 3-6: Mean of all phases streamwise velocity, u, field for the A = 2°, k = 0, 5.2, 5.7 and 11.5. Note scale change for k=11.5 55

Figure 3-7: Mean streamwise velocity, $\bar{u}$, for A=2° k=5.2 5.7, 11.5 at y=0. 56

Figure 3-8: Mean streamwise velocity, $\bar{u}$, and vorticity, $\bar{\omega}_z$, profiles for A=2° k=5.2 5.7, 11.5 at x=0.5c, c. 57

Figure 3-9: Schematic of the vortex orientation for the velocity deficit cases. 58

Figure 3-12: Time averaged mean v velocity field for the A = 2°, k = 0, 5.2, 5.7 and 11.5. 60

Figure 3-13: Mean spanwise vorticity, $\overline{\omega}_z$, field for the A = 2°, k = 0, 5.2, 5.7 and 11.5. 61

Figure 3-14: RMS u velocity field for the A = 2°, k = 5.2, 5.7 and 11.5 oscillating cases. 62

Figure 3-15: RMS v velocity field for the A = 2°, k = 5.2, 5.7 and 11.5 oscillating cases. 63

Figure 3-16: RMS spanwise vorticity, ω_z, field for the A = 2°, k = 5.2, 5.7 and 11.5 oscillating cases. 64

Figure 3-17: Control volume used for determination of mean drag equation 65

Figure 3-18: Mean force coefficient, C_F, as a function of airfoil oscillation amplitude and reduced frequency. 68

Figure 3-19: MTV flow visualization (k = 8.8) and velocity vectors from the planar MTV data (k = 8.6) near the airfoil trailing edge. Airfoil at AOA=2°, trailing edge moving up (AOA decreasing). Dashed lines indicate initial line locations. 69

Figure 3-20: MTV flow visualization (k = 8.8) and velocity vectors from the planar MTV data (k = 8.6) near the airfoil trailing edge. Airfoil at AOA=0°, trailing edge moving up (AOA decreasing). Note flow visualization images flipped up/down. 70

Figure 3-21: Phase averaged vorticity, $<\omega_z>$, field for A=2°, k=4.1, 5.2, 5.7 and 11.5 cases. $\phi=0$. Dashed line indicates edge of data grid. Note: Vorticity contour levels different for each case as shown. 72

Figure 3-22: Vorticity profiles for 2 degree, k=5.2, 11.5 case at x = 6 cm, z = 0 cm. Curve is best fit to a Gaussian vortex profile. Horizontal profiles show quantity as a function of x, and vertical profiles a function of y. Equation represents the vorticity profile for a Gaussian vortex. 74

Figure 3-23: Azimuthal velocity profile for the 2 degree, k=11.0 case at x=6 cm, z=0 cm. Fits shown for portions of the profile indicated by the line sections. Functionality indicated by equation near the fit line. 75

Figure 3-24: Vortex array properties as a function of the streamwise distance. 78

Figure 3-25: Schematic representation of vortex spacing variables. Positive b indicates positive vorticity is above negative vorticity as shown. 80

Figure 3-26: Vertical vortex spacing, b, as a function of downstream distance. 82

Figure 3-27: Vortex streamwise spacing, a as a function of downstream distance. 83

Figure 3-28: Vortex convection speed, U_c, as a function of downstream distance. 84

Figure 3-29: Peak vorticity wpeak, circulation Γ, core radius r_c, convection speed U_c, and spacing (a,b) for the 2-D planar measurements at x= 6 cm, z = 10 cm. 85

Figure 3-30: Maximum swirl velocity, V_{sw}, as a function of the reduced frequency at x=c/2, midspan. 88

Figure 4-1: Schematic of the vortex / side wall interaction. 90

Figure 4-2: Sample line tagging imaged. A=2° k=11.5 x=$38r_{ci}$. Dashed white lines indicate undisplaced line center location for reference. 92

Figure 4-3: Schematic representation of axial flow profiles relative to vortex location. A=2°, k=11.5, x=$38r_{ci}$. 93

Figure 4-4: Local phase averaged peak spanwise flow, $<w>_{peak}$, versus the downstream distance, x, and the reduced frequency, k. Data plotted dimensionally. 94

Figure 4-5: Local peak spanwise flow, $<w>_{peak}$, versus the downstream distance, x, and the reduced frequency, k. Data plotted non-dimensionally. 95

Figure 4-6: Local peak spanwise flow, $<w>_{peak}$, versus the downstream distance, x, and the reduced frequency, k. Distance normalized by vortex array wavelength, a. 96

Figure 4-7: Peak axial flow speed, $<w>_{peak}$, versus the reduced frequency for A=2° at z=10cm off the centerspan. 97

Figure 4-8: Peak reverse axial flow speed, $<w>_{rev}$, versus the reduced frequency for A=2° at z=10cm off the centerspan. 97

Figure 4-9: Maximum axial flow, $<w>_{max}$, versus reduced frequency. 98

Figure 4-10: Spanwise flow versus vertical distance, y, and phase. A=2°, k=11.5. Downstream location indicated on figure. Line plots show all phases (i.e., y-profiles) simultaneously. 99

Figure 4-11: Axial velocity profiles for A=2°, k=9.6. Multiple phases shown simultaneously. 100

Figure 4-12: Axial velocity profiles for A=2°, k=5.2. Multiple phases shown simultaneously. 100

Figure 5-1: Schematic of flow field with cutting walls. Coordinate system origin is located at the cutting wall leading edge, as shown. 101

Figure 5-2: Impact speed, V_i, versus reduced frequency from the mid-span data. 102

Figure 5-3: Example phase-averaged spanwise velocity profiles for A = 2°, k = 11.5, x = $13r_{ci}$. Phase, ϕ, with the highest spanwise flow shown at each z location. Distance between profiles not shown to scale. 104

Figure 5-4: Peak spanwise flow speed for A = 2°, k=5.2. 105

Figure 5-5: Peak spanwise flow speed for A = 2°, k = 11.5. 105

Figure 5-6: $<w>_{peak}$ versus spanwise location for k = 11.5. 106

Figure 5-7: Peak to peak magnitude of velocity spike, V_{os}, as a function of reduced frequency. 106

Figure 5-8: Comparison of the front speed, V_f, the wave spanwise flow speed, V_w, and the equivalent sound speed, c_e. 108

Figure 5-9: Maximum spanwise velocity, $<w>_{max}$ comparing no-wall and cutting wall experiments. 109

Figure 5-10: $<w>_{rev}$ as a function of the reduced frequency. 110

Figure 5-11: Spanwise velocity profiles for A = 2°, k = 11.5, x = $58r_{ci}$ all phases (i.e. y-profiles) shown. 111

Figure 5-12: Comparison of the peak spanwise velocity between the line tagging and sMTV data. 113

Figure 5-13: Comparison of the planar (midplane) and stereoscopic (z=8cm, near midplane) measurements of the mean streamwise velocity, u, for k=11.5. 114

Figure 5-14: Mean streamwise velocity, u, fields, k = 5.2, z = r_{ci}, $2r_{ci}$, $10r_{ci}$, $20r_{ci}$. 115

Figure 5-15: Mean streamwise velocity profiles for x = $11r_{ci}$, k = 5.2 at different z's. .116

Figure 5-16: Mean streamwise velocity, u, fields, k = 11.5, z = r_{ci}, $2r_{ci}$, $10r_{ci}$, $20r_{ci}$. 117

Figure 5-17: Mean streamwise velocity profiles for three downstream positions at z = $2r_{ci}$, k = 11.5. 118

Figure 5-18: Mean lateral velocity, v, fields, k = 5.2, z = r_{ci}, $2r_{ci}$, $10r_{ci}$, $20r_{ci}$. 119

Figure 5-19: Mean streamwise velocity, v, fields, k = 11.5, z = r_{ci}, $2r_{ci}$, $10r_{ci}$, $20r_{ci}$. 120

Figure 5-20: Mean spanwise vorticity, ω_z, fields, k = 5.2, z = r_{ci}, $2r_{ci}$, $10r_{ci}$, $20r_{ci}$. 122

Figure 5-21: Mean spanwise vorticity, ω_z, fields, k = 11.5, z = r_{ci}, $2r_{ci}$, $10r_{ci}$, $20r_{ci}$. 123

Figure 5-22: Mean spanwise velocity, w, fields, k = 5.2, z = r_{ci}, $2r_{ci}$, $10r_{ci}$, $20r_{ci}$. 124

Figure 5-23: Mean spanwise velocity, w, fields, k = 11.5, z = r_{ci}, $2r_{ci}$, $10r_{ci}$, $20r_{ci}$. 125

Figure 5-24: Phase-averaged vorticity, $<\omega_z>$, for ϕ=0 at multiple span locations. k=5.2. .. 127

Figure 5-25: Phase-averaged vorticity, $<\omega_z>$, profiles for k = 5.2. Dashed lines $<\omega>$ = 0. Spacing of profiles in figure not to scale. 129

Figure 5-26: Phase-averaged spanwise velocity, $<w>$, for ϕ=0 at multiple span locations. k=5.2. 130

Figure 5-27: Phase-averaged spanwise flow, $<w>$, profiles for k = 5.2. Dashed lines $<w>$ = 0. Spacing of profiles in figure not to scale. 131

Figure 5-28: Comparison of vortex parameters (Γ, $<\omega_z>_{peak}$, r_c, U_c) from no-wall midspan data and cutting wall, z = $20r_{ci}$ (near midspan) data. k = 5.2. Symbols common. 133

Figure 5-29: Vortex parameters (Γ, $<\omega_z>_{peak}$, r_c, U_c, $<w>_{peak}$, b/a) for multiple span locations. k=5.2. Symbols common. 134

Figure 5-30: Relative location of the peak vorticity to the peak spanwise flow, k = 5.2. 136

Figure 5-31: Phase-averaged vorticity, $<\omega_z>$, for ϕ=0 at multiple span locations. k=11.5. 138

Figure 5-32: Phase-averaged vorticity, $<\omega_z>$, profiles for k = 11.5. Dashed lines $<\omega> = 0$. Spacing of profiles in figure not to scale. 139

Figure 5-33: Phase-averaged spanwise velocity, $<w>$, for ϕ=0 at multiple span locations. k=11.5. 140

Figure 5-34: Phase averaged spanwise flow, $<w>$, profiles for k = 11.5. Dashed lines $<w> = 0$. Spacing of profiles in figure not to scale. 141

Figure 5-35: Comparison of vortex parameters (Γ, $<\omega_z>_{peak}$, r_c, U_c) from no-wall midspan data and cutting wall, $z = 20r_{ci}$ (near midspan) data. k = 11.5. Symbols common. 143

Figure 5-36: Vortex parameters (Γ, $<\omega_z>_{peak}$, r_c, U_c, $<w>_{peak}$, b/a) for multiple span locations. k = 11.5. Symbols common. 144

Figure 5-37: Peak vorticity, $<\omega_z>_{peak}$, as a function of downstream distance for k = 11.5. Curves shown are vertically offset to allow simultaneous viewing. 145

Figure 5-38: Spatial correlation of initial local vorticity peak to r_c, U_c, $<\omega_z>_{peak}$, k=11.5. Vertical major grids are 0.1 apart. Magnitudes for the vertical axis can be found on Figure 5-36. 147

Figure 5-39: Relative location of the peak vorticity to the peak spanwise flow, k=11.5. 148

Figure A-1: Airfoil mean drag formulation control volume. 159

LIST OF SYMBOLS

Abreviations

AOA	Airfoil angle of attack
FOV	Field of view
IV	Camera intensifier voltage
MTV	Molecular Tagging Velocimetry
RMS	Root mean square
sMTV	Stereoscopic molecular tagging velocimetry

Symbols

A	Maximum airfoil angle of attack
b	Airfoil span length
c	Airfoil chord length
C_{FM}	Mean force coeffient from the mean velocity profile
C_{FP}	Mean force coeffient including pressure terms
d	Center to center time between gate pulse
F	Mapping function between real and image planes
$F_{i,j}$	Partial derivative of mapping functing; i with respect to j
f	Airfoil ossilation frequency
g_d	delayed gate period
g_u	undelayed gate period
h_o	Distance from the lense plane to center of the measurement plane
i	image plane direction
j	real plane direction

k	Reduced frequency: $k = (\pi cf)/U_{\infty}$
l_o	z-direction distance from lense plane to center of the measurement plane
Re_c	Chord reynolds number
r_c	Vortex core radius measured at x = 6cm from the midspan data
r_{ci}	Initial vortex core radius measured at x = 6cm from the midspan data
U_c	Vortex convection speed
U_{∞}	Tunnel free stream approach speed
U_0	Tunnel free stream at a given downstream measurement location
u	Streamwise velocity component
V_c	Equivilant sound speed
V_f	Front speed
V_i	Impact velocity, U_c/V_{sw}
V_{os}	Peak to peak spanwise flow speed difference for area varying wave.
V_r	Radial velocity component
V_{sw}	Peak swirl speed
V_{swi}	Initial peak swirl velocity measured at x = 6cm from the midspan data
V_w	Wave speed
V_{θ}	Azimuthal velocity component
v	Lateral velocity component
w	Spanwise velocity component
w_{max}	Highest axial flow speed measured in the spatial region investigated

w_{peak}	Local maximum in the axial flow speed
x	Streamwise direction
x_o	x-direction distance from lense plane to center of the measurement plane
y	Lateral direction
z	Spanwise direction
Δt	Time delay between undelayed and delayed images
ϕ	Data phase referenced relative to airfoil motion
Γ	Circulation
Γ_i	Initial circulation measured at x = 6cm from the midspan data
φ	Stereoscopic camera angle
τ	Tagged molecule phosporescence life time
ω_i	Initial maximum vorticity measured at x = 6cm from the midspan data
ω_{max}	Maximum spanwise vorticity
ω_{peak}	Local maximum spanwise vorticity
ω_z	Spanwise vorticity

CHAPTER 1

INTRODUCTION

Flows with strong concentrated regions of vorticity (here after referred to as a "vortex") are prevalent in many technological (e.g., wing tip vortices) and natural flow fields (e.g., tornadoes). The interaction of vortices with other vortices, boundaries (e.g., no-slip, free surface), particles, etc. is a fundamental problem in fluid mechanics. In this work the interaction of concentrated vortices with a no-slip boundary condition and the subsequent axial core flow was investigated using Molecular Tagging Velocimetry (MTV).

It has been shown in prior work (e.g., Laursen et al., 1997; Cohn and Koochesfahani, 1993; Koochesfahani, 1989) that the interaction of a vortex with a solid boundary perpendicular to the axis of the vortex core causes the flow along the axis of the vortex core (axial flow, core flow, or secondary flow). Figure 1-1 shows schematically the array of alternating sign vortices generated in the wake of an oscillating airfoil. When the vortices interact with a cutting wall, flow is developed in the vortex core. Figure 1-2 is taken from Koochesfahani (1989) and shows the top view of a dye visualization experiment in the wake of an oscillating airfoil. In Figure 1-2 the flow direction is right to left and the airfoil is directly upstream of the right side of the picture. The axial flow within a vortex core is made visible by lateral displacement of the dye. Figure 1-2(a) shows the development of axial flow as a result of the interaction of the vortex array with the side walls of the tunnel. In Figure 1-2(b) a false wall is placed into the center span location of the tunnel. Both (a) and (b) show dye being ejected away from the no-slip boundary as expected. A similar finding was reported by Wiegand (1993) for an axisymmetric vortex ring cut by a solid wall. In the present work the flow field of a line

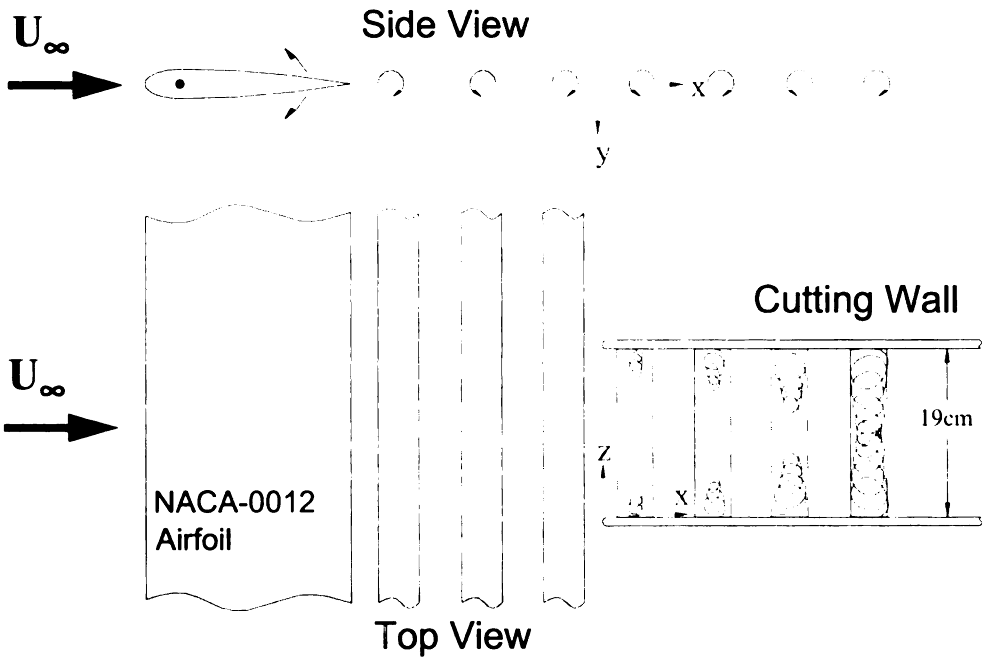

Figure 1-1: Schematic representation of flow field investigated.

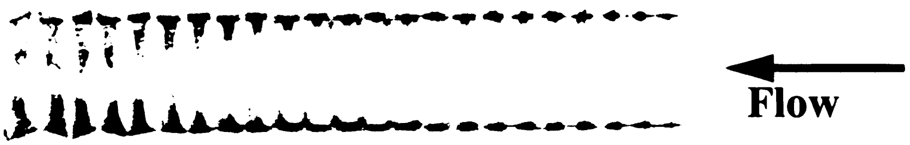

(a) without false walls

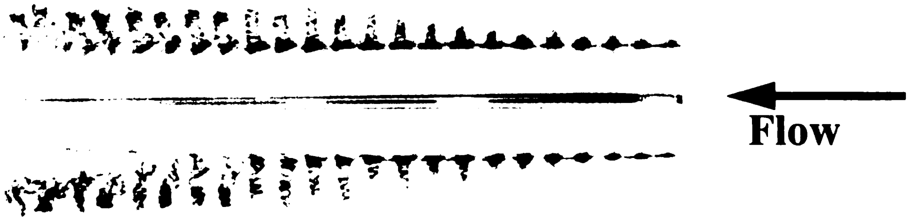

(b) with false walls

Figure 1-2: Top view dye visualization in the flow behind a pitching NACA0012 airfoil from Koochesfahani (1989). Flow is right to left, the airfoil is upstream of the right side of the image. Flow facility side walls, not shown, were above and below the dye traces.

vortex interacting with a no-slip boundary was investigated with the goal of understanding the effects of the interaction on the vortex.

Interest in flow fields with concentrated vortices containing axial flow is driven by several technical areas. For example, the passage of helicopter rotor blades creates trailing vortices behind the rotor blades. During forward flight, vertical descent and landing (forward based descent) following rotor blades can interact with the trailing vortex of the leading blade. This interaction, Vortex Blade Interaction (VBI), is a major source of noise and, as Conlisk (1997) noted, "reducing the number and intensity of the interactions is critical for reducing rotor noise." Much of the work with helicopter rotor fluid dynamics is conducted computationally. Reduction of the noise is dependant upon the ability to compute blade loads accurately. Conlisk (1997) indicates that many researchers/designers specify the vortex core structure and do not allow it to change temporally. This approach yields computed blade loads that are fairly accurate for a single interaction but the solutions were found to be sensitive to the core size chosen. When the vortex core structure was allowed to change with interaction and calculated along with the flow field for multiple VBI encounters the results no longer agreed well with experiments. Failure to predict the vortex structure changes is a limitation since multiple blades may interact with the same vortex. These observations were also echoed by Hassan et al. (1992) who noted that the accuracy of the simulations of VBI was dependant upon the user specified core size and strength.

A second area of technical interest in the subject of vortices with axial flow is in turbomachinery. Kotidis (1989) performed a study on the losses in a turbine. One of the identified losses was the transport of fluid from the tip of the blade to the hub via axial flow within the spanwise shed vortices. As a final technical example, vortex breakdown, important in many technical areas, has been associated with sudden widening of the vortex radius and a deceleration of the axial flow within the core (e.g., Lopez 1990). Naturally occurring flow fields that exhibit strong regions of vorticity also show flow along the axis of the vortex. A vivid example of axial flow within a strong vortex occurs within tornadoes and hurricanes, and to a lesser extent in dust devils and water spouts (Maxworthy, 1973).

Much of the past work in the area of rotational flow near a no-slip boundary, including the start-up axial flow within a vortex core, and the resulting 3-D core structure is analytical. First solutions in this area considered either a quiescent fluid above a rotating infinite plate (von Kármán, 1921), or solid body rotation over a infinite plate (Bödewadt, 1941). These flows are illustrative in that the source of axial flow, or secondary flow, within the core of a vortex can be understood by examining these "simple" flows. Consider the case of solid body rotation over a fixed plate shown in Figure 1-3. The flow has a constant angular velocity equal to ω. Away from the wall where, the flow can be assumed inviscid, the r-momentum equation can be simplified to the Euler-n equation which equates the radial pressure gradient to the azimuthal velocity and radial location. Near the plate viscosity cannot be neglected. The azimuthal velocity is reduced but the radial pressure gradient is assumed to be the same as the far field via boundary layer approximations. The corresponding imbalance indicates fluid particles move radially inward (for rotating fluid, fixed wall) near the wall. Note that the Euler-n equation does hold near the wall in the boundary layer, but the r-momentum equation can be used to re-derive the expression with additional terms (from the viscous term in the r-momentum

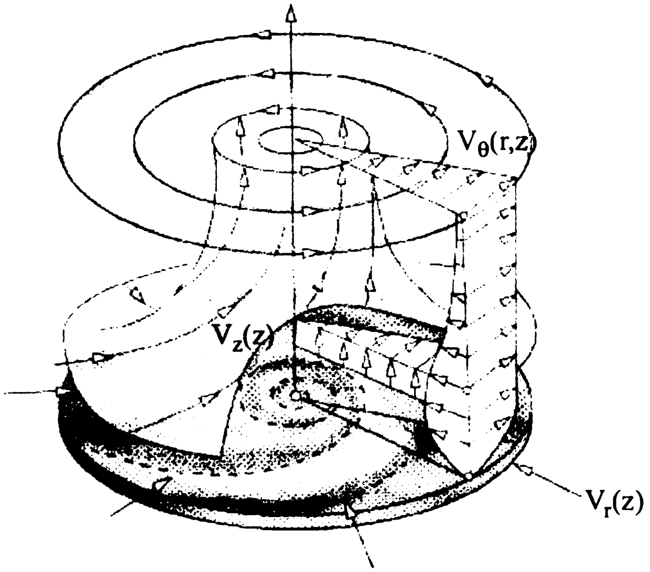

Figure 1-3: Schematic of rotational flow over a fixed solid boundary. Adapted from Figure 10-1 from Schlicting (1960). Figure courtesy of Kind Design, Inc.

equation) with $V_r(r,z)$ added. The fluid particles transported towards the center of the vortex are expelled away from the wall due to mass conservation. For example, in Figure 1-2(a) the axial flow that develops due to the interaction of the vortex with the side walls of the tunnel is directed away from the walls. Similarly, when the cutting plate is placed into the flow near the centerline of the tunnel, as in Figure 1-2(b), the axial flow is directed away from the flat plate.

While the solid body rotation flow field is illustrative, it does not represent the vortical flow field of a concentrated line vortex. Other researchers (e.g. Rott and Lewellen, 1966; Burggraf et al., 1971) have sought similarity solutions for a generalized vortex, defined by the azimuthal velocity field, $V_\theta \sim r^{-\alpha}$, over a no-slip wall. The flow field of a generalized vortex is defined at the extremes by $\alpha = -1$ for a solid body rotation and $\alpha = +1$ for a potential vortex. Rott and Lewellen (1966) were limited to $\alpha < 0.1217$

because the solution diverged for $\alpha > 0.1217$; however, Burggraf et al. (1971) were able to find solutions for the entire range of α by creating composite similarity solutions. Kuo (1970) developed analytical solutions for vortices that simulated tornadoes, or flows in tornado chambers. The solution showed a strong upward motion of fluid within the core of the vortex and a weaker descending or recirculating motion outside the core region.

Donaldson (1956) and Donaldson and Sullivan (1960) investigated axial flow solutions allowable under the Navier Stokes equations. Donaldson and Sullivan (1960) were able to show that several different axial flow core structures were possible. These core structures included single axial flow peak in the center of the vortex (single-celled structures) and axial flow distributions with both positive and negative axial flow velocities (multi-cell).

Experimental work on the formation of axial flow, and the resulting core structure, is limited. Koochesfahani (1989) studied the flow behind an oscillating NACA0012 airfoil and showed that axial flow developed within the vortex core due to interaction with solid boundaries (i.e., the tunnel side walls and/or false walls placed in the flow). The magnitude of the axial flow speed was estimated by the displacement of dye and appeared to vary linearly (for constant oscillation amplitude) with the reduced frequency. The magnitude was significant with respect to the freestream velocity (around $W/U_\infty = 0.3$-0.65). Koochesfahani (1989) noted that the use of dye to estimate the axial flow speed represents an integrated or average velocity during the dye transport. Cohn and Koochesfahani (1993) looked at the boundary conditions that cause axial flow to be initiated in a flow field similar to Koochesfahani (1989). The axial flow was initiated for the no-slip boundary as expected. However, axial flow was also initiated for a shear boundary condition. The core structure was visually different between the two experiments. The solid wall boundary created a core structure with the highest axial flow near the center of the vortex core (single-cell). In contrast, the shear boundary created a core axial velocity profile that indicated the maximum axial velocity occurred near the edge with a very small axial velocity near the center (multi-cell).

Laursen et al. (1997) performed Particle Image Velocimetry (PIV) measurements and dye visualization for a 2-D vortex pair, created by ejecting fluid through a slit, traveling in a still fluid. They noted that the vortex structure is initially 2-D, but quickly becomes unstable and breaks up. Evidence for the "break up" indicated axial flow within the vortex core was responsible. An estimate for the axial flow speed was determined using dye markers. The data indicated that the axial flow speed was nearly equal to the convection speed of the vortex pair. Hagen and Kurosaka (1993) used heated fluid as a passive tracer in a hairpin vortex created by a ramp protruding into a flow. The results confirmed the corewise transport of the heated fluid within the vortex core. The velocity of the transport was found to be on the same order as the free stream velocity.

The previous experimental studies were performed for free or convecting vortices. More work had been performed for confined vortices (e.g., vortex tubes, "tornado chambers", etc.). Measurements of the velocity field of a vortex in a tornado chamber were made by Wan and Chang (1971). These experiments indicated that the axial flow structure for tornado-like vortices was determined by a parameter $e_c = Q_c/(\Gamma r_c)$, where Q_c is the volume flow through the vortex core, Γ is the circulation and r_c is the core radius of the vortex. Two cases were studied, a "low" e_c, and a "high" e_c. The low e_c

vortex had a single cell axial flow structure, while the high e_c had a two cell axial flow structure.

Hirsa et al. (2000) studied the flow field of a vortex created by a pair of flaps in a tank using PIV and flow visualization. The data indicated that there was a region of recirculation near the wall within the vortex core with very little axial flow. This region was characterized by a sudden increase in the radius of the vortex and was considered to be analogous to vortex breakdown seen in vortex chambers. The structure of their vortex indicated that maximum axial flow was at approximately $r = r_c$, rather than $r = 0$. The recirculation region was also discussed in Maxworthy (1972) and was described as a "vortex jump". Maxworthy indicated that this jump region allows the flow to match boundary conditions between the natural upflow from the vortex no-slip interaction, and the much larger outflow from the chamber. The vortex jump discussed in Hirsa et al. (2000) and Maxworthy (1972), has also been observed in natural flow fields such as dust devils, waterspouts, and tornadoes, Maxworthy (1973).

Vortex interaction with walls has been studied for vortices with axial flow already present by Krishnamoorthy and Marshal (1994), Marshall and Yalamanchili (1994) and Marshall and Krishnamoorthy (1997). In these works the results show that a vortex with axial flow present that is cut will produce either expansion or compression waves at the wall, depending on the direction of the axial flow with respect to the cutting wall. The area varying waves travel along the core of the vortex away from the cutting surface. Lundgren and Ashurst (1989) investigated the propagation of area varying waves on the vortex core and found that the equations governing the propagation of wave on a vortex core were analogous to gas dynamics wave transport equations.

To date, quantitative measurements of any kind are limited and whole field measurements of the vortex core with axial flow do not exist. Rockwell (1998) reviews the literature on vortex body interaction. In the section on normal interactions (i.e., were the axis of the vortex is perpendicular to the cutting body) Rockwell (1998) states that the "study of vortex distortion in the vicinity of the surface, fully accounting for viscous effects, would be fruitful." Therefore, well resolved measurements in the core of a vortex interacting with a no-slip boundary are needed to provide fundamental understanding for further work in this area. The current research is aimed at acquiring an understanding of the development of axial flow due to normal incident interaction of a columnar vortex with a no-slip boundary and the associated effects on the vortex structure.

In this work, measurement and analysis of the undisturbed flow field (flow in the near wake of a pitching airfoil Figure 1-4) was required to provide reference and initial conditions. However, the problem of the trailing edge flow field and initial development of the vortical wake behind an oscillating airfoil is also of fundamental interest to aerodynamicists. Three specific areas of interest are: the validity of the unsteady Kutta condition at the trailing edge, the formation region of the vortex array, and the mean thrust/drag of an oscillating airfoil.

Much of airfoil theory and design is based upon inviscid theory, use of which is reliant upon assumptions of the flow conditions at the trailing edge of the airfoil. Inviscid approximations require that the flow leave the airfoil trailing edge "smoothly". The Kutta condition requires that a stagnation point exists and is fixed at the trailing edge for the static airfoil (McCrosky, 1982). The unsteady Kutta condition is an extension of the steady

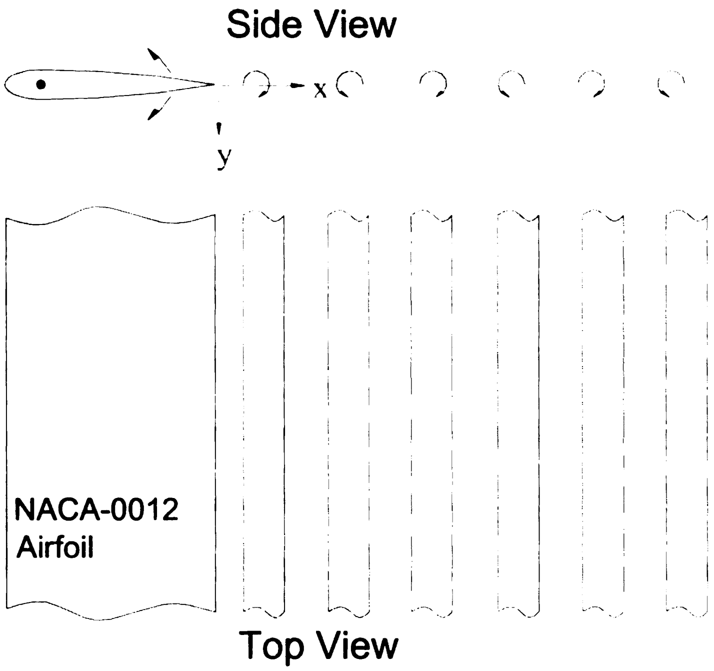

Figure 1-4: Schematic of initial vortex array formation flow field.

Kutta condition to allow inviscid analysis on a oscillating airfoil and assumes a zero pressure difference across the trailing edge (Maskell, 1972; Giesing, 1969).

Experimental work, used to determine how well the inviscid analysis represents real viscous flows, has shown that the classic unsteady Kutta condition may be valid at low reduced frequencies; however at higher reduced frequencies the validity is less certain (Poling and Telionis, 1986). Uncertainty over the importance of trailing edge conditions can be illustrated by the conclusions of two works. Katz and Weihs (1981) concluded that the use of the unsteady Kutta condition, though it may be physically inaccurate, does provide accurate estimates of airfoil forces and downstream flow patterns using inviscid solution methods. Stanek and Visbal (1989) performed a simulation using the full Navier Stokes equations of the flow field experimentally investigated in Koochesfahani (1989).

The results showed only qualitative agreement between the calculations and experimental data. The differences were attributed, in part, to resolution near the trailing edge and details of the trailing edge shape. These differences highlight importance of the trailing edge flow conditions.

The study of the mean flow field downstream of oscillating airfoils has been motivated by the use of oscillating and/or heaving airfoils as a thrust generation mechanism (Anderson, 1998; Streitlien and Triantafyllou, 1998; Platzer and Neace, 1993). The formation of the vortex array behind an oscillating airfoil has been studied mainly with flow visualization and point measurements (Wilder et al., 1996; Koochesfahani, 1989). Koochesfahani (1989) showed, using dye visualization, that the vortical pattern in the flow field generated by the oscillating airfoil can be complicated with multiple structures for each oscillation depending up on the oscillation amplitude, frequency and wave form. The mean thrust has been calculated using point data based on the mean streamwise velocity field (e.g. Anderson et al., 1998; Koochesfahani, 1989). Whole field, time resolved velocity and vorticity measurements of the formation region behind an airfoil are limited. Whole field measurements would increase the general understanding of the physics of the flow field and allow the thrust/drag to be estimated more precisely.

The current work can, therefore, be divided into two broad categories: the initial formation region of the 2-D vortex array without cutting walls and the interaction of the vortex array with the no-slip cutting walls. The flow field for the first section of this work, shown schematically in Figure 1.4, is characterized by the airfoil parameters, the chord, c, and reduced frequency, k. The coordinate system origin for this subsection of the study was at the trailing edge of the airfoil when the airfoil passed through 0 degrees, as shown.

The measurements of the undisturbed flow field were needed to determine the initial conditions for the axial flow study. The same measurements of the undisturbed flow field simultaneously provided the secondary goals for this work. Specifically, details of the near field development of the flow behind an airfoil oscillating at a high reduced frequency touching on the associated issues and characterization of the development of the wake of an oscillating airfoil over the first chord length downstream from the airfoil trailing edge.

It is important to note that the work detailing the vortex / wall interaction has considered the dynamics of a vortex interacting with a no-slip boundary without regard to the generation method. The airfoil is used as a method of generating vortices because it allows control of the vortex properties through the airfoil peak amplitude and oscillation frequency.

The primary goal of this work was to investigate the interaction of the vortex array with a no-slip boundary (Figure 1-1). The flow field for this portion was characterized by the vortex strength (i.e., circulation, Γ, and peak vorticity, ω_z) and core radius, r_c (defined as the 1/e point for a Gaussian vortex). This flow field was shown schematically in Figure 1.1. The origin was fixed at the leading edge of the wall with z positive away from the wall. The goal of this portion of the work was to detail the vortex and axial flow structure after the vortex/cutting wall interaction and the changes in the vortex properties after the interaction. The axial flow properties were measured and the effect of the axial flow on the vortex peak vorticity, circulation and core size was detailed. Finally, the presence of area varying waves on the vortices was addressed.

The remainder of this work is divided into three broad categories: experimental methods (Chapter 2), results/discussion (Chapters 3-5) and conclusions (Chapter 6). The results and discussion are further subdivide into the initial evolution of the vortex array without the cutting walls (Chapter 3), the spanwise flow generated by the vortex / tunnel side wall interaction (Chapter 4), and the vortex array properties after interaction with the cutting walls (Chapter 5).

CHAPTER 2

EXPERIMENTAL METHODS

2.1 Facility

The interaction of a vortex core cut by a solid wall is investigated in this work. The resulting flow field is shown schematically in Figure 1-1. A NACA-0012 airfoil (chord, c=12cm) was oscillated in a periodic motion about the quarter chord location to generate a sequence of alternating sign vortices. The motion was described by a sine function with a peak amplitude or airfoil Angle of Attack (AOA), A, and a frequency, f, (Figure 2-1).

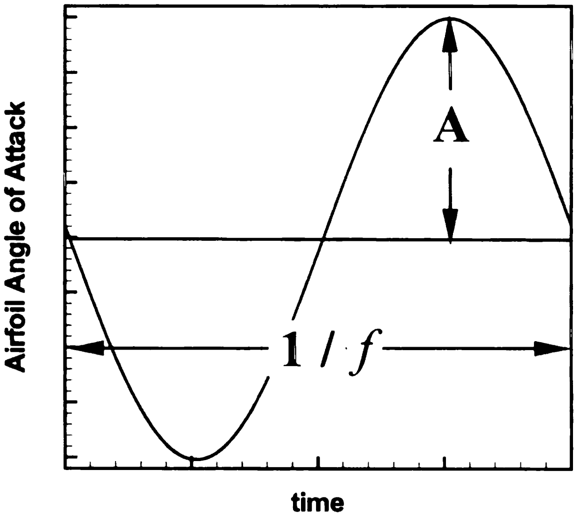

Figure 2-1: Definition of the airfoil motion.

Walls were placed into the flow field after isolated vortices were formed to cut the vortices. The work of Cohn and Koochesfahani (1993) and Koochesfahani (1992, 1989) indicate that shortly after the vortex/cutting wall interaction occurs a transport of fluid within the core region of the vortex is initiated.

The research was conducted in an Engineering Laboratory Design (ELD) 10,000 liter close-loop water tunnel with a 2'x2'x8' (61 cm x 61 cm x 243 cm) test section, see Figure 2-2. The facility is located in the Turbulent Mixing and Unsteady Aerodynamics Laboratory at Michigan State University.

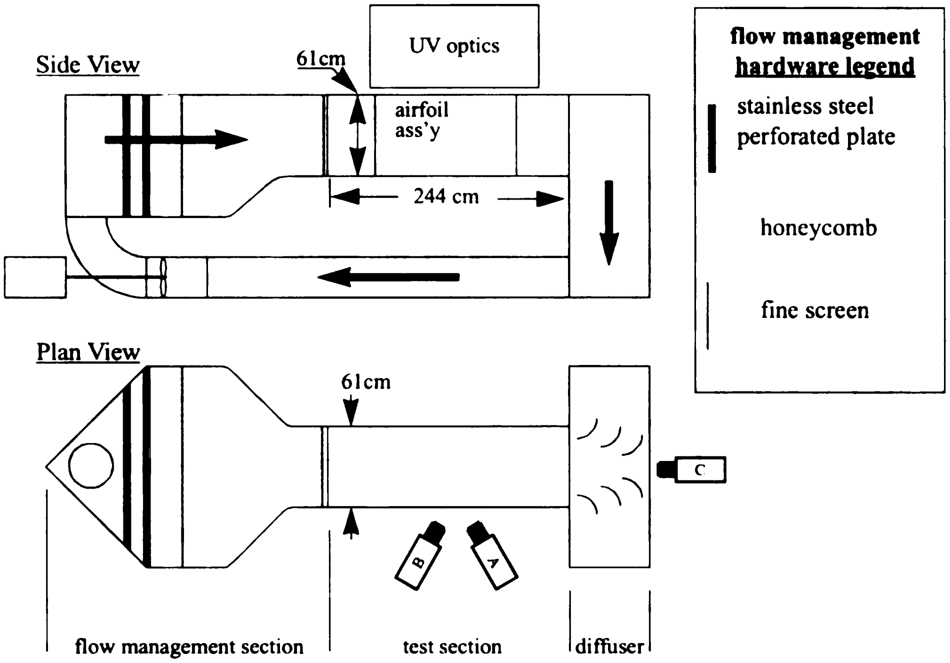

Figure 2-2: Schematic of the Turbulent Mixing and Unsteady Aerodynamics Laboratory 10,000L water tunnel at Michigan State University. Cameras A and B shown positioned for stereoscopic measurements. Camera C shown positioned for single line tagging experiments.

The freestream velocity, U_∞, was adjusted to 10.5 cm/s, which corresponds to a chord Reynolds number, $Re_c \approx 12000$. The Re_c was chosen to match the conditions reported in Koochesfahani (1992, 1989). The flow upstream of the airfoil had a RMS level of $0.015U_\infty$. The unsteady pitching of an airfoil can be characterized by the reduced frequency, k, where $k = (\pi c f)/U_\infty$. Given $c = 12$ cm and free stream velocity, $U_\infty = 10.5$

cm/s, the reduced frequency was $k = 3.59f$, where f is the frequency of the airfoil motion. The airfoil was held in a false wall assembly that allowed linkage between the motion controller and airfoil. The airfoil was held with only a small gap (< 1mm) between the airfoil and assembly walls. The aspect ratio of the airfoil/assembly was 4:1.

The motion of the airfoil was controlled by a Galil DMC-1030 motion control unit. The resolution of the motor providing the motion was 10,000 counts per revolution or 27.7 counts per degree. The controller was programmed to provide a symmetric sinusoidal motion to the airfoil. An example of the airfoil motion is shown in Figure 2-3. The deviation level was found by subtracting the actual airfoil position from the best fit sine wave for the data. The peak deviation was 2 counts (0.07 degrees). The RMS deviations level was 0.6 counts (0.02 degrees). The deviation levels, peak and RMS, were representative of all airfoil motions.

The airfoil zero angle of attack was found by oscillating the airfoil at several reduced frequencies and measuring the vortex array properties, $<\omega_{peak}>$, Γ, and r_c. The ratio of these properties between the positive and negative vortices was calculated and plotted versus mean angle. The airfoil zero AOA was determined by the condition that most caused the ratios to be one. Once the airfoil zero AOA was determined, a camera was aligned with a physical target placed on the airfoil and fixed securely in place. The airfoil zero AOA could then be checked as needed based on camera images of the target. This ensured a consistent zero degree AOA throughout the experimental procedure.

Two oscillation amplitudes, A = 2° and 4°, with frequencies in the range of f = 1.14-3.20 Hz (k = 4.3 - 12.1) for A = 2° and f = 1.14-1.78 Hz (k = 4.3 - 6.7) for A = 4° were investigated for this work. The low end of the reduced frequency range was high

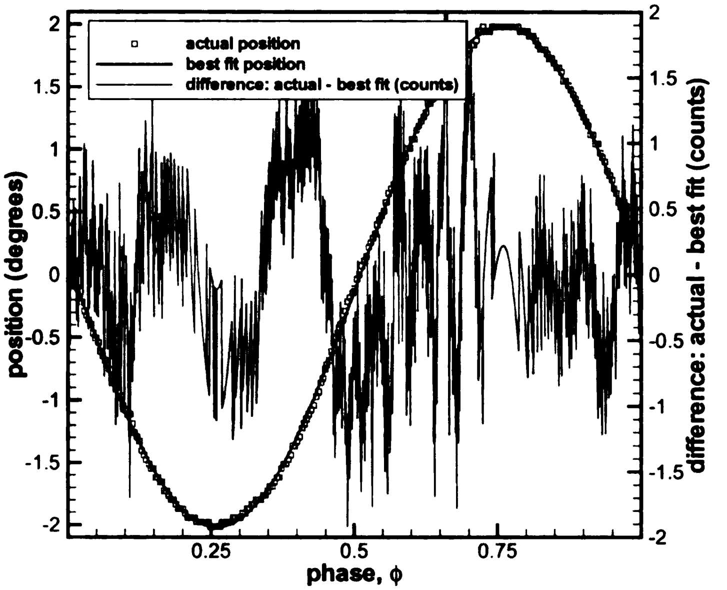

Figure 2-3: Representative example of real airfoil motion (A = 2°, k=8.6) with a comparison to programmed functionality. Difference between the real and programmed in counts.

enough to ensure that isolated vortices were formed by the first chord length downstream of the airfoil trailing edge. The upper end of the reduced frequencies was limited by the spatial stability of the vortex array. Specifically, at higher reduced frequencies the vortex array was found to change lateral position during and between runs.

2.2 Two Component Planar Molecular Tagging Velocimetry

2.2.1 Technique Description

Molecular Tagging Velocimetry (MTV) is a whole field optical technique which relies on molecules that can be turned into long lifetime tracers upon excitation by photons of an appropriate wavelength. Typically a pulsed laser is used to "tag" the regions of interest and those tagged regions are interrogated (i.e. imaged) at two successive times within the lifetime of the tracer. The displacement of the tagged region between the two interrogation times is determined and the measured Lagrangian displacement vector provides the estimate of the velocity vector, see Figure 2-4. MTV can be viewed as a

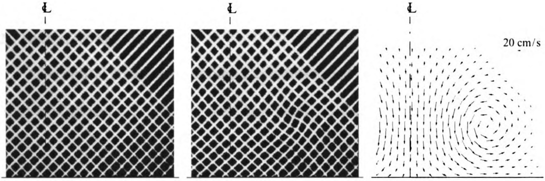

(a) **(b)** **(c)**

Figure 2-4: Typical MTV image pairs and the resultant 2-component velocity vector field. The flow shown is from a vortex ring impacting a flat wall at normal incidence. The axis of symmetry is indicated by the dashed lines.(a) Undelayed grid imaged 1μs after the laser pulse ("undelayed" image) (b) same grid imaged 8ms later ("delayed" image) (c) velocity field derived from (a) and (b). Gendrich and Koochesfahani (1996).

molecular analogue to Particle Image Velocimetry (PIV) and can be utilized in flows where particle seeding, needed for PIV, is either difficult or problematic. MTV was better suited to the current study because particle seeding within the core of a vortex is difficult.

The 2-component and 3-component measurements in this study utilized a grid of intersecting laser lines, as shown in Figure 2-4, for tagging purposes. A direct spatial correlation method was utilized to determine the displacement of the tagged regions. Detailed discussions of the planar 2-component MTV technique, and the chemistry of the chemical complex used, can be found in Koochesfahani et al. (1996), Gendrich and Koochesfahani (1996), Gendrich et al. (1997), and Koochesfahani (1999).

The molecular tracer used in this study was a chemical triplex with the following molar concentrations: 1×10^{-4} M $g_1\beta$-cyclodextrin, 0.055 M cyclohexanol, and a saturated solution of 1-bromonaphthalene (approx. 1×10^{-5} M). The lifetime for this chemical complex was nominally τ =3.5ms. The photon source was a Lambda Physik LPX 210i XeCl excimer laser which generates 20 ns long pulses at a wavelength of 308 nm.

2.2.2 Optical Arrangement

The optical arrangement for the 2-component and 3-component MTV experiments is shown in Figure 2-5. The excimer laser produced a rectangular beam that was first passed through a cylindrical lens combination to expand the beam along the long axis. A second cylindrical lens combination was used to focus the beam along the short axis into a thin sheet approximately 0.5 mm thick. The use of cylindrical lens combinations for these two operations allowed variable focal lengths to be achieved which in turn allowed the

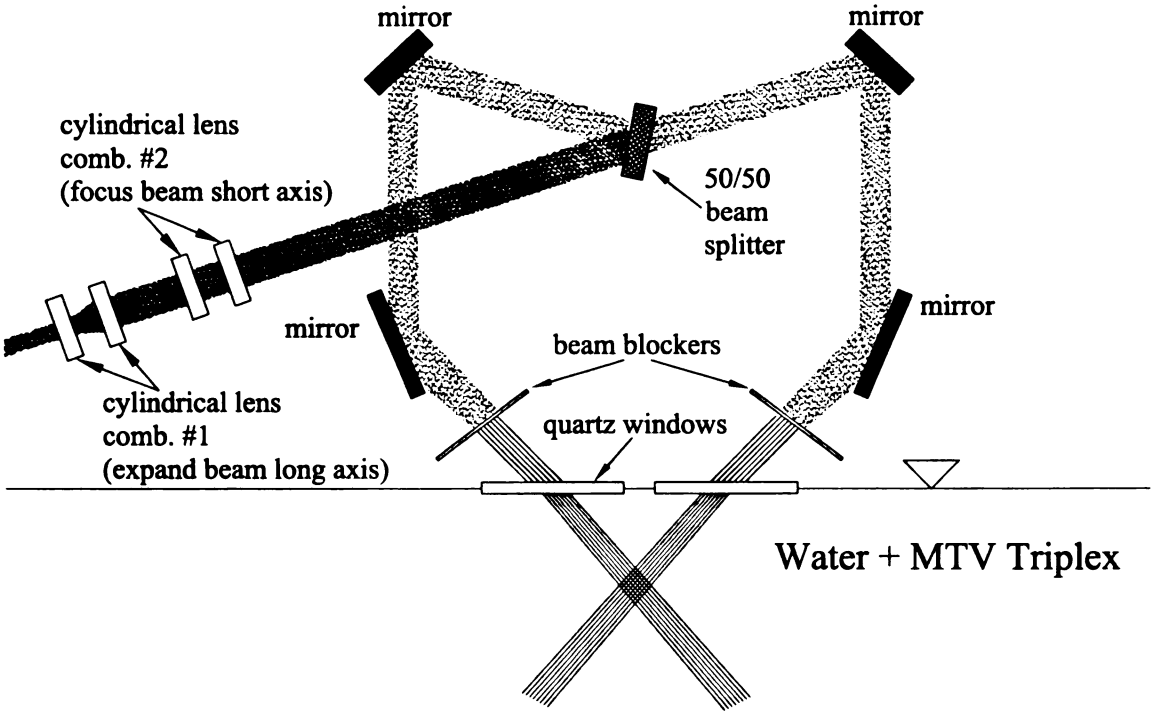

Figure 2-5: Schematic representation of optical set-up for planar and stereoscopic MTV experiments.

beam to be focused where needed (i.e., at the measurement plane). The beam next passed through a 50-50 beam splitter to create two laser sheets. The sheets were redirected into the tunnel using an array of mirrors. Brass plates with machined slots were used to alternately block and pass portions of the beam, creating a series of lines. Quartz windows were set on the top free surface of the water tunnel to allowed the beams to enter the working fluid without distortion from surface waves. The series of lines from the two sheets intersected in the measurement region, creating a tagged grid pattern similar to that shown in Figure 2-4.

2.2.3 Imaging Details

Past implementations of MTV (see e.g. Gendrich 1998, Cohn 1999) have used a two camera approach to image the illuminated flow patterns. One camera begins to acquire an image a short time (~ 1 μs) after the laser fires to provide the initial pattern location or the "undelayed" image. An image from the second camera is taken a known time after the first camera to provide the distorted, or "delayed", image. Use of this technique requires the two cameras to be spatially aligned precisely. A different strategy is used in this study to provide the image pairs. Specifically, a strategy was employed which that allowed the two cameras, described above, to be replaced with a single intensified Charge Coupled Device (CCD) camera.

Intensified cameras, analogous to "night vision" cameras, allow amplification of low light scenes. The image intensity is controlled by setting the gain (i.e. amount of amplification) and the gate period. The camera electronics allow the user to arbitrarily place the gate pulse (i.e. "intensifier on" pulse) within a frame. When the pulse is high the intensifier is activated and the camera CCD array is exposed to photons. The period of the

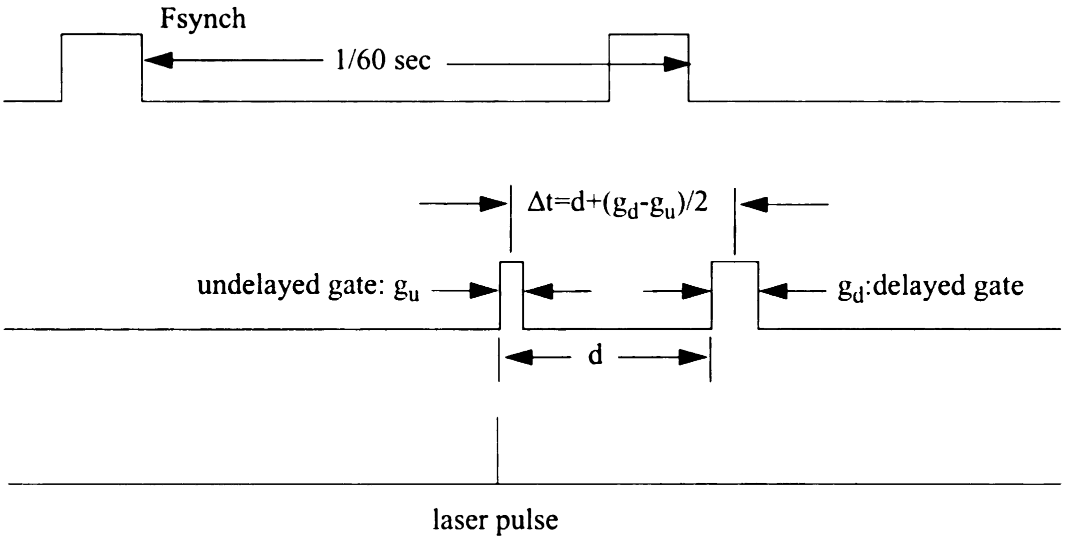

Figure 2-6: Timing diagram for the "double shot" camera operation. Each Fsynch pulse indicates the start of a new image.

gate pulse is analogous to the shutter time on non-intensified video or still cameras. By utilizing the ability to place the shutter at any point within the frame time, an image pair can be created by gating one frame at the end of a frame (the undelayed image) and gating the next image at the beginning of the following frame (the delayed image) for the "double shot". A Stanford Computer Optics (SCO) 4QuikE intensified camera was used in this work. This camera is a full frame CCD camera with a resolution of 640 x 480 pixels and a framing rate of 60Hz. This timing strategy reduced the effective data rate by one half, from 60 Hz to 30Hz, as two frames were needed to provide each image pair (i.e. each instantaneous whole field velocity measurement).

A schematic of the "double shot" camera timing diagram is shown in Figure 2-6. The timing signals were created using a function generator and two Stanford Research Systems (SRS) Digital Delay Generators. The laser was fired shortly (~1μsec) before the undelayed gate was applied. The center to center time between the gate pulses, d, was precisely known.

The delay times used in this study were near to the lifetime value for the chemical triplex (3.5-4.5 msec) and therefore the light intensity of the tagged regions was expected to drop approximately 66% from the undelayed to the delayed images. The intensified cameras used did not allow change in the camera intensifier gain between images. The tagged lines in the delayed image would therefore become too dark compared to the undelayed tagged lines to be used in the correlation routine. Different gate periods were used for the undelayed and delayed images to compensate for the loss of intensity. The delay time between images was therefore defined for this timing strategy by the time from the center of the undelayed gate to the center of the delayed gate plus as shown in Figure 2.6. Typical gate periods were 0.2 msec and 0.4 msec for the undelayed and delayed images respectively.

The use of intensified cameras can be complicated by a mean background pattern on the image. Figure 2.7 shows a mean background image from a SCO camera. Observation of this image indicates a small scale honeycomb pattern on the image caused by the intensifier coupling. MTV data are affected by this background pattern in the following way: There are two intensity patterns present on each data image, the tagged lines and the background honeycomb pattern. The tagged line patterns move spatially, however the honeycomb pattern remains fixed relative to the CCD array. There is a relative displacement between the tagged lines and the honeycomb pattern. This relative displacement is measurable, and causes an extra error in the measurements. The error was significantly reduced by correcting for the honeycomb pattern. A series of images were

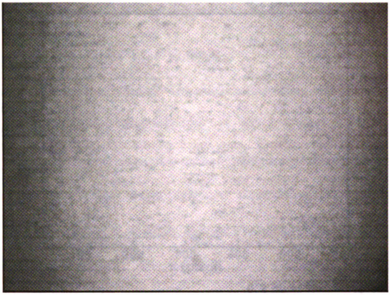

Figure 2-7: Mean image pattern from a SCO intensified camera.

taken of a relatively uniform image (uniformly illuminated white background), and those images were averaged to create an average image that contains the background honeycomb pattern as shown in Figure 2.7. All data images were then divided by that mean background image reducing the effect of the mean background image. There was also a large scale non-uniformity in the image intensity (i.e. the image is darker on the edges) shown in Figure 2-7. This intensity pattern does not affect MTV measurements because of the global, rather than local nature of the pattern, however, this non-uniformity was also compensated for in the above strategy.

The affect of the background and the background compensation technique were illustrated via target tests. A target was displaced uniformly in the x-direction in these tests. The measured displacement was found and the difference between the measured displacement and the actual uniform displacement was taken to be the error. This was

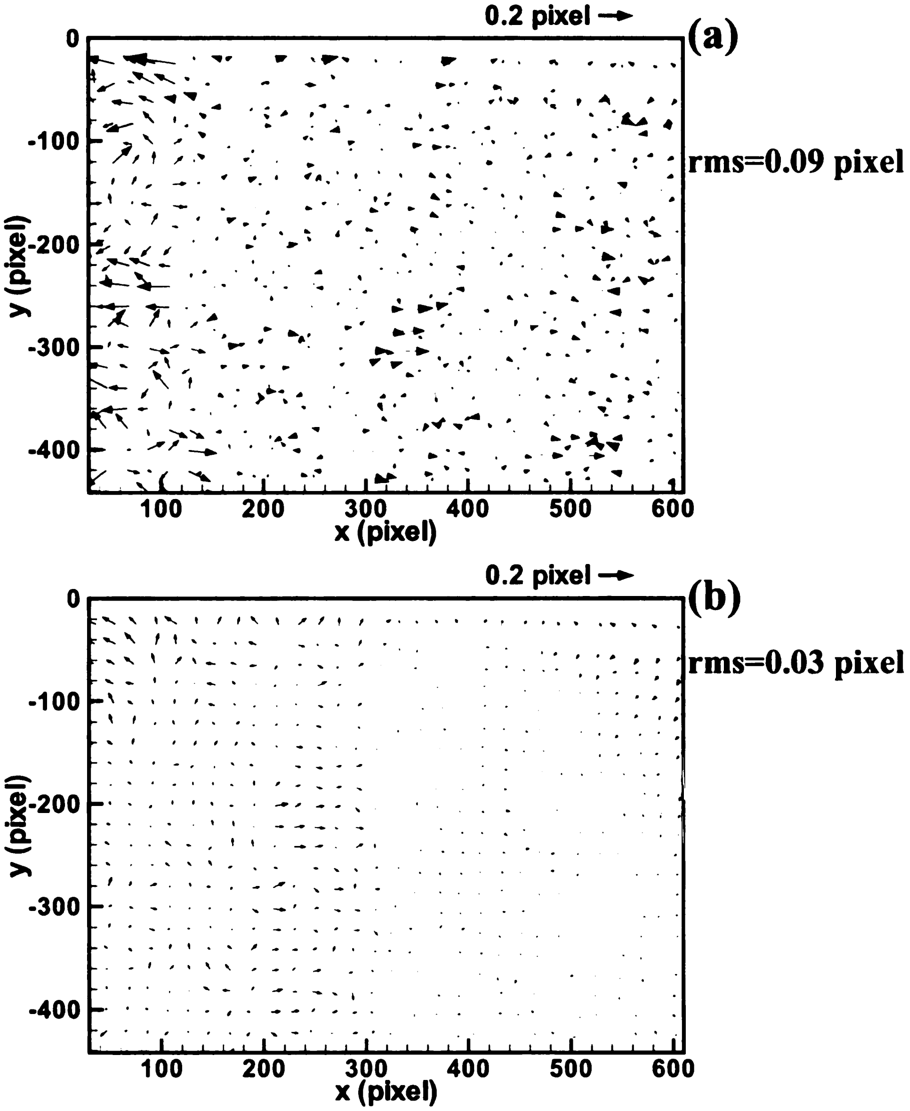

Figure 2-8: Deviation from a uniform displacement, without (a) and with (b) background correction.

performed on the same images with and without background compensation. Figure 2.8 shows the error for the target tests. The figure clearly shows the decreased error in the compensated data over the majority of the image plane. Quantitatively, the error level, measured by the RMS level, was reduced by a factor of three through the compensation technique used. Typical error levels are discussed in the next section.

2.2.4 Instantaneous Planar MTV Error Estimation

A series of images of a target with zero displacement were taken with the SCO cameras used in this study and processed using the MTV correlation technique to provide an estimate in the uncertainty in the planar implementation of the technique. The u and v displacements for these images, when processed, should be zero because the target was fixed spatially. Any non-zero displacements were a result of noise on the image and error from the processing technique. This error estimate is not affected by the background pattern discussed in the previous section because there was no displacement for these error tests. The results from these tests is shown in Figure 2.9 for the intensified cameras used in this study. An extensive discussion of general error estimation for the planar technique in general can be found in Gendrich and Koochesfahani (1996). The camera intensifier was a significant source of image noise so the error level in Figure 2-9 was found as a function of camera gain. Typical intensifier voltage (IV) levels are between 1200 and 1240 in this study which corresponds to an error level of 0.17 to 0.24 pixels. The error level quoted was for the 95% confidence level, indicating that 95% of the measurements will be better than the quoted error estimate. This corresponds to a 0.08 to 0.12 pixel RMS error level for a Gaussian distribution. Typical magnifications and delay times of 0.0088 cm/pixel and 3.5msec, respectively, were used in this study. The 95% error level for an instantaneous measurement in dimensional units was therefore 0.4 to 0.6 cm/sec.

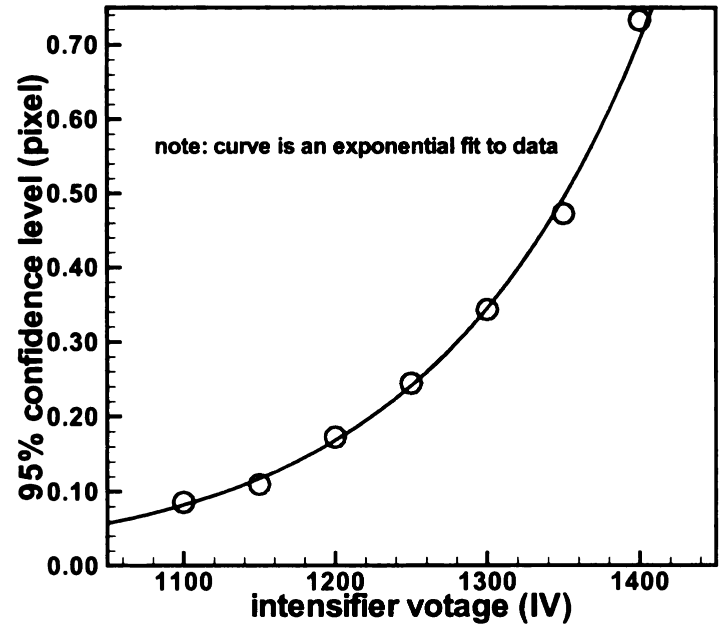

Figure 2-9: Uncertainty level in MTV planar technique for SCO intensified cameras as a function of camera gain.

2.3 Stereoscopic MTV

2.3.1 Angular Stereoscopic Method Description

Standard planar optical techniques such as MTV and PIV measure velocity components in the plane of the laser sheet (i.e. they provide two components of the velocity vector in the plane of the laser sheet). In a flow with all three velocity components standard planar techniques have two weaknesses: First, the accuracy of the two dimensional velocity vectors suffers due to artificial in-plane velocities measured as a result of the out-of-plane motion. This effect can be minimized by the appropriate choice of optics. Second, a potentially significant portion of the flow dynamics (i.e. the out-of-plane velocity component) is not measured.

Measurement of all three velocity components was needed for this study and therefore a stereoscopic Molecular Tagging Velocimetry (sMTV) technique was developed. Stereoscopic measurement techniques make use of two detectors that view the measurement region from two different perspectives. Comparison of the simultaneous flow velocities between the two cameras yields the complete velocity vector in the plane of the laser sheet.

An angular stereoscopic measurement technique was developed and tested for use with the base planar MTV technique for this work. A schematic of a general angular stereoscopic system is shown in Figure 2-10. The construction of the 3 component velocity field from the individual cameras 2-component measurements can be accomplished using two primary techniques: geometric reconstruction, and the "generalized undistortion" method. The geometric reconstruction method uses ray tracing and pin hole approximations, see for example Westerweel and Newstadt (1991) and Bohl et al. (2001). The reconstruction equations are dependant upon the physical parameters of the experimental system as shown in Figure 2-10. In addition, the geometric

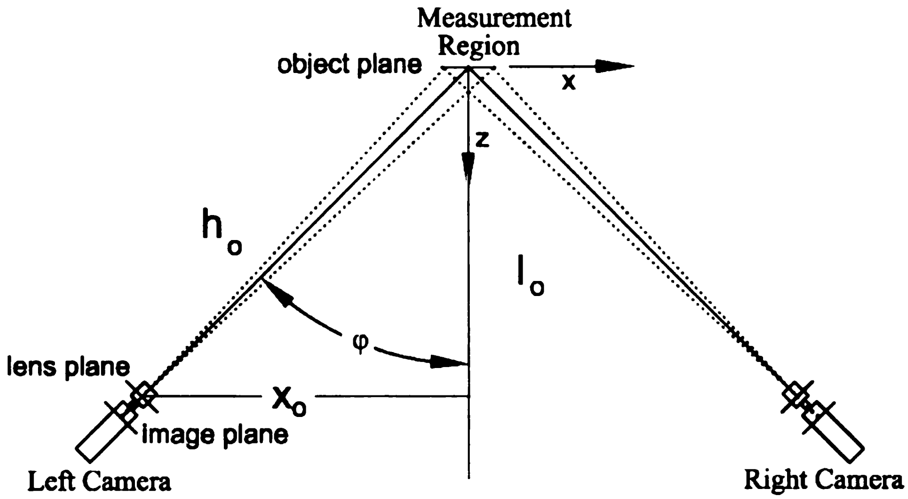

Figure 2-10: Schematic of angular displacement stereoscopic method. Distances and angles are derived independently for each camera.

reconstruction equations are also dependant upon the magnification ratio between the image and object planes. This method is "easy" to implement and provides very accurate results if there is no index of refraction change between the camera and image planes and the magnification is uniform across the image. In the presence of an index of refraction interface the geometric method still works well, although there is a systematic error across the image in the measured velocity components, see Bohl et al. (2001). Geometric relationships can also be determined for non-uniform magnification ratios, however they are significantly more complicated to derive and are specific to a given geometry.

2.3.2 Generalized Undistortion Reconstruction

The generalized undistortion method accounts for the imaging geometry of the system via calibration of the imaging system. The present implementation of the generalized undistortion method follows from the work of Solof et al. (1997) which described the method for a PIV system. The method described in that work is general in that it is independent of the planar method (i.e. MTV, PIV) used to provide the displacement measurements. It is also general in that methods other than the angular displacement method (e.g. the linear translation method) can be used with it.

First consider the transform relationship for a single camera. A location in space can be related to a location on the image array by the following relationship:

$$\mathbf{X} = \mathbf{F}(\mathbf{x}) \qquad (1)$$

where $\mathbf{X}$ is the image plane location, $\mathbf{x}$ is the real space location and $\mathbf{F}$ is a function that relates the two. The displacement recorded by the camera can be related to (1) by:

$$\Delta\mathbf{X} = \mathbf{F}(\mathbf{x} + \Delta\mathbf{x}) - \mathbf{F}(\mathbf{x}) \qquad (2)$$

A first order expansion of (2) gives the displacement as

$\Delta\mathbf{X} \approx \nabla$

where

$(\nabla F)_i$

In (4)

direct

plane

displa

solved

displa

displ

smal

vecto

$\Delta\mathbf{X}$

whe

writ

ΔY

whe

disp

disp

$$\Delta \mathbf{X} \approx \nabla \mathbf{F}(\mathbf{x}) \cdot \Delta \mathbf{x} \tag{3}$$

where

$$(\nabla F)_{i,j} = \frac{\partial F_i}{\partial x_j} = F_{i,j} \tag{4}$$

In (4) i represents the image plane directions (1,2) and j represents the real-plane directions which can, in general, be three (1,2,3). If the flow is 2-dimensional the third real plane direction drops out. In that case (3) can be solved to provide the real plane displacements using a single camera. If there is out-of-plane motion present (3) cannot be solved using a single camera because the number of unknowns, the real plane displacements dimensions, 3, outnumbers the number of knowns, image plane displacements dimensions, 2. In practice, the effect of three dimensionalities may be small, and equation (3) cane be used with good results to determine the in-plane velocity vector.

In a stereoscopic system (2) can be written uniquely for each camera as:

$$\Delta \mathbf{X}^{c} = \mathbf{F}^{c}(\mathbf{x} + \Delta \mathbf{x}) - \mathbf{F}^{c}(\mathbf{x}) \tag{5}$$

where c=1,2 represents the left and right cameras. The 3-component version of (4) is written as:

$$\Delta X_i^c \approx \nabla F_{i,j}^c(x_j) \cdot \Delta x_j \tag{6}$$

where i=1,2 (each camera in-plane displacement direction) and j=1,2,3 (real plane displacement direction). Equation (6) can be expanded to relate the image plane displacements to the real plane 3- component displacements as follows:

$$\begin{bmatrix} \Delta X_1^1 \\ \Delta X_2^1 \\ \Delta X_1^2 \\ \Delta X_2^2 \end{bmatrix} = \begin{bmatrix} F_{1,1}^1 & F_{1,2}^1 & F_{1,3}^1 \\ F_{2,1}^1 & F_{2,2}^1 & F_{2,3}^1 \\ F_{1,1}^2 & F_{1,2}^2 & F_{1,3}^2 \\ F_{2,1}^2 & F_{2,1}^2 & F_{2,1}^2 \end{bmatrix} \begin{bmatrix} \Delta x_1 \\ \Delta x_2 \\ \Delta x_3 \end{bmatrix} \qquad (7)$$

Equation (7) is solved for (Δx_j) via least squares fit. The real displacements, (Δx_j), are converted directly to real units (i.e. inches, cm, mm, etc.) by this transform.

The solution of (7) requires the establishment of the relationship between real space locations and image plane locations. This is done via calibration. In this work a calibration target with printed intersections at known spatial locations was placed into the flow field (Figure 2-11). The target was moved to and imaged at seven z planes, with the cameras held fixed, and a polynomial fit (4th order in x and y, and 2nd order in z) was created for each camera. The polynomial fits were differentiated to provide $F_{i,j}$ for use in (7). The function **F**, and its derivatives $F_{i,j}$ were smooth, slowly varying and well described by the polynomial fits (Figure 2-12).

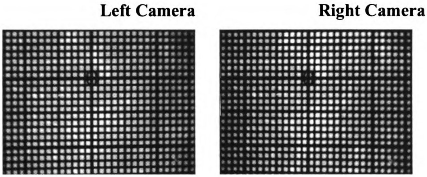
Left Camera **Right Camera**

Figure 2-11: Sample left and right image calibration grid at z=0.

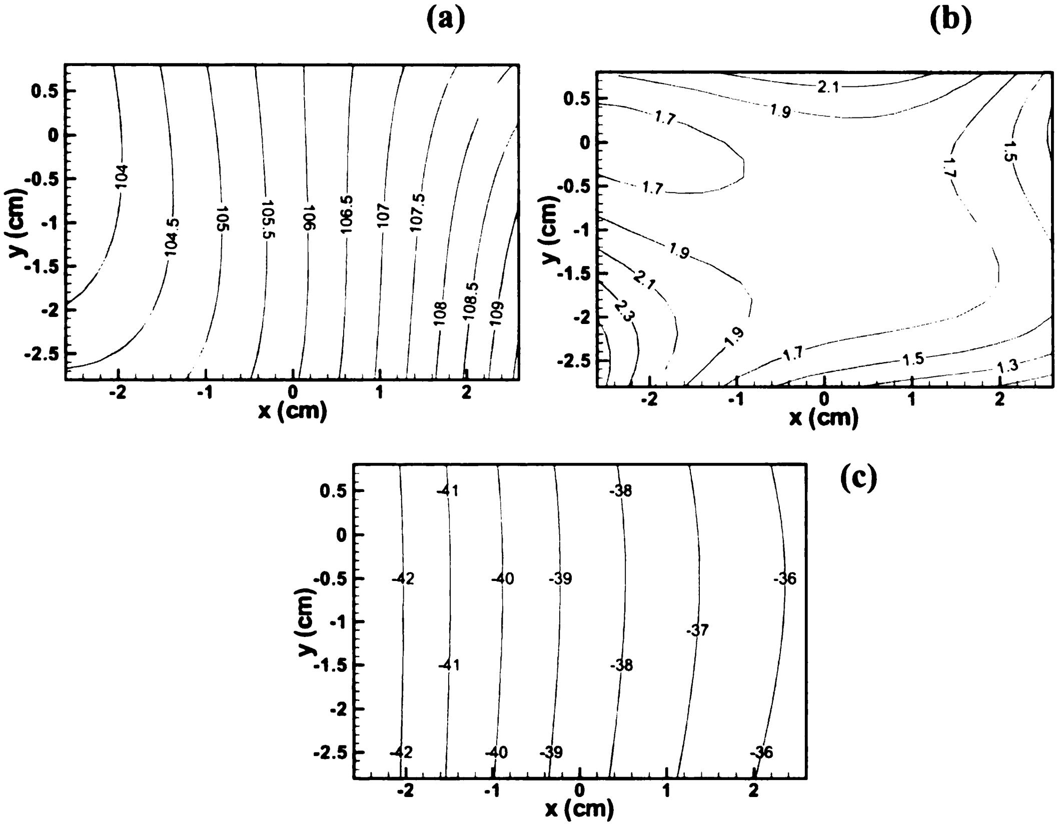

Figure 2-12: Representative derivatives of mapping function, F, for the right camera, x-direction. (a) $F^1_{1,1}$, (b) $F^1_{1,2}$, (c) $F^1_{1,3}$. Distances in real units (cm, mm, inches etc.). Derivative units are (pixels) / (real distance unit).

As discussed, this method automatically accounts for non-uniform magnification in the fit of the calibration data. The drawback of this method, compared to the geometric undistortion method, is a more complicated calibration procedure. In this study the non-uniformity in the magnification due to multiple index of refraction interfaces (see 2.3.4) makes the use of the generalized undistortion method more desirable.

2.3.3 sMTV Acquisition / Processing

The acquisition / processing of sMTV data was as follows: The laser sheet and grid intersections were created in the location to be studied in the same manner as the planar MTV in section 2.2.2. Camera timing and use was identical to that describe in section 2.2.3, except that two cameras were used and aligned for angular measurements as shown in Figure 2-10. The cameras were aligned so that the middle of the measurement domain occurred at the same location (i.e. the center of the image) on both image planes. A computer generated target with known grid spacing was placed into the test section at the same location as the laser grid (Figure 2-11). The was accomplished by moving the calibration grid in the z-direction until the center intersection was in the same pixel location for both cameras. This insured that the calibration grid for z=0, and the laser light sheet, occurred at the same z-plane. The grid was displaced 0±0.15 cm in steps of 0.05 cm. Maximum z-displacements were less than 0.10 cm during the delay times used. The target grid had a 0.2 cm Δx and Δy, which corresponded to the nominal laser grid spacing. Images were recorded by both cameras at each z location. The calibration grid intersections are correlated to provide the mapping of image to real coordinates. The calibration data are fit via least squares to determine the functions, F, from equation (1).

The calibration grid was then removed from the test area and data were acquired for each camera simultaneously. The images from each camera were processed separately using the standard planar MTV processing routine to provide the apparent velocity components for that perspective. Figure 2-13a,b shows an instantaneous velocity field for the left and right cameras in the technique validation flow field as discussed in section 2.3.4. It is instructive to note that the estimation of the out of plane velocity is primarily a function of the x-displacement. Comparison of Figure 2-13 a and b shows that the v-component was similar between the two cameras, while the u-component showed differences, as expected. Since each grid intersection was unique, the real-space starting

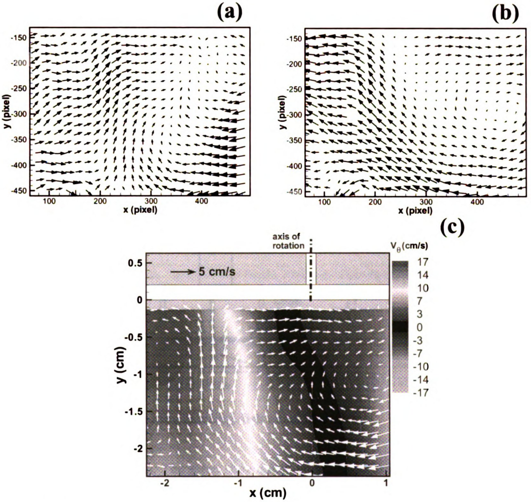

Figure 2-13: Instantaneous (a) left camera, (b) right camera, and (c) combined velocity field for flow under the rotating disk.

location for each intersection was determined and it's match found for the other camera. The data for the same intersection were combined as described in section 2.3.2 to provide the three component velocity measurement in the plane of the laser sheet, see Figure 2-13c. Data post processing (i.e. phase averaging, mapping to a regular grid, determination of vorticity, etc.) proceeded as with the planar technique.

2.3.4 sMTV Experimental Validation

Experimental validation of the technique was made in the flow under a rotating disk as shown in Figure 2-14. A detailed description of the sMTV validation can be found in Bohl et al. (2001). The setup shown in Figure 2-14 illustrates a rotating flat disk (radius R = 6.35 cm) inside a container of square cross section. A DC motor was used to rotate the disk at 250 RPM (±1 RPM) for all experiments. The rotating disk was located 3.2 cm (0.5R) above the bottom fixed wall. The region of the flow imaged here was characterized by primarily an azimuthal flow (maximum V_θ about 16 cm/s) and a weaker secondary flow (V_x and V_y typically 5 times smaller). The imaged region for 3-component measurements was in the (x-y) plane and was approximately 3.5 cm (in x) × 2.5 cm (in y), starting about 0.15 cm below the disk (outside of the Ekman boundary layer). The baseline reference data for this flow were obtained from the measurement of the (V_θ,V_x) velocity

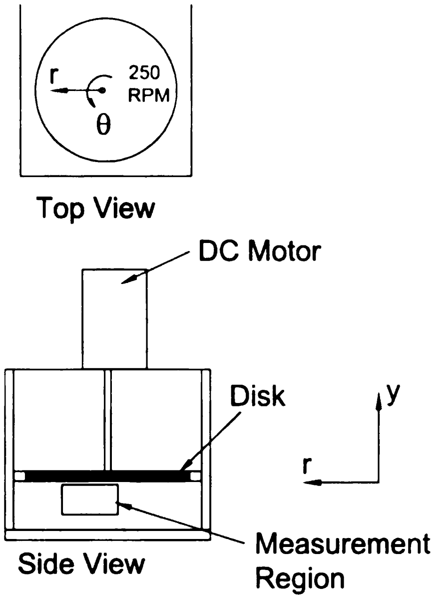

Figure 2-14: Schematic of the rotating disk experiment.

components over the (x-θ) plane at a given y distance away from the disk using standard 2-component MTV with viewing through the bottom of the test section. Because the out-of-plane velocity component (V_y in this case) was very small, accurate measurements of the in-plane velocity components (V_θ,V_x) could be made and used for comparison.

The approach just described allowed the comparison of velocity data (V_θ,V_x) between the stereo method and the measured reference data along the radial line defining the intersection of the two measurement planes. Since the two measurements were not carried out simultaneously, comparisons cannot be provided on the basis of the instantaneous velocity data. Instead, the mean and rms fluctuation of the velocity data computed from 7200 realizations were compared. The comparison of the mean and rms profiles of the primary velocity component V_θ is illustrated in Figure 2-15 with excellent agreement between the profiles measured by the stereo method and the reference data.

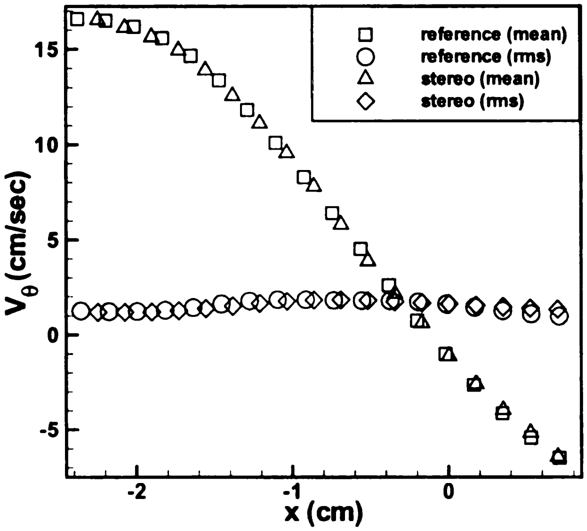

Figure 2-15: Comparison of V_θ from stereoscopic MTV with planar reference MTV data. Data at y = -0.43 cm

2.3.5 sMTV Optical Issues

Implementation of the angular stereoscopic method in the current work was complicated by several index of refraction surfaces (i.e. air / acrylic and water / acrylic) . The most significant refraction occurred for the air/acrylic interface on the outside of the water tunnel because the measurement plane was viewed at an angle with respect to the tunnel sidewalls. All other interfaces were parallel refractions which had much less significance to the imaging characteristics of the system. A liquid prism was employed to compensate for the refraction due to the air / acrylic interface (Figure 2-16). The walls of the liquid prism were made of acrylic and the working fluid was water. The liquid prism allows light rays to make the air-acrylic transition at nearly 90° which eliminated the refraction at interface and increased the image quality.

2.3.6 sMTV Error Estimation

The error level in a stereoscopic measurement is dependant upon the error in the base planar technique and the set-up of stereo imaging system. The error in the angular stereoscopic method is dependent specifically upon the angle between the cameras. Analysis of the error as a function of the camera angle, φ, (as defined in Figure 2-10) using the geometric reconstruction equations, is shown in Figure 2-17. The ratios of the in-plane component and out-of-plane component errors to the measurement correlation error (i.e. the planar technique error) are plotted as a function of the camera angle, φ. The camera angle used in this work was nominally 17° due to optical limitations. The error ratio of out-of-plane to correlation error for this camera angle was approximately 3:1. The corresponding error ratio for the in-plane component to the correlation error is 1:1. Given the correlation error estimate discussed in section 2.2.2 of 0.17-0.24 pixels (0.4 - 0.6 cm/

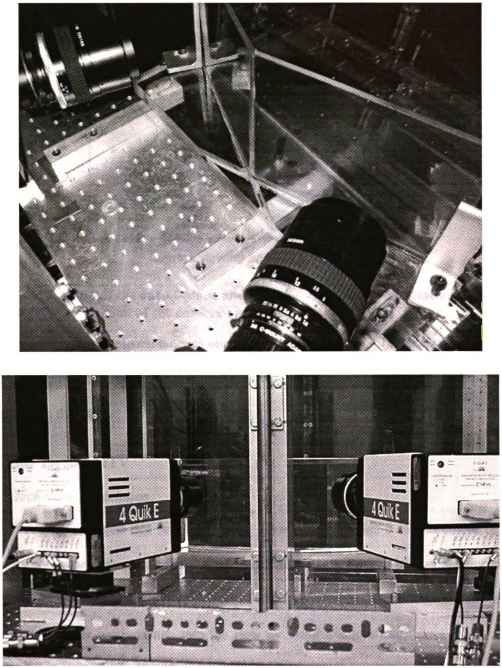

Figure 2-16: Stereoscopic camera set-up with liquid prism.

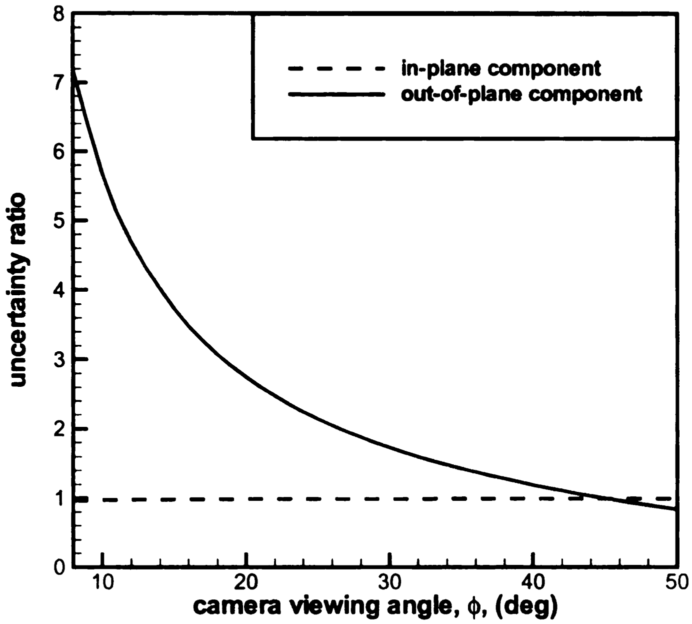

Figure 2-17: Ratio of the out-of-plane and in-plane error to the correlation technique error level as a function of the camera angle, φ.

sec), the corresponding instantaneous out-of-plane error was 0.5 - 0.7 pixels (1.2 - 1.8 cm/sec), respectively. For reference, out-of-plane velocities of up to 15 cm/sec were measured in this study.

2.4 Line Tagging MTV

2.4.1 Technique Description

A single tagged line written into the flow field provides a measurement of the velocity component perpendicular to the line. Initial measurements of the axial flow speed in this study were made using a single tagged line viewed from the downstream end of the test section. Lines were written into the flow by using a single laser sheet (rather than splitting the sheet with a 50/50 beam splitter as shown in Figure 2-5) and beam blockers. The lines were passed vertically into test section (i.e. normal to the bottom surface of the tunnel). The tagged lines were imaged from the downstream end of the tunnel, camera c in Figure2-2. Undelayed and delayed images of the single tagged line were acquired with a single intensified camera using the timing described in Figure 2-6 with delay times of 16 ms and gate periods of 0.14 and 2.3 ms. Displacement normal to the tagged line indicates spanwise, z-component, flow in this orientation, see Figure 2-18.

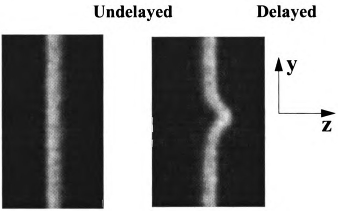

Figure 2-18: Example of undelayed and delayed lines for a single tagged line. Delay time: 16 msec; A=2°, k= 11.5; x=0.85c, z=0.85c.

The data were processed to provide the spanwise velocity component (w) via the following method: The location of highest intensity was found to the nearest pixel for each row in an image. The intensity profile was fit using a polynomial, typically 2nd order, using the intensity from the 5 pixels on each side of the maximum intensity location (Figure 2-19). The center of the lines in the undelayed and delayed images were determined by finding the maximum of the fit polynomials. The displacement was taken to be the difference between the peak intensity locations in the delayed and undelayed images. The resulting displacement was scaled, using the magnification ratio and delay time, to provide the dimensional velocity. The procedure was carried out for each row in the image.

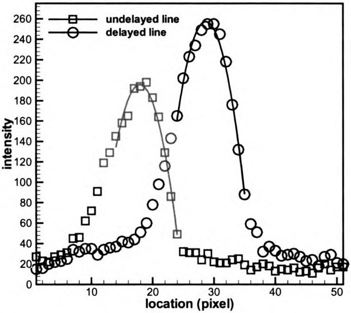

Figure 2-19: Intensity profiles taken from Figure 2-11, in the region spanwise displacement . Curves shown are best fit 2^{nd} order polynomial to ± 5 data points about the peak intensity location.

2.4.2 Error Analysis

There were two sources of error in the line tagging measurements. They were measurement error, and error due to flow velocities in the direction parallel to the beam. The measurement error level could be characterized by investigating regions in the flow where there was no spanwise displacement measured and determining the noise in the measurements in those locations. The phases that corresponded to the two vortices passing through the measurement location, and the resulting spanwise axial core flow, are shown in Figure 2-20. The two vortices are differentiated by the line colors. Figure 2-20 highlights the localized axial core flow and the near zero spanwise flow outside of the vortex cores. Estimates for the measurement error taken from the near zero spanwise flow region were 0.35 cm/s for the phase averaged data.

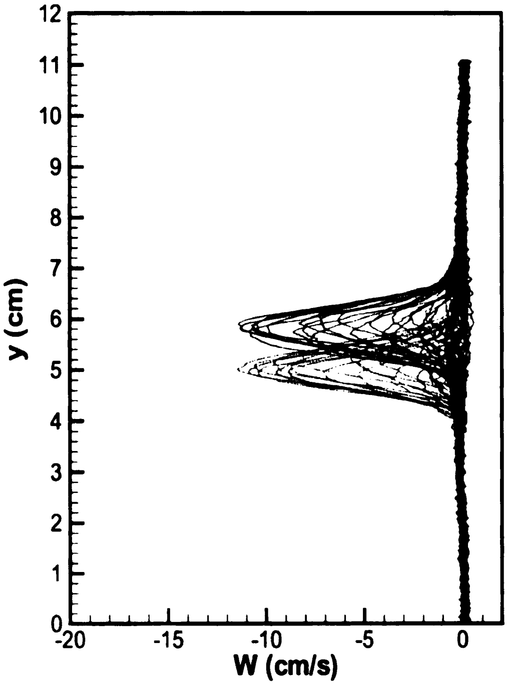

Figure 2-20: Phase averaged spanwise flow profiles for vortex / side wall interaction. A=2°, k=2.84; x=1.27c, z=0.85c.

The second source of error in the line tagging measurements was due to flow velocities in the direction of the tagged line. Molecular tagging techniques rely upon a difference in contrast to provide the spatial location of the tagged region. A single tagged line provides contrast only in the direction perpendicular to the line. Along the direction parallel to the line there will be no change in contrast, neglecting beam attenuation issues, and therefore no spatial location information can be determined in this direction. The intersecting lines used in the planar and stereoscopic techniques provide a 2-dimensional contrast field in a region where two lines intersect, thus limiting the possible measurement locations to those regions. Hill and Klewicki (1994) discusses this issue and provide an estimate for this error. An equation for the error estimate was adapted from Hill and Klewicki (1994) and is given by the equation:

$$\frac{\Delta w}{w} = \tan\theta\left(\frac{\partial w}{\partial y}\right)\Delta t \qquad (8)$$

In (8) w is the estimated velocity component perpendicular to the tagged line, Δw is the error in the estimated velocity, θ is the local flow angle (tanθ is therefore v/w if v is the velocity component parallel to the tagged line) and Δt is the delay time for the measurement. The error is clearly a function of the flow investigated, and knowledge of the flow field is required to determine the error level.

Figure 2-23 shows a simulation of the effect of this error on a vortical flow field similar to those measured in this work for illustration. In Figure2-23(a) the real flow field of an Oseen vortex with a Gaussian distribution of axial flow is shown. Figure 2-23(b) shows the flow field that would be measured given equation (8). In this work, the phase averaged **peak** spanwise velocity, $<w>_{peak}$, will primarily be reported for the line tagging data. The spatial location of this velocity should be relatively coincident to the center of the vortex and should, therefore, have the least error due to the vertical velocity. Lateral velocities at other phases (i.e. locations different to the vortex center) will, however, be affected.

2.5 Data Acquisition

Each MTV data run was composed of 1000 measurements (i.e image pairs) at a data rate of 30Hz. The SCO cameras used in this study provided an image that was 640x480 pixels in size. Typical FOV's were 4cm x 3cm in extent. Between 350 (stereoscopic) and 500 (2-D planar) grid intersections were placed into this spatial region. Multiple FOV's were taken and later combined in phase space to increase the data spacing, as recommended in Cohn and Koochesfahani (2001), to limit the systematic error

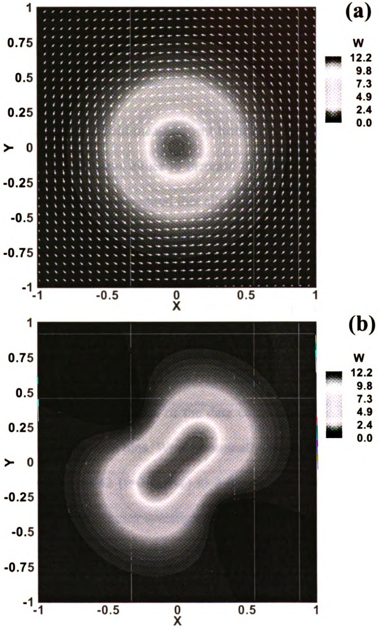

Figure 2-21: Simulation of an Oseen vortex with a Gaussian distribution of axial flow (a) and the expected measured axial velocity distribution considering equation (8) (b).

in the calculation of the vorticity. Different FOV's were combined and the data were re-mapped into regularly spaced data points. Other flow properties, e.g. vorticity and strain, were calculated at this point.

2.6 Phase Averaging

While MTV is a whole field measurement technique, it was necessary at times to investigate multiple fields of view, either to increase the spatial extent of the data or to increase the spatial resolution. One method that allows multiple data sets to be combined into a single data set is phase ordering/averaging the data sets. In this study the data were sufficiently repeatable from cycle to cycle that measurements from different airfoil oscillation cycles could be combined relative to the reference motion of the airfoil, or the airfoil phase, ϕ and discussed as representative of the instantaneous flow field. Phase averaging the data has several desirable effects on the data processing for this problem. By phase averaging the temporal resolution of the data could be increased. The data were ordered and divided into 64 phase bins. With a nominally 30 Hz data rate, the number of points per cycle ranged from 42 (f=0.71 Hz) to 8 (f=3.55 Hz) for the frequency range investigated. None of the frequencies investigated was an integer multiple of the camera framing rate so the camera frames would move relative to the airfoil motion populating the entire cycle. The cycle was broken down into finer phase (temporal) spacing than allowed by the camera framing rate.

Phase averaging allows the individual measurement error to be reduced by averaging the measurements within the phase bin to determine the phase averaged value for that portion of the phase. There were typically 16 realizations per phase bin which reduced the measurement error level by a factor of 4. Phase averaged noise levels were therefore be 0.1-0.15 cm/sec for the planar measurements as well as the in-plane portion of the stereoscopic measurements while the corresponding out-of-plane measurement error was 0.3-0.45 cm/sec.

The airfoil trajectory shown earlier in Figure 2-3 is the phase ordered airfoil AOA for the time series data and indicates the repeatability of the airfoil motion. The phase, ϕ, was normalized to run from 0 to 1 rather than 0 to 2π. Figure 2-22 shows the phase ordered velocity for the u and v components at an arbitrary spatial location for the A = 2°, k = 11.0 case from a planar MTV measurement. The width of the velocity band and the bin RMS levels (i.e. the RMS of the points that were contained in a bin 1/64th of a cycle wide at a given spatial location) were nominally 1.5 cm/s and 0.4 cm/s respectively. These data showed both the cycle to cycle variation, the effect of averaging over a finite portion (1/ 64th) of the phase, as well as experimental noise. The phase, $\phi=0$, will be defined as an airfoil angle of attack (AOA) of zero degrees with the AOA decreasing (i.e. airfoil pitching down) for this work.

Figure 2-23 shows typical measurement FOV boundaries from the individual experiments. The use of phase averaging allowed the creation of a spatially large, phase resolved (i.e. pseudo instantaneous) data field over the entire spatial region shown in Figure 2-23. The increased spatial data extent allows the development of the flow field to be examined continuously in space.

2.7 Calculation of Statistical Quantities

In this work the mean and RMS levels for the oscillating cases were calculated from the phase averaged data. Specifically, the data were re-ordered with the phase information then phase averaged as described above. The large FOV data sets were

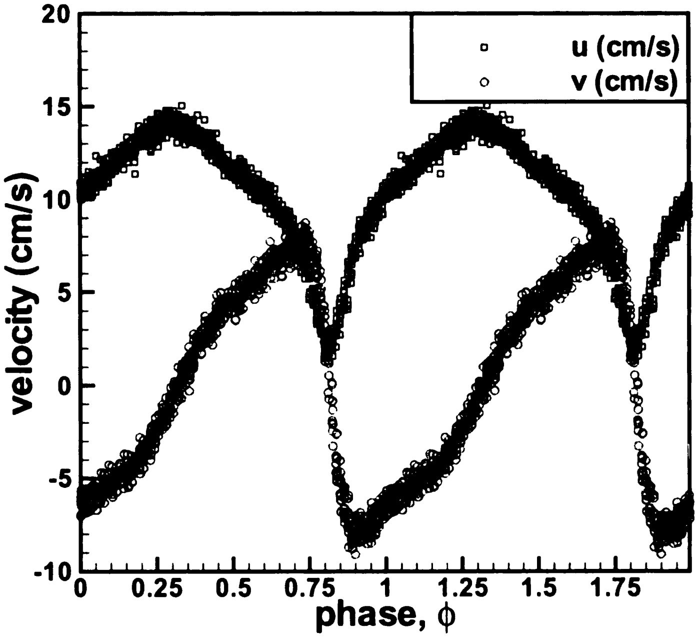

Figure 2-22: Phase ordered u and v velocity components for the 2 degree, k=11 case at x=6 cm downstream of the trailing edge. Note 2 cycles are shown.

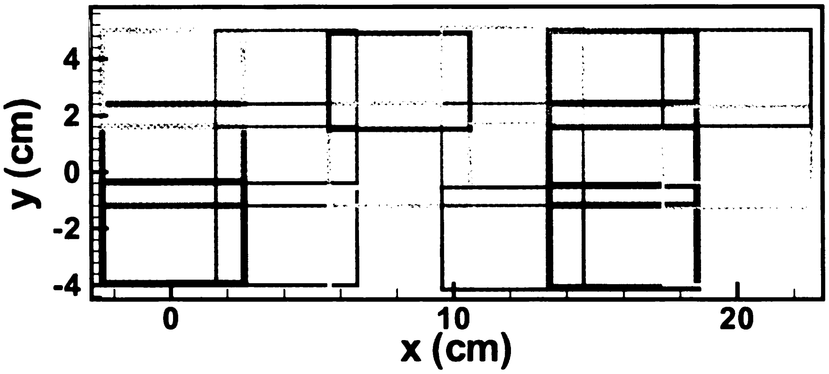

Figure 2-23: Sample map of experiment fields of view combined to create large data sets in phase space.

created by combining the smaller FOV phase averaged data sets and the mean and RMS level were computed by averaging the data in phase space. These statistical quantities were therefore different from the long time average and RMS, however, because the phases were nearly equally populated the differences were negligible. The statistical quantities for the static airfoil case was computed using the complete time series. The large FOV data for the static case was created by combining the small FOV statistical data.

CHAPTER 3

CENTERSPAN PLANAR MEASUREMENTS, NO CUTTING WALLS

Standard 2-D planar MTV measurements have been made at the center span of the tunnel over a distance of -1 cm < x < 13 cm (-0.08c < x < 1.08c) downstream of the trailing edge of the airfoil without the cutting walls present, see Figure 1-4 with the free stream speed, U_{∞} = 10.5 cm/sec. Data from multiple FOV's were combined to generate a data set over the range -4 cm < y < 4 cm (-0.33c < y < 0.33c) for -1 cm < x < 13 cm (-0.1c < x < 1.08c) with two exceptions: first, for the range 10 cm < x < 13 cm, additional data were taken to increase the lateral range of y to ±8 cm (±0.67c). This allowed free stream information to be gathered. Second, near the trailing edge of the airfoil, portions of the laser lines were blocked by the airfoil, and therefore data were not available in that region. The areas where data were not available are marked by dashed lines in the figures of this chapter.

The data in this chapter are subdivided into two sections, static and oscillating airfoil cases. The static airfoil data were acquired at A=0°, the mean airfoil angle of attack for the oscillating cases. These data provide contrast to the oscillating cases, emphasizing the dynamic nature of the flow field. The mean flow fields of the oscillating cases are first discussed followed by the "instantaneous" phase averaged flow fields. Three reduced frequencies, k=5.2, 5.7, and 11.5 are considered in this section of the work. The k=5.2 and 11.5 cases are the cases that will be investigated in detail with the cutting walls. The k = 5.7 case is included because the vortex array is aligned vertically giving a nominal zero mean thrust. An additional case, k = 4.1, is included in the discussion of the phase averaged flow field because the formation process was significantly different at this low reduced frequency. The spatial evolution of two reduced frequencies, k = 5.2 and 11.5 for

A=2°, will be discussed in detail. Vortex array properties (peak vorticity, circulation, core radius, convection speed, etc.) will be discussed for the vortex arrays at x = 6cm downstream, where the cutting walls will be placed, for all cases.

3.1 Static Airfoil Characteristics

Figure 3-1 shows the mean u, v and ω_z fields, along the centerspan of the facility, in the wake of an airfoil held fixed at an AOA=0°. The vorticity shown in Figure 3-1 was calculated from the mean velocity field. The mean streamwise velocity was slightly greater than the freestream speed ($\bar{u} \approx 1.04U_\infty$) above the airfoil and outside of the airfoil boundary layer. The average streamwise velocity then relaxed to the freestream level for $x > 0.5c$. This was expected given the decreased tunnel area caused by the airfoil section and the wake deficit. The velocity in the wake directly behind the trailing edge of the airfoil ($x < 0.1c$) was nearly zero ($\bar{u} \approx -0.04U_\infty$). The velocity deficit was clearly indicated by the vector field, Figure 3-2(a). The weak reverse flow in the wake was observed, when the vectors were scaled to a uniform length regardless of their magnitude. That is a recirculation region was observed, Figure 3-2(b). Note that the data in Figure 3-2 are the irregularly spaced data before they were re-mapped onto a regular spaced field. These data are used in the vicinity of the airfoil surface to minimize re-mapping artifacts due to lack of resolution in the airfoil boundary layer. Figure 3-3 is a flow visualization image taken using the MTV chemical triplex. The recirculation region was indicated in this image by the relatively bright region below and in the wake of the airfoil. The separation point was marked by the boundary of the luminescent fluid/dark fluid at the airfoil surface. In this region it was believed that the concentration of free bromonaphthalene was increased, due to absorbtion and release from the airfoil, allowing it to be visualized. The transverse, $\bar{v}$,

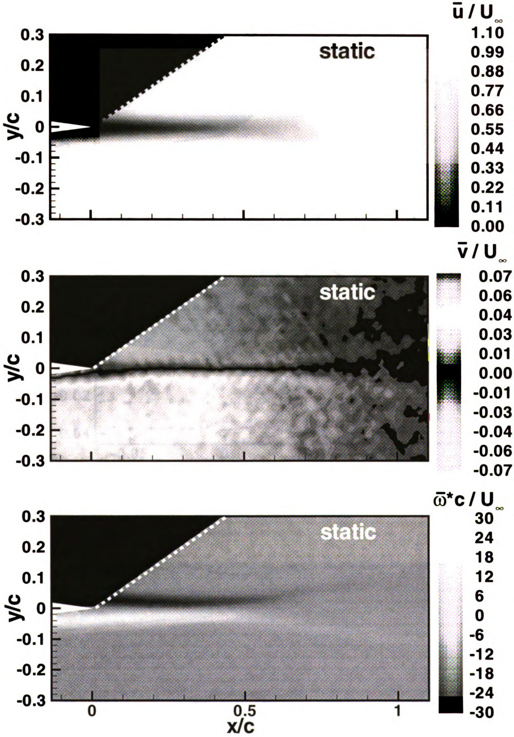

Figure 3-1: Mean u, v and ω_z fields for the stationary airfoil at AOA=0°, tunnel midspan.

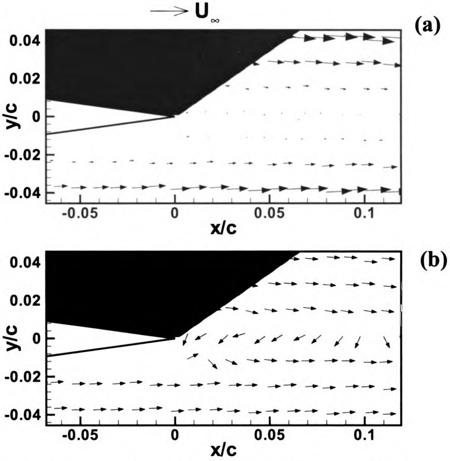

Figure 3-2: Mean velocity vectors in the near wake of the static airfoil. (a) vector length proportional to velocity, (b) vector length uniform.

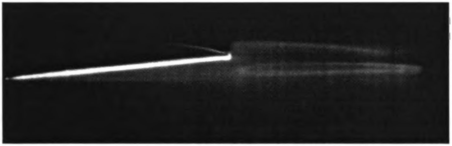

Figure 3-3: Flow visualization of recirculation bubble in the near wake of a stationary NACA-0012 airfoil at AOA=0°.

velocity showed the flow being directed first towards the centerline of the shear layer downstream of the airfoil trailing edge then becoming predominantly streamwise, $\overline{v} \approx 0$, for $x > c$ (Figure 3-1). Near the airfoil surface the recirculation region was shown by the $\overline{v}$ directed away from the surface of the airfoil (Figures 3-1 and 3-2).

The mean vorticity, $\overline{\omega}_z$, was initially high in the boundary layer, and reducing in magnitude with increasing downstream distance (Figure 3-1). Note that the velocity at the airfoil surface was not used as a boundary condition in the velocity re-mapping (from irregularly spaced to regularly spaced data), therefore the actual vorticity in the boundary layer near the airfoil surface was underestimated.

At $x \approx 0.6c$ the structure of the $\overline{u}$ and $\overline{\omega}_z$ fields changed with the wake showing a decreasing width from $x = 0$ to $x \approx 0.6c$. The minimum wake width was found at $x \approx 0.6c$. The width of the wake region then increased for $x > 0.6c$ with a marked decrease in the sharpness of the velocity deficit profile. The $\overline{\omega}_z$ field also showed this change in the structure, i.e., a lateral spreading and a decrease in magnitude. Profiles of the same data are shown in Figure 3-4 for $x = 0.5c$ and $1.0c$ to clarify the current discussion by illustrating the average vorticity decrease, and wake width increase.

The RMS fields are shown in Figure 3-5 for the same measurement area. The wake directly downstream of the airfoil trailing edge showed low RMS levels ($\approx 0.05U_\infty$). Peak RMS of nominally $u_{RMS} = 0.16U_\infty$ and $v_{RMS} = 0.18U_\infty$ occurred at $x = 0.6c$ downstream. The RMS streamwise, u_{RMS}, velocity showed two local regions of high fluctuations symmetrically placed about the $y = 0$ line. A single RMS peak was shown for v_{RMS}. The downstream locations of the RMS peaks correlated with the change in the mean field structure noted above.

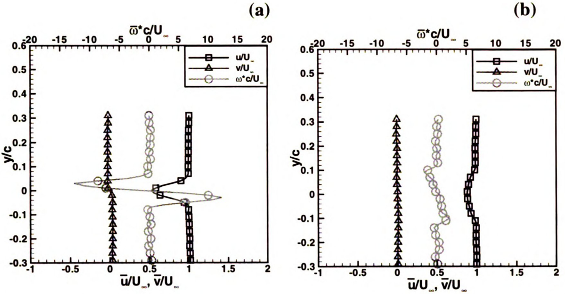

Figure 3-4: Profile of $\overline{u}$, $\overline{v}$ and $\overline{\omega}_z$ for the stationary airfoil at x=c/2 (a) and x=c (b), midspan. Every 3rd point shown.

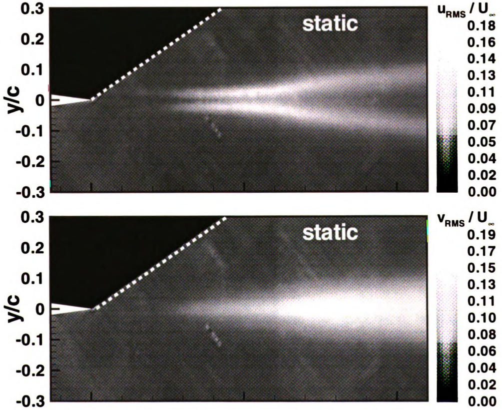

Figure 3-5: RMS u and v fields for the stationary airfoil at AOA=0°, tunnel midspan.

3.2 Oscillating Airfoil

3.2.1 Time Averaged Data

Mean streamwise velocity, $\bar{u}$, fields for the A = 2°, k = 5.2, 5.7 and 11.5 the oscillating cases are shown in Figure 3-6. The airfoil shown in the following figures is shown at an AOA of 0°, which for the oscillating airfoil represents the mean location of the airfoil. The $\bar{u}$ field for the A = 2°, k = 5.2 case showed a velocity deficit downstream of the airfoil with a nominally constant (in x) minimum mean velocity, $\bar{u} \approx 0.85U_{\infty}$, in the wake for $x > 0.4c$ and extending past the measurement range (Figure 3-7). The y-profiles revealed an overshoot in the streamwise velocity above and below the wake before the velocity relaxed to the freestream speed (Figure 3-8). The mean u field for the A = 2°, k = 5.7 case showed a small velocity deficit for $0.2c < x < 0.6c$ (Figure 3-7). For $x > 0.5c$ the velocity profile in the y-direction was nearly uniform (Figure 3-8). A large velocity excess was observed in the wake for the A = 2°, k = 11.5 case in contrast to the velocity deficit observed for k=5.2. The switch from a mean streamwise velocity deficit to a mean velocity excess is an indicator of a switch from an airfoil with mean drag to one with mean thrust (Koochesfahani, 1989). The k=5.7 case, which showed a nominally uniform mean streamwise velocity profile, was indicative of a net zero drag case, if only mean streamwise velocity was considered. A complete discussion of the mean drag characteristics of the measured airfoil is found in Section 3.2.2.

The qualitative aspects of the mean streamwise velocity, $\bar{u}$, field can be described by the orientation of the vortices with respect to each other. The following discussion is not unique. Similar discussions can be found, for example, in Lighthill (1975) and Koochesfahani (1989). Consider a vortex and the two closest vortices of the opposite sign.

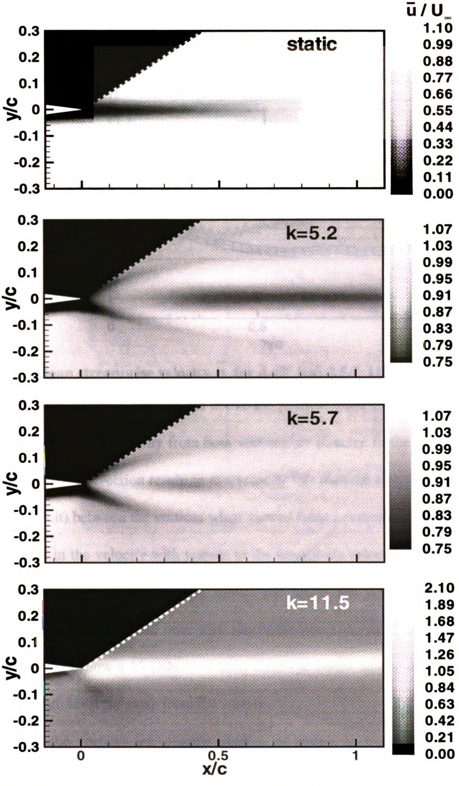

Figure 3-6: Mean of all phases streamwise velocity, $\bar{u}$, field for the A = 2°, k = 0, 5.2, 5.7 and 11.5. Note scale change for k=11.5

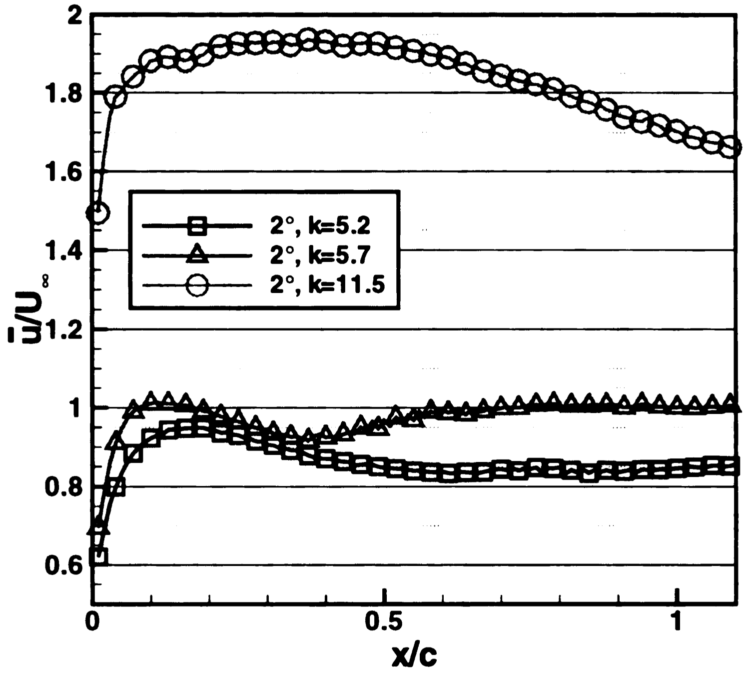

Figure 3-7: Mean streamwise velocity, $\bar{u}$, for A=2° k=5.2 5.7, 11.5 at y=0.

In Figure 3-9 the negative vortices are above the positive vortex. Between the vortices the induced streamwise velocity from both vortices are directed in the direction opposite of the direction of convection resulting in a velocity less than the freestream velocity (i.e., a velocity deficit) between the vortices when viewed from a stationary coordinate system. The overshoot in the velocity with respect to the freestream velocity is also predicted by this geometric argument. Specifically, above and below the vortex array the induced velocity from the vortices will sum with the freestream velocity. The induced velocity from the vortices follow a 1/r reduction away from the vortex and so the flow will return to the freestream level far away from the vortices.

When the vortices are exactly aligned, as shown in Figure 3-10, the induced velocities due to each vortex cancel, and the mean streamwise velocity profile is uniform across the vortex array. Figure 3-11 shows the case where the vortex orientation has

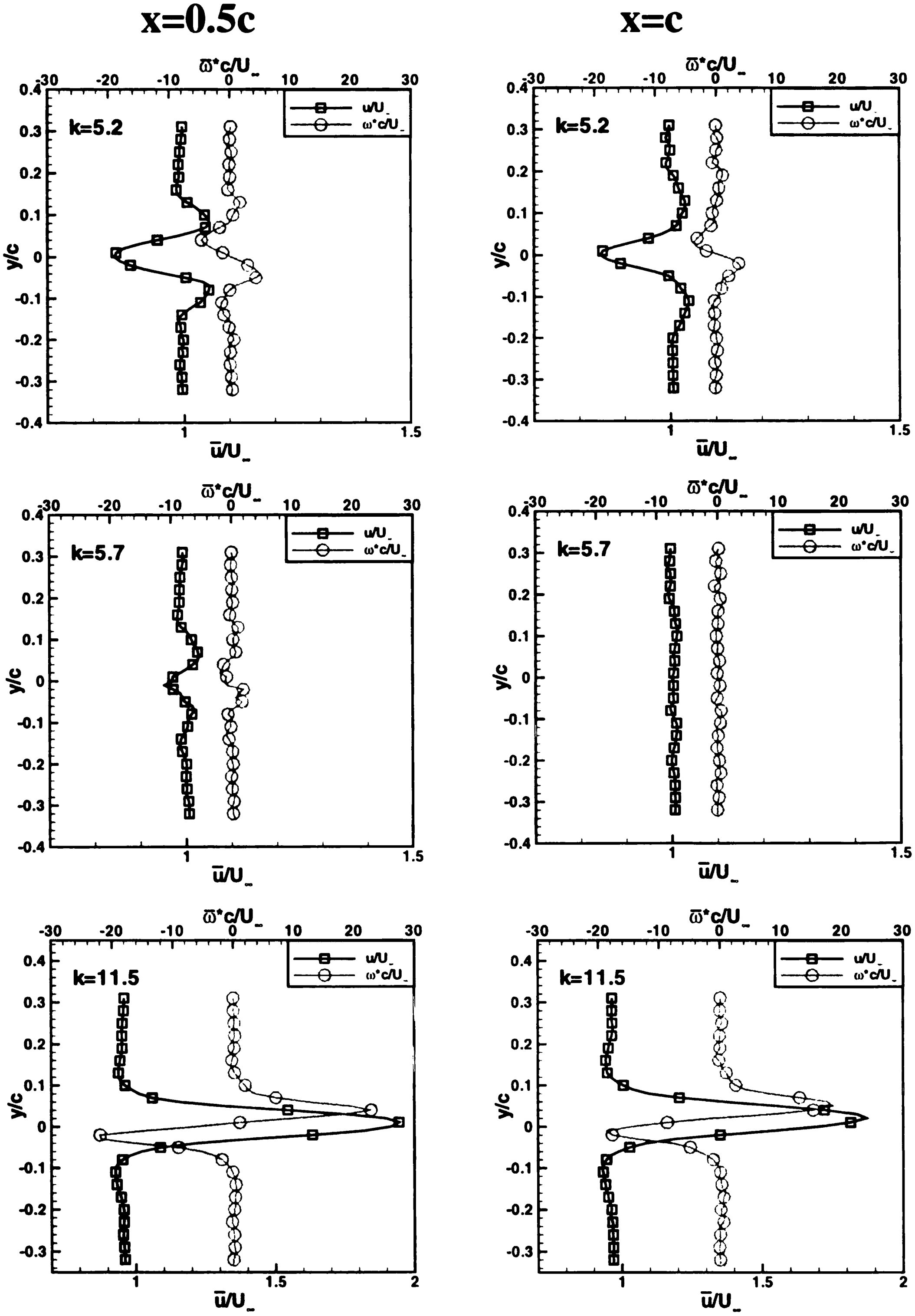

Figure 3-8: Mean streamwise velocity, $\bar{u}$, and vorticity, $\bar{\omega}_z$, profiles for A=2° k=5.2 5.7, 11.5 at x=0.5c, c.

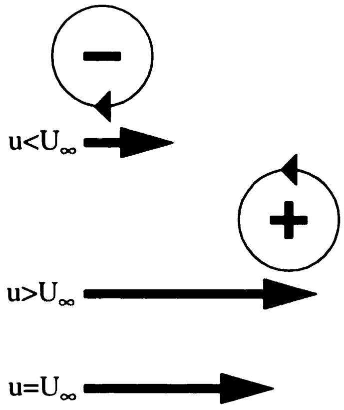

Figure 3-9: Schematic of the vortex orientation for the velocity deficit cases.

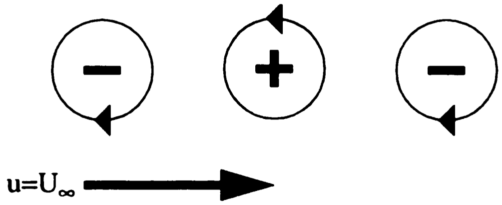

Figure 3-10: Schematic of the vortex orientation for uniform mean streamwise flow case.

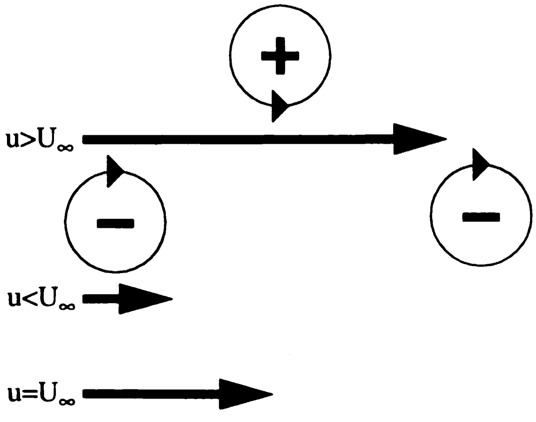

Figure 3-11: Schematic of the vortex orientation for the velocity excess cases.

r

w

os

vo

vo

vor

sho

infe

vort

obser

show

was a

trailing

switched. In this orientation the induced streamwise velocity between the vortices adds to the freestream speed, and a velocity excess, or jet-like profile is observed. An undershoot above and below the vortex array is also predicted, in contrast to the velocity deficit case. The mean lateral velocity, $\bar{v}$, is shown in 3-11.These data also showed that the mean velocity was directed towards the y=0 plane as was also observed for the static airfoil. The maximum $\bar{v}$ levels increased with increasing k. The downstream distance over which non-zero $\bar{v}$ was found decreased with increasing k. The lack of mean $\bar{v}$ downstream of the airfoil was expected for this flow field regardless of the orientation of the vortices with respect to each other. Specifically, the induced v velocity fluctuations from each vortex will sum to zero, causing a net zero $\bar{v}$ if the orientation of the array pattern is fixed.

The mean spanwise vorticity, $\bar{\omega}_z$, field for the A = 2°, k = 5.2, 5.7 and 11.5 the oscillating cases are shown in Figure 3-13. The k = 5.2 case showed the mean spanwise vorticity, $\bar{\omega}_z$, in the wake to have the same orientation as $\bar{\omega}_z$ in the boundary layer, i.e. the vorticity from the top (y positive) boundary layer of the airfoil remained above the vorticity from the bottom boundary layer of the airfoil in the wake. The k = 5.7 case showed very little $\bar{\omega}_z$ for $x > c/2$. This result indicated that the vortices were aligned as inferred from the mean streamwise velocity profile. The k = 11.5 case shows the expected vorticity orientation change which was also consistent with the jet like profile in $\bar{u}$ observed.

Fluctuating u and v velocity and spanwise vorticity fields for the above cases are shown in Figures 3-14, 3-15, and 3-16, respectively. The RMS streamwise velocity, u_{RMS}, was a maximum upstream of the trailing edge of the airfoil. Downstream of the airfoil trailing edge the u_{RMS} levels in the vortex sheet ranged from $0.2U_\infty$ to $0.6U_\infty$ and

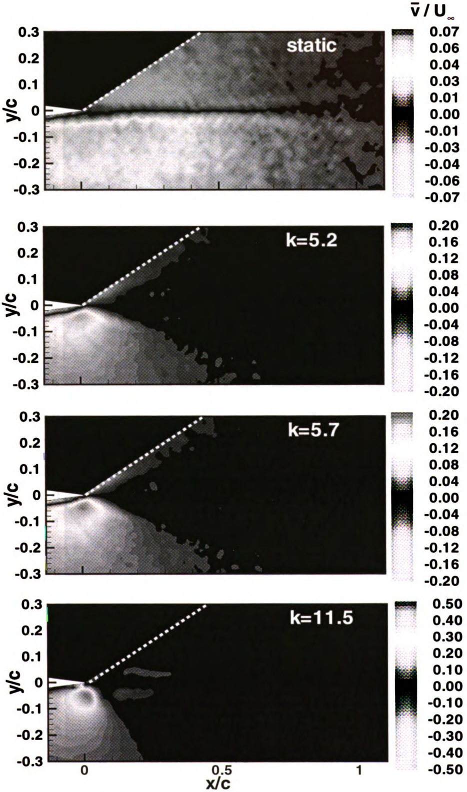

Figure 3-12: Time averaged mean v velocity field for the A = 2°, k = 0, 5.2, 5.7 and 11.5.

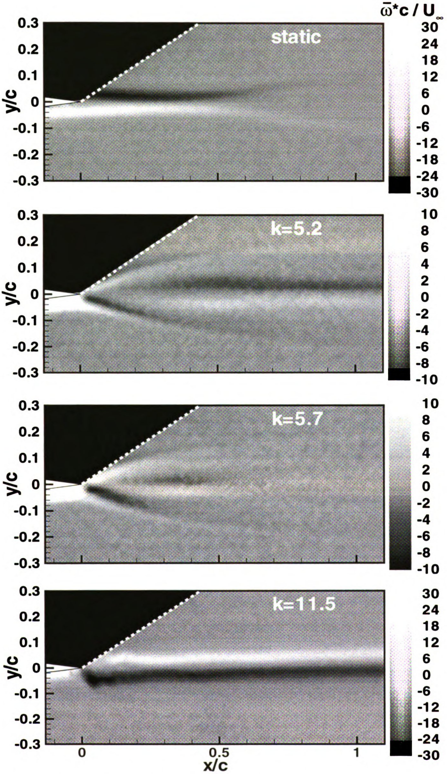

Figure 3-13: Mean spanwise vorticity, $\overline{\omega}_z$, field for the A = 2°, k = 0, 5.2, 5.7 and 11.5.

Figur

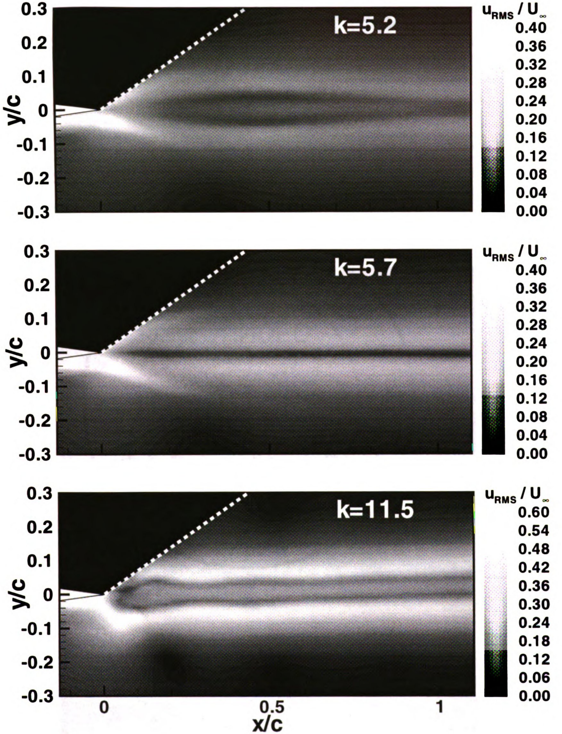

Figure 3-14: RMS u velocity field for the A = 2°, k = 5.2, 5.7 and 11.5 oscillating cases.

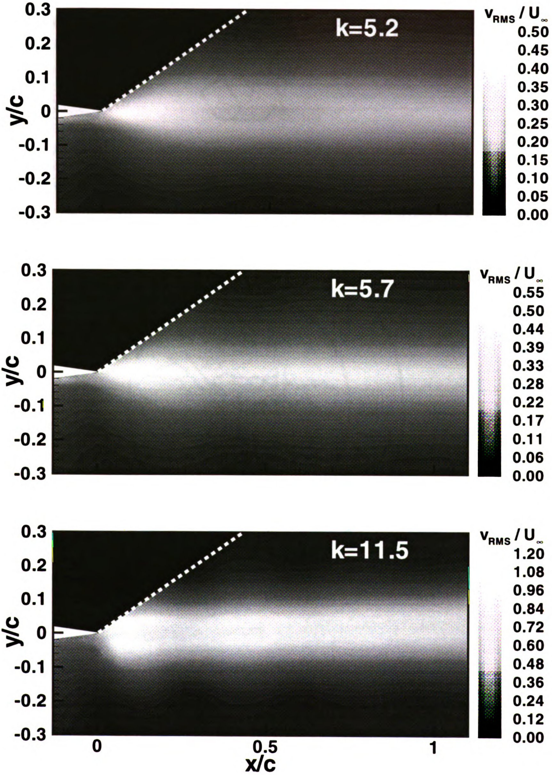

Figure 3-15: RMS v velocity field for the A = 2°, k = 5.2, 5.7 and 11.5 oscillating cases.

Figur
oscilla

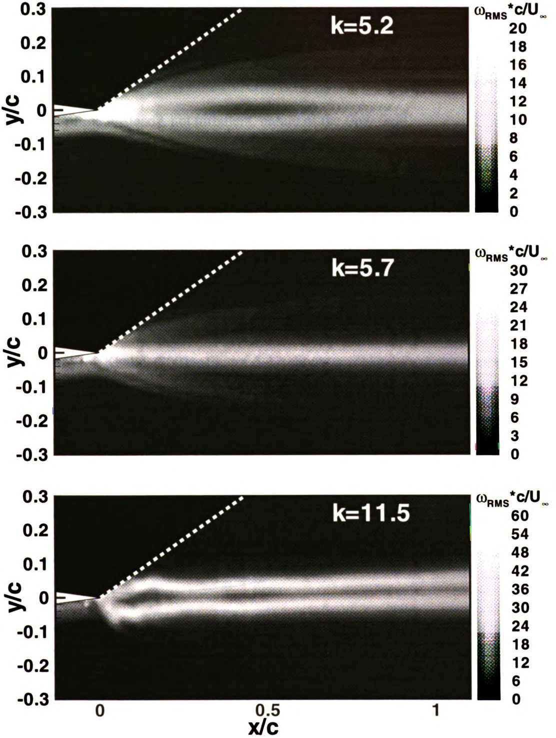

Figure 3-16: RMS spanwise vorticity, ω_z, field for the A = 2°, k = 5.2, 5.7 and 11.5 oscillating cases.

t

v

l

w

3.

vc

ch

me

ind

(1

Figur

increased with increasing k. The RMS lateral velocity, v_{RMS}, levels showed magnitudes that ranged from $0.3U_\infty$ to $0.9U_\infty$ and also increased with increasing k. RMS spanwise vorticity, ω_z, levels were 2 to 3 times larger than the mean levels in the wake. The RMS levels indicated a highly fluctuating flow field; However it is instructive to note that this was a result of the unsteady, not turbulent, nature of the flow field.

3.2.2 Mean Force Calculation

Force on an immersed object can be calculated using a combination of control volume and differential analysis on the flow field. Initial analysis of the drag characteristics on the current data was reported in Khalid (2001). The development of the mean thrust, C_F, equations used in this work can be found in Appendix A and were derived independently of Khalid (2001). Figure 3-17 shows a schematic of the control volume

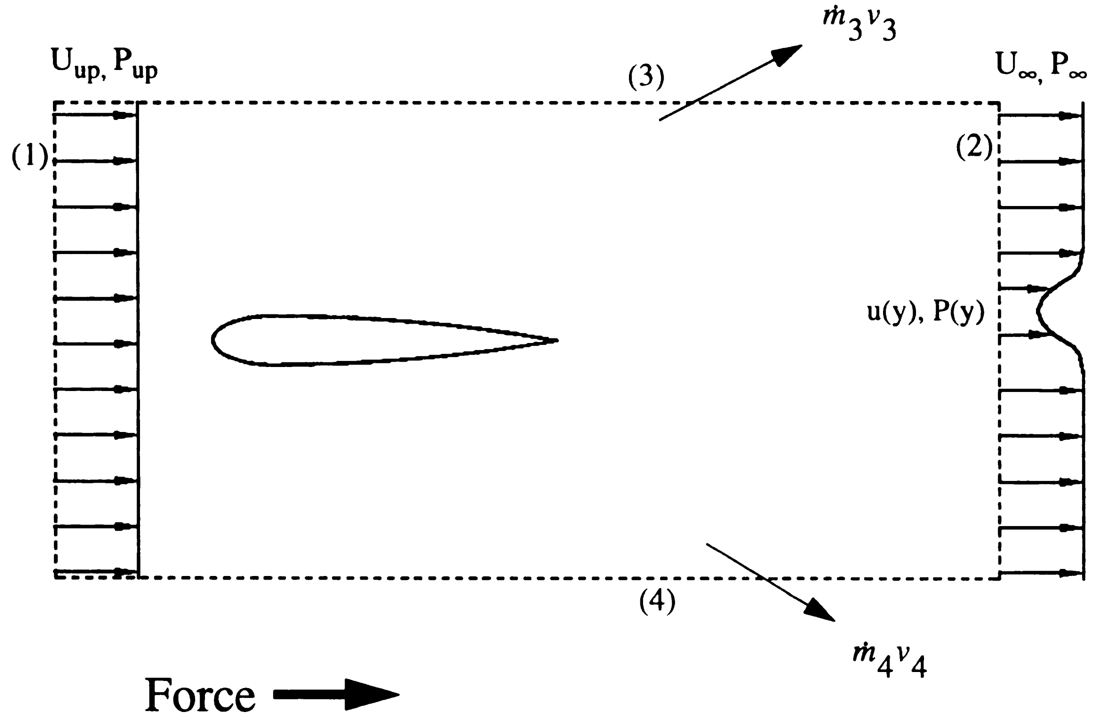

Figure 3-17: Control volume used for determination of mean drag equation

u

v

e

K

ca

st

C

Eq

wa

flu

2-D

as s

C_{F}

Whe

verti

appro

U_0 a

down

modif

used. It was recognized that P_0 and P_∞ were non-uniform vertically due to hydrostatic variations, however this variation was the same for both surfaces and therefore had no effect on the force calculation. Past researchers (e.g. Anderson et al., 1998; Koochesfahani, 1989) have used a mean streamwise velocity profile formulation to calculate the thrust/drag characteristics of this flow field. The thrust from the mean streamwise velocity, C_{FM} can be computed using:

$$C_{FM} = \frac{2}{c}\int_{-y}^{y} \frac{\bar{u}}{U_\infty}\left(1 - \frac{\bar{u}}{U_\infty}\right)dy \tag{9}$$

Equation (9) was used when only a single velocity component could be measured in the wake. This equation neglects the effects of the pressure variation in y due to the fluctuations in the flow velocity as the vortices pass the control surface. If the flow field is 2-D and the complete velocity vector is known, the mean force equation can be re-derived as shown in Appendix A to be:

$$C_{FF} = C_{FM} + \frac{2}{cU_\infty^2}\int_{-y}^{y} (\tilde{u}^2 - \tilde{v}^2)dy \tag{10}$$

Where C_{FM} is defined by equation (9). The limits of integration were, in this case, the vertical measurement extent. The mean streamwise velocity did not return to the upstream approach velocity level within the vertical measurement extent of this problem, i.e. $U_\infty \neq U_0$ at $y = 0.6c$. For this case, the pressure difference between the upstream and downstream lateral control surfaces had to be taken into account. Equation (10) was modified to reflect this as

C_{F}

Whe

P_0

The

k=5

mea

sho

(~0.

abo

freq

C_{F}

was

und

Wh

8 ra

3.2.

the

(tra

$$C_{FP} = C_{FF} + \frac{2}{cU_{\infty}^{2}} \int_{-y}^{y} \Delta P dy \qquad (11)$$

Where ΔP was found via the Bernoulli Equation by

$$P_0 - P_{\infty} = \Delta P = \frac{\rho}{2}\left(U_{\infty}^{2} - U_{0}^{2}\right) \qquad (12)$$

The upstream velocity, U_{∞}, was determined using the conservation of mass for the A=2°, k=5.7 case for which the vortices are lined up. This calculation of U_{∞} agreed with the measured free stream speed for the static airfoil case. Investigation of the velocity profiles showed that the freestream speed above and below the centerline were slightly different (~0.5%). The value of U_0 used in (12) was found by averaging the freestream speeds above and below the centerline.

Figure 3-18 shows the mean force coefficient as a function of the reduced frequency, and oscillation amplitude of the airfoil calculated from the mean profile only, C_{FM} , and the mean profile plus the RMS and pressure profiles, C_{FP}. From these data it was clear that the use of the mean profile only over estimates the thrust, and underestimates the drag on the airfoil consistent with, Streitlien and Triantafyllou (1998). When the full force equation was used the zero thrust case for A = 2° was found to be k ≈ 8 rather than, k ≈ 6 which was the case predicted by the mean field.

3.2.3 Trailing Edge Phase Averaged Data

Figure 3-19 shows flow molecular tagging flow visualization and MTV data with the airfoil passing through AOA=-2° (minimum AOA) and beginning to pitch down (trailing edge moving up). The undelayed image indicated the initial location of the tagged

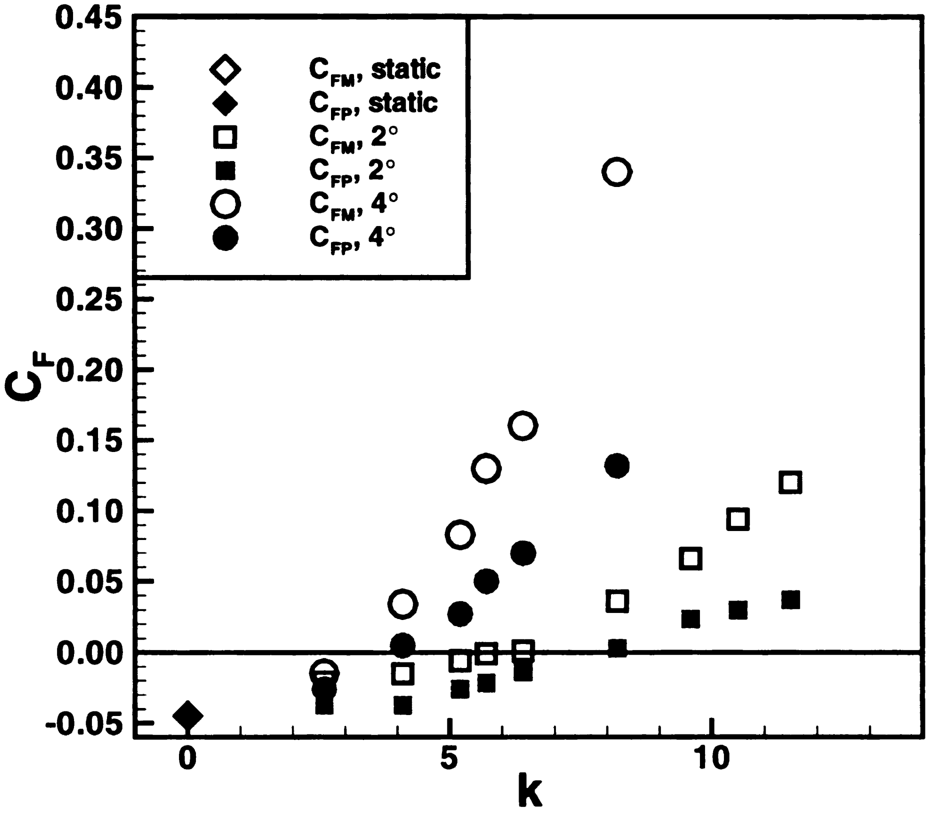

Figure 3-18: Mean force coefficient, C_F as a function of airfoil oscillation amplitude and reduced frequency.

line. The flow visualization data were taken at a reduced frequency of 8.8 (the highest flow visualization reduced frequency), and are shown in Figure 3-19 for qualitative comparison to the MTV velocity vector data taken at k = 8.6. The unsteady Kutta condition requires the flow to leave the airfoil trailing edge tangent to one of the surfaces (McCrosky, 1982). These data highlight the reverse flow along the surface of the airfoil, shown by the tagged line displacement compared to the initial line location marked by the dashed lines. Reverse flow was also indicated by the MTV velocity vector data near the airfoil surface. The reverse flow image was strikingly similar to the "possible" flow pattern drawn in Figure 5 of McCrosky (1982) and contradicts the validity of the unsteady Kutta condition for this high reduced frequency case. The reverse flow indicated that fluid

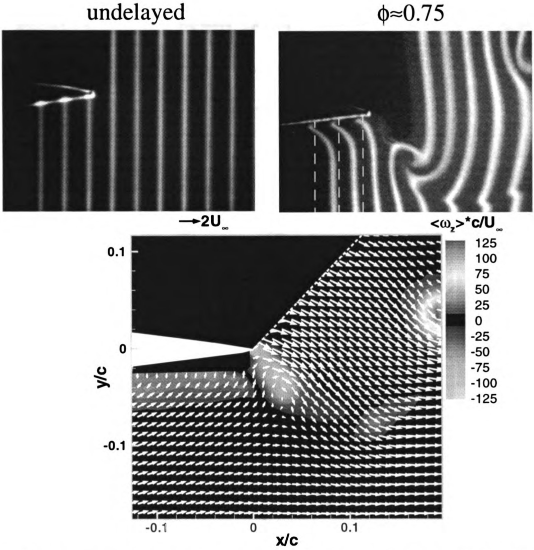

Figure 3-19: MTV flow visualization (k = 8.8) and velocity vectors from the planar MTV data (k = 8.6) near the airfoil trailing edge. Airfoil at AOA=2°, trailing edge moving up (AOA decreasing). Dashed lines indicate initial line locations.

from the top surface of the airfoil convected to the bottom of the airfoil which showed that the flow cannot leave tangent to either airfoil surface.

Flow visualization near the trailing edge is shown in Figure 3-20 for the case of AOA=0° with the airfoil beginning to pitch up (trailing edge moving down). The flow visualization images are flipped up/down in this figure to allow comparison with the MTV

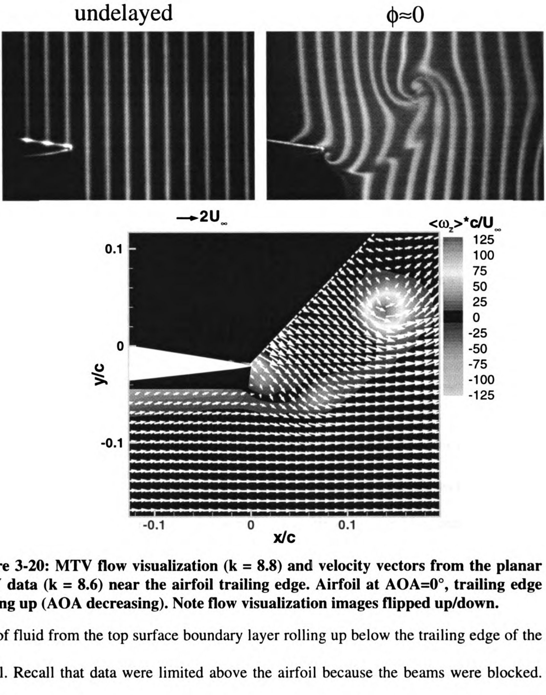

Figure 3-20: MTV flow visualization (k = 8.8) and velocity vectors from the planar MTV data (k = 8.6) near the airfoil trailing edge. Airfoil at AOA=0°, trailing edge moving up (AOA decreasing). Note flow visualization images flipped up/down.

data of fluid from the top surface boundary layer rolling up below the trailing edge of the airfoil. Recall that data were limited above the airfoil because the beams were blocked. Results in this region can be determined by assuming vertical symmetry in the flow field and moving half a cycle (phase). The delayed flow visualization image showed that the vortex formation occurred very near to, possibly upstream, of the trailing edge. The tagged line on the upper surface of the airfoil nearest to the trailing edge highlights this obs

bel

airf

to b

the

is a

trai

sho

feat

rang

fiel

3.2.

= 2

flow

k =

dow

vort

sign

vort

the

in a

observation (Figure 3-20, "delayed", third line from the left). This line was displaced below the bottom surface of the airfoil indicating that fluid from the upper surface of the airfoil was transported below the bottom surface of the airfoil and formed the vortex about to be shed. The sharp gradient marking the initial shear layer illustrated by the "kinks" in the first three tagged lines downstream of the trailing edge. MTV data for a similar phase is also shown in Figure 3-20. These data highlight the initial vortex formation near the trailing edge. The sharp gradient present in the delayed images of Figure 3-20 was not shown by the MTV data due to the data point spacing which was too coarse to capture the feature. The velocity vectors in Figures 3-19 and 3-20, which show streamwise velocities ranging from near zero to $+2U_\infty$, illustrated the large velocity fluctutations in this flow field.

3.2.4 Downstream Phase-Averaged Data

Figure 3-21 shows the phase averaged spanwise vorticity, $<\omega_z>$, for four cases, $A = 2°$, $k = 4.1, 5.2, 5.7$ and 11.5 at $\phi = 0$. The $k=4.1$ case is included in this section since the flow field characteristics were very different from the higher reduced frequency cases. For $k = 4.1$ the boundary layer left the airfoil trailing edge forming a shear layer then rolled-up downstream. The coherent vortical structures remained connected to the boundary layer vorticity until approximately 6cm (0.5c) downstream. Two distinct regions of the same sign vorticity were generated for a single cycle. The orientation of the primary regions of vorticity was suggestive of a thrusting airfoil, however, net drag was calculated based on the mean flow. This was because of the secondary regions of vorticity which were aligned in a "drag" orientation, and were strong enough to result in the mean drag.

Fi

ca

di

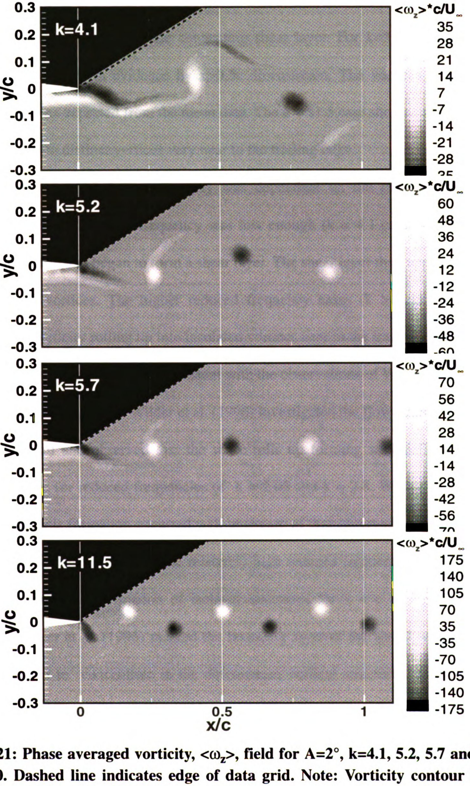

Figure 3-21: Phase averaged vorticity, $\langle\omega_z\rangle$, field for A=2°, k=4.1, 5.2, 5.7 and 11.5 cases. ϕ=0. Dashed line indicates edge of data grid. Note: Vorticity contour levels different for each case as shown.

The next highest reduced frequency, k=5.2, no longer showed the multiple structures that were in evidence for the k=4.1 case. A thin "tail" of vorticity was observed and represented the remnants of the connecting shear layer. For k=5.7 the connecting vorticity was no longer in evidence by x>0.5c downstream. The vortices were nearly aligned vertically as expected from the mean data. The k = 11.5 case showed the boundary layer rolling up into distinct vortices very near to the trailing edge.

The formation of the vortex array was dependant on the reduced frequency. Specifically, when the reduced frequency was low enough (k = 4.1 case) the boundary layers left the airfoil and began to form a shear layer. The shear layer then appeared to roll up into isolated vortices. The higher reduced frequency cases (k > 4.1) showed the boundary layer vorticity rolling up into insolated vortices near to the trailing edge.

The results of this work are consistent with the observations of Wilder et al. (1996) for lower reduced frequencies. Wilder et al. (1996) investigated the flow behind a flapping NACA0012 airfoil and observed that the wake rolls up forming well defined isolated structures at $x \approx c$ for reduced frequencies of k = 2.05 and k = 2.8. Wilder et al. (1996) commented that this formation occurred well upstream of that observed at lower reduced frequencies, and credited this with the relatively high reduced frequencies studied. The current work shows the formation of isolated structures for $x < c$ at higher reduced frequencies. Wilder et al. (1996) marked the boundary layer of the airfoil with dye. The dye was observed to concentrate in the downstream vortical structures. They inferred, from the lack of dye between the marked vortices, that there was little vorticity between the isolated vortical structures. The current whole field measurements confirm quantitatively that inference.

F
C
fu
pr

in

goo

sm

Representative vorticity profiles are plotted in Figure3-22 for A = 2°, k = 5.2, 11.5 along with the best fit to a Gaussian vortex profile. The vortex profile showed an excellent fit to the Gaussian model for |d| < 0.5 cm (nominally the core size). For |d| > 0.5 cm the vortex deviated from the Gaussian profile with slightly higher measured vorticity levels. There was near symmetry shown in the vorticity profile for k=11.5 while the k=5.2 case was asymmetric. Specifically, the vertical (y-direction) profile was thinner and showed a second peak at r ≈ 1.5 caused by the remnants of the connecting vortex sheet.

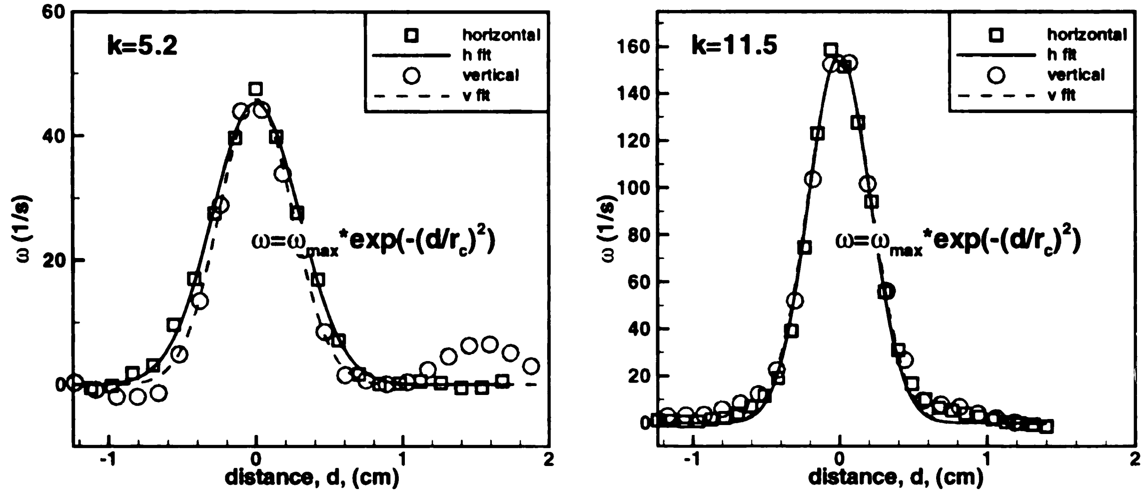

Figure 3-22: Vorticity profiles for 2 degree, k=5.2, 11.5 case at x = 6 cm, z = 0 cm. Curve is best fit to a Gaussian vortex profile. Horizontal profiles show quantity as a function of x, and vertical profiles a function of y. Equation represents the vorticity profile for a Gaussian vortex.

Figure 3-23 shows the azimuthal velocity, V_θ, profile for the same vortices shown in Figure 3-22. The velocity profiles were also fit for a Gaussian vortex. Agreement was good for the k = 5.2 case over the entire range, while the k = 11.5 case agreed only over a small range near the vortex center. This was consistent with the agreement of the vorticity

Fig
cm.
ind

pro

oth

trac

circ

vor

defi

cen

vor

use

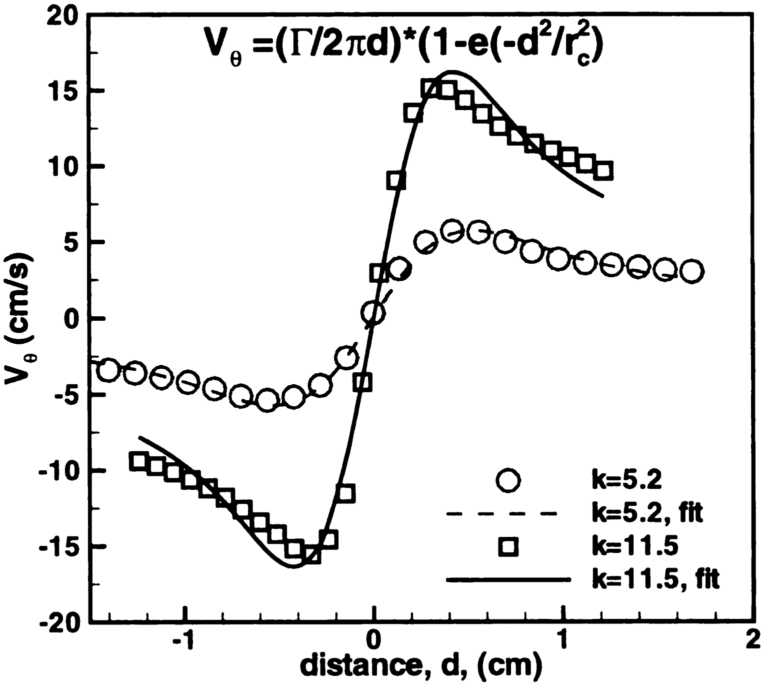

Figure 3-23: Azimuthal velocity profile for the 2 degree, k=11.0 case at x=6 cm, z=0 cm. Fits shown for portions of the profile indicated by the line sections. Functionality indicated by equation near the fit line.

profile fits already discussed. These velocity profiles were similar to those reported in other works (see e.g., Wilder et al. (1995), Koochesfahani (1992)).

The downstream development of the vortical flow field can be illustrated by tracking the motion of the vortex and characterizing the peak spanwise vorticity, $<\omega>_{peak}$, circulation, Γ, and core radius, r_c, as a function of downstream distance. The location of a vortex was defined as the location of the centroid of the vorticity. The centroid was used to define the vortex location as the vortex becomes non-Gaussian downstream and the centroid better represents the vortex location (compared to the location of the peak vorticity) for these distributions. To find the peak vorticity a second order polynomial was used for the fitting the data and the spatial extent of the fit was limited to $0.5r_c$ away from the nominal peak. This process was repeated for each phase and was carried out until the vortex left the measurement field.

The circulation of the vortex is determined by

$$\Gamma = \sum \langle \omega_z \rangle \Delta x \Delta y \tag{13}$$

Where Δx and Δy were the data grid spacing. When using (13) only the vorticity from the vortex should be included while noise in the vorticity calculation should not. To achieve this two threshold levels are used, a vorticity cut-off limit and an included spatial radius. A cut-off limit of 2 s^{-1} was placed on the vorticity to reduce the effects of experimental noise on the circulation calculation. Only the vorticity with in spatial radius of 1 cm from the peak vorticity location was used. The 1 cm radius was justified by the vorticity profiles in Figure 3-22 because it was small enough to not include the "tail" of the vortex for the k = 5.2 case (making a localized measure), but big enough to be within 1% of the infinity value for the k = 11.5 case. A conservative estimate of the uncertainty level in the circulation calculation is 2 cm^2/s based upon the effects of threshold level and radius of included data.

The vortex core radius, r_c, can be defined by the e^{-1} point of the vorticity field for a Gaussian shaped vortex. The vortex initially fit a Gaussian profile as shown in Figure 3-21, however, the vorticity distribution becomes non-Gaussian downstream. To account for this, the "radius of gyration" of the vorticity field was used to define the vortex core radius. The radius of gyration is defined as the square root of the second polar moment of inertial of the vorticity divided by the circulation, or:

c

n

o

de

de

usi

can

$\frac{D(}{D}$

If the

$$r_c = \sqrt{\frac{\iint r^2 \omega dA}{\iint \omega dA}} \qquad (14)$$

The core radius, r_c, defined by equation (14) reduces to the e^{-1} point value for a Gaussian vorticity profile.

Figure 3-24 shows the development of the vortex properties as a function of the downstream distance for A = 2°, k = 4.1, 5.2 and 11.5. Only the positive sign vortex properties are shown in Figure 3-24 since vortex property data at x = 6cm (Figure 3-29, discussion to follow) showed the vortex properties for the positive and negative sign vortices agree well. Recall that the k = 4.1 case had multiple regions of same sign vorticity for each phase. For that case the vortex with the strongest vorticity was tracked. The maximum of the vorticity was initially constant for the k = 5.2 and 11.5 cases. This constant region reached nominally to x=0.4c downstream. After this point there was a decrease in the local maximum vorticity as a function of x. The k = 4.1 case showed a nominally uniform peak vorticity until $x \approx 0.75c$. The expected decrease in vorticity based on diffusion of vorticity is shown for the k = 11.5 case by a dashed line in Figure 3-24. The decrease in vorticity was larger than expected if diffusion alone acted on the vortex to decrease the vorticity magnitude, so a second mechanism must be investigated.

Vortex stretching / re-orientation was also investigated to describe the difference using arguments similar to those found in Cohn (1999). The vorticity transport equation can be written as

$$\frac{D\langle\omega_z\rangle}{Dt} = \left(\langle\omega_x\rangle\frac{\partial w}{\partial x} + \langle\omega_y\rangle\frac{\partial w}{\partial y} + \langle\omega_z\rangle\frac{\partial w}{\partial z}\right) + \upsilon\nabla^2\omega_z \qquad (15)$$

If the convection speed is constant, and ω_x, ω_y are small then equation (15) simplifies to:

Figu

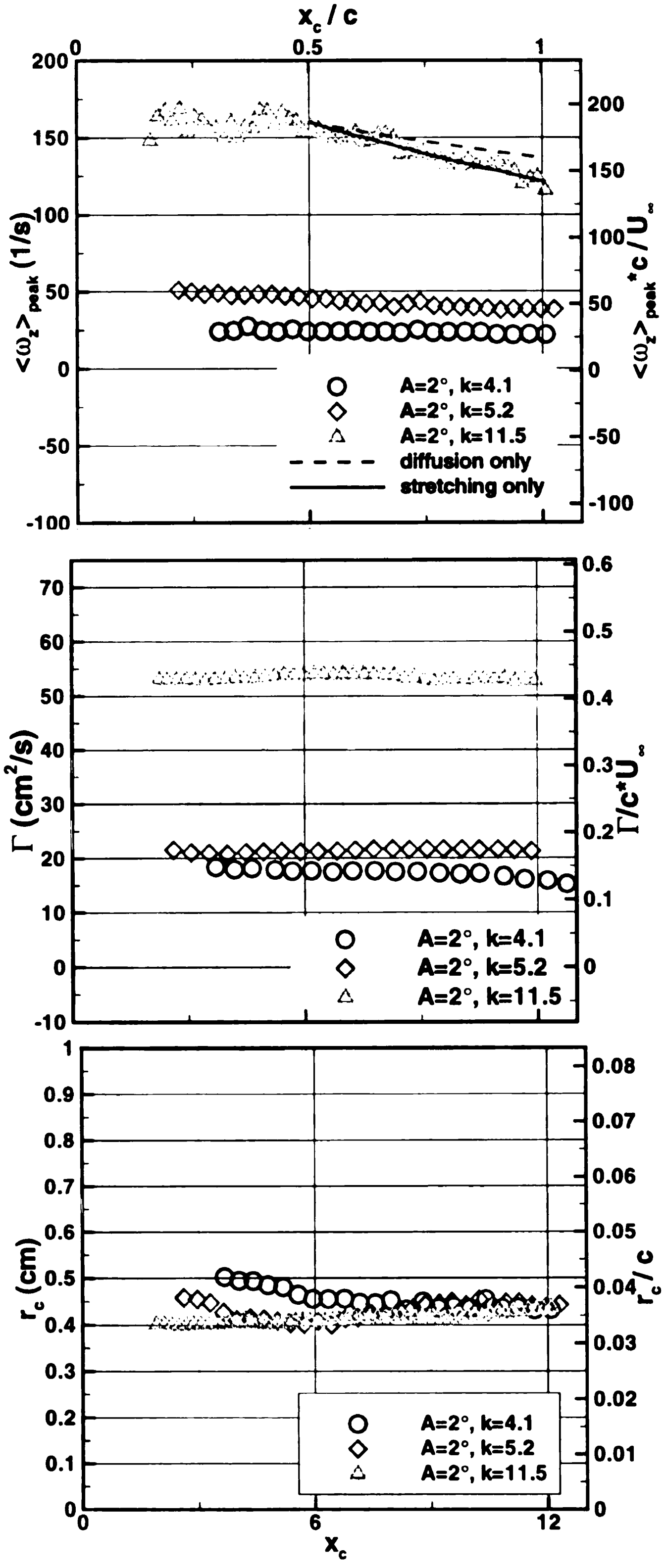

Figure 3-24: Vortex array properties as a function of the streamwise distance.

$$\frac{\partial}{\partial x}\langle\omega_z\rangle = \frac{1}{U_c}\left(\underbrace{\langle\omega_z\rangle\frac{\partial w}{\partial z}}_{\text{I}} + \underbrace{\upsilon\left(\frac{\partial^2}{\partial r^2}\langle\omega_z\rangle + \frac{1}{r}\frac{\partial}{\partial r}\langle\omega_z\rangle\right)}_{\text{II}}\right) \qquad (16)$$

Using equation (16) with a constant axial flow gradient ($\frac{\partial w}{\partial z}$) (term I) and viscosity (term II) neglected allows qualitative investigation of the effects of stretching on the vortex. The solid line in Figure 3-24 is the result of applying term I of equation (16) (term II is the viscous diffusion term) with a constant axial flow gradient, found by best matching the stretching term to the data, of -0.6 s^{-1}. The existence of this axial flow gradient was attributed to the development of the axial flow generated by the vortex interaction with the side walls of the tunnel. This axial flow gradient was below the current measurable axial flow gradient of 1 s^{-1}. From this analysis though, the decrease in peak vorticity appears to be a function of both viscous diffusion, and vortex stretching.

The circulation as a function of the streamwise distance is also shown in Figure 3-24. The data in Figure 3-24 show that the circulation was constant, to within the uncertainty limit, over the spatial extent investigated. The small oscillations observed for the k = 11.5 case are due to vorticity moving in (as the vortex forms) and out (as the vortex expands) of the included range.

The vortex core radius, r_c, is shown in Figure 3-24. The vortex formation dynamics were further illustrated by these data. All three cases have nearly the same core radius, r_c=0.43 cm, at x = c downstream. The k = 11.5 case showed a linear increase in r_c from 0.4 cm to 0.43 cm over the extent investigated. The k = 5.2 case showed the same linear increase in r_c for x > 0.5c. For x < 0.5c the core radius decreased from a high level of 0.55 cm near the trailing edge to a minimum of $r_c = 0.40$ cm at $x \approx 0.5r_c$. The k = 4.1 case showed the same trends as the k = 5.2 case, however the linear growth range began at $x \approx 0.7c$. The decreasing core radius shown initially for the k = 4.1 and 5.2 cases can be explained by the formation process. The lower reduced frequency cases formed into isolated structures further down stream as was shown in Figure 3-15. The vorticity was more distributed, therefore r_c was larger, while the isolated structures were forming.

The vortex spacing, and orientation are also important parameters in the description of the dynamics of this flow field. A schematic of the vortex spacing nomenclature is shown in Figure 3-25. The sign of b is defined as the lateral distance from

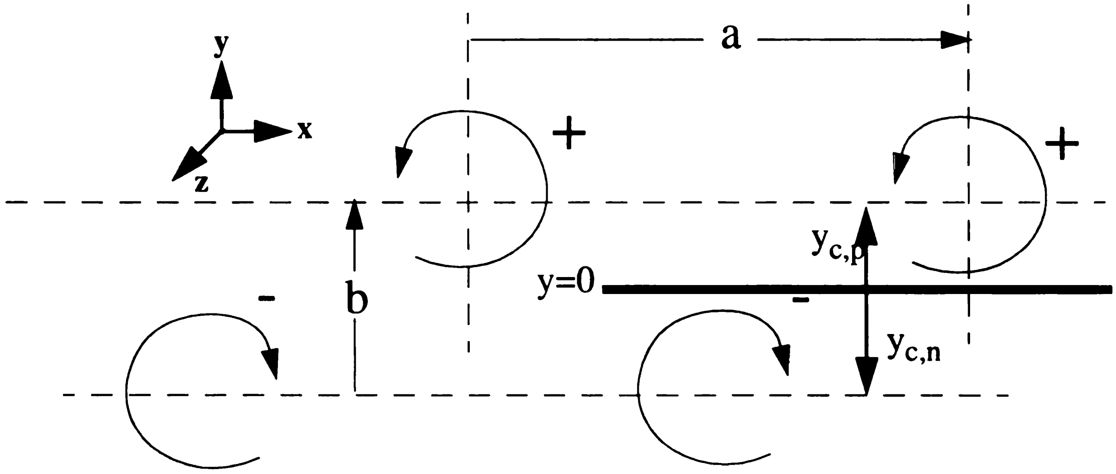

Figure 3-25: Schematic representation of vortex spacing variables. Positive b indicates positive vorticity is above negative vorticity as shown.

the negative vortex to the positive vortex, where the vortex location was again the location of the centroid of the vorticity. The vertical was significant in this flow field because it was known from the mean flow data that the orientation of the vortex array, and

i

n

do

aw

for

con

dow

dow

incre

corresponding net force, switched as the reduced frequency increased. The streamwise spacing, a, is a measure of the vortex sheet wavelength (and frequency).

The vortex spacing as a function of downstream distance is shown in Figures 3-26 and 3-27. Figure 3-26 shows the vertical spacing between the positive and negative vorticity for $k = 5.2$ and 11.5 cases. The vertical spacing, b, was calculated by determining the vertical locations of the centroid of the vorticity at a given downstream location for the negative and positive sign vortices; therefore, this measure is not an instantaneous measurement. Both cases showed an initial motion of the vortex away from the $y=0$ line. After that initial region, the vortices moved back towards the center. The $k = 5.2$ case appeared to be approaching a constant vertical spacing distance for $x > c$. The high reduced frequency case, $k = 11.5$, showed that for $x > 0.5c$ the distance between the vortices remains relatively constant, though they were moving away from the $y = 0$ line in the +y-direction.

The vortex streamwise spacing, a, is shown in Figure 3-27. The cases showed an initial period of increasing a. This was explained by observing that the vortices formed near to the trailing edge in a nearly fixed location, then convected downstream. The downstream vortex of the same sign was already in the flow field and therefore convecting away from the forming vortex causing the initial increase in a. Once the vortex was formed and started to convect downstream the streamwise spacing remained relatively constant. The $k=5.2$ case showed decreasing streamwise distance, a, indicating the downstream vortex was slowing slightly. The streamwise distance, a, increased with downstream distance for the $k=11.5$ case indicating the convection velocity was increasing. The vortex convection speed, U_c, as a function of downstream distance is

Figur

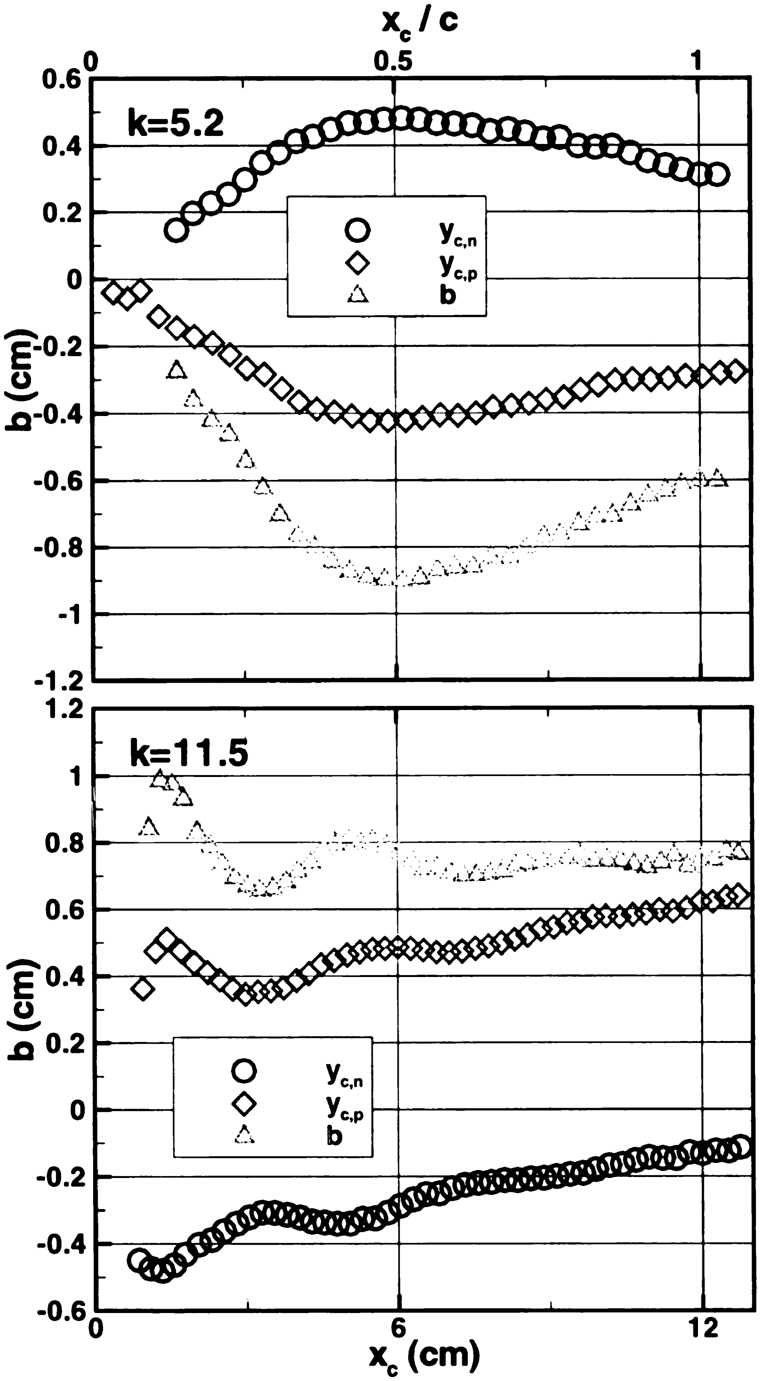

Figure 3-26: Vertical vortex spacing, b, as a function of downstream distance.

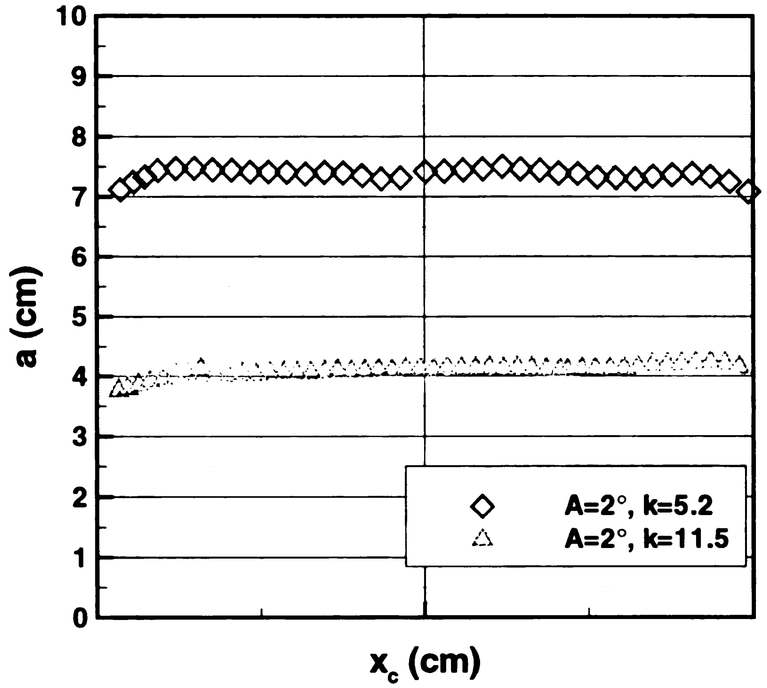

Figure 3-27: Vortex streamwise spacing, a as a function of downstream distance.

shown in Figure 3-28. These data were found by numerically differentiating the vortex position versus the airfoil phase and multiplying by the frequency. The differentiation (i.e., convection speed) was very sensitive to uncertainty in the spatial location, so the spatial location data were first smoothed using a moving window averaging scheme, then differentiated. The initial acceleration period of the vortex was clearly observed for the k=5.2 and 11.5 cases. .The k = 11.5 case showed a trend of nominally linear increase in U_C as a function of increasing downstream distance. There was a brief, U_C = constant period for $0.67c < x < 0.75c$, which was followed by a return to the linearly increasing convection speed. The k = 5.2 case showed a nominally uniform convection speed after the initial acceleration, then a small decrease in the convection speed for x > 9 cm (0.75c).

The vortex properties as a function of the reduced frequency of the airfoil are presented in Figure 3-29 for x = 6 cm (0.5c). The vortex properties for the both positive

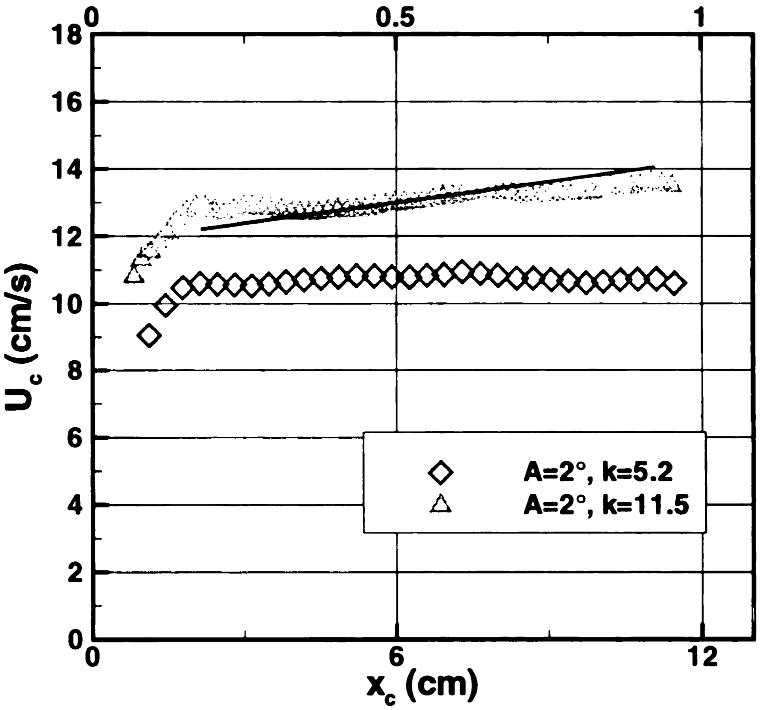

Figure 3-28: Vortex convection speed, U_c, as a function of downstream distance.

and negative sign vortices are shown in Figure 3-29. These data indicated the vortices differ by sign of vorticity (and circulation), but otherwise similar. Note that the cutting walls placed into the flow to initiate the vortex/no-slip interaction were placed so that the leading edge was at x = 6cm (0.5c). This discussion, therefore, serves as an indication of the initial conditions for the vortex array before interaction with the wall.

The peak vorticity, $<\omega_z>_{peak}$, and circulation, Γ, increased with increasing reduced frequency as expected. The peak vorticity magnitude increased linearly by over 6 times for the reduced frequency range investigated. The circulation showed a smaller increase of 3 times. The circulation data were fit to a second order polynomial. No curve was drawn for the 4° due to the limited number of data points.

The vortex core radius was $r_c \approx 0.4$ cm for the 2° (k > 5) case and $r_c \approx 0.46$ cm for the 4° cases. The core radius initially decreased as a function of k for the 2° case. The

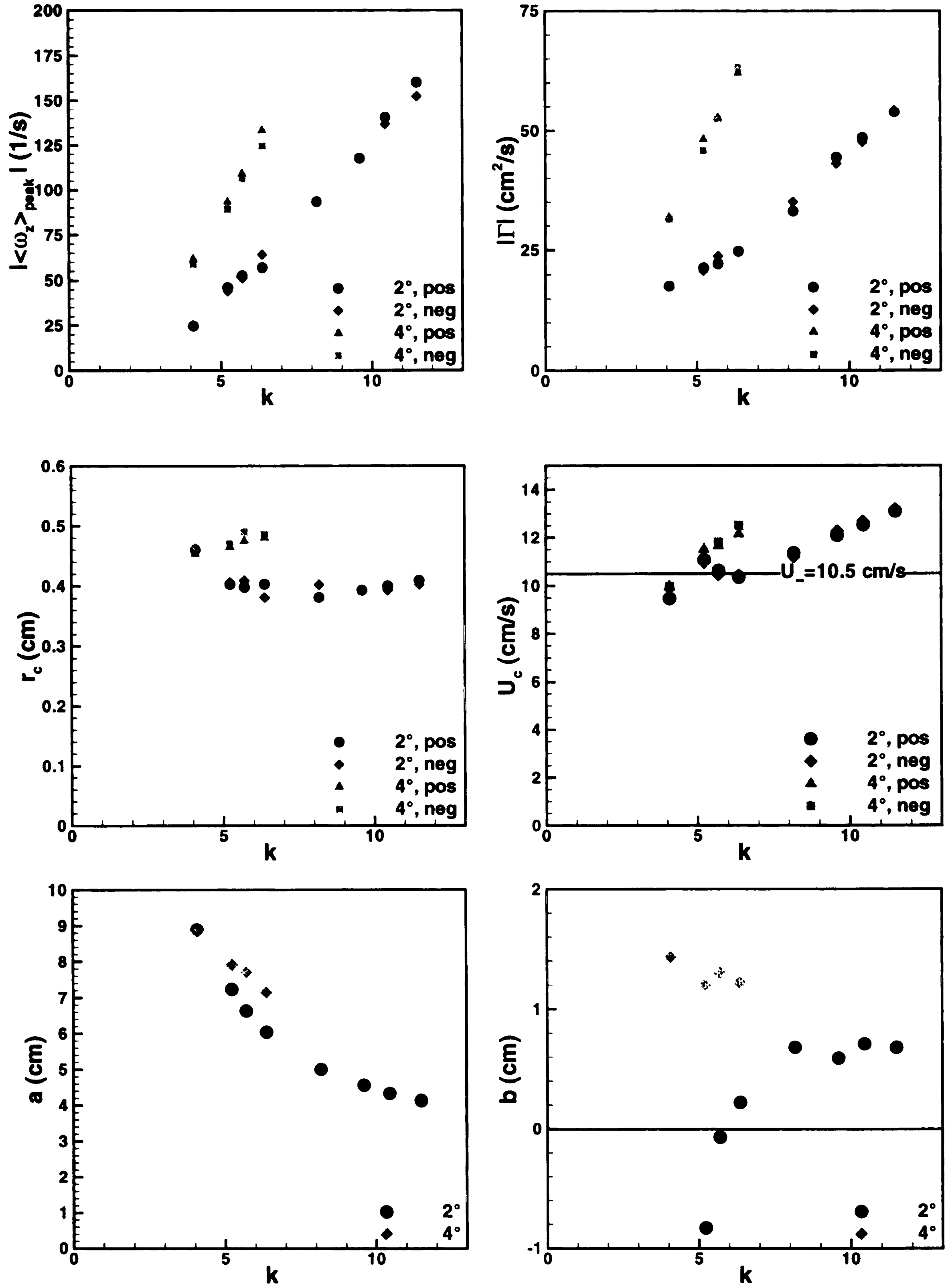

Figure 3-29: Peak vorticity ω_{peak}, circulation Γ, core radius r_c, convection speed U_c, and spacing (a,b) for the 2-D planar measurements at x= 6 cm, z = 10 cm.

reduction of the core radius at x = 6 cm for A = 2° was consistent with difference in the formation process of the vortices for this oscillation amplitude. Specifically, for low k's, isolated and concentrated vortices form farther downstream which resulted in a more diffuse spatial distribution of vorticity and greater r_c. The A = 2° r_c data do indicate a slight increase in the vortex core size for the higher reduced frequencies. This may be due to three dimensionalities (i.e., axial core flow) from the vortex / side wall interactions beginning to affect to vortex array. The 4° case showed higher values for the core radius, $r_c \approx 0.47$ cm. The lower r_c value for A = 4°, k = 4.1 was due to the formation of multiple (2 rather than 1) isolated vortices of the same sign for each phase which result in smaller vortices. The quoted r_c value was for the strongest vortex of each sign.

A comparison of the vortex core radius can be made between the radius of gyration measure (16) described above and the fit to a Gaussian profile. The core radius for the vortex profile of k=11.5 case shown in Figure 3-21 was found to be 0.31 via fit parameters. The reason the fit underestimated the vortex core size was due to the deviation from the Gaussian profile for $|d| > 0.5$. The actual vorticity was higher than the fit vorticity for $|d| > 0.5$ which resulted in a larger core radius using (16). The same comparison for the k=5.2 case shows good agreement with the vortex core radius from the Gaussian fit (from the horizontal profile with no tail) being equal to $r_c = 0.41$, compared to 0.40 from (16).

Vortex convection speed (U_c) and spacing data are provided in Figure 3-29. The vortex convection speed at this fixed spatial location was found via best linear fit to the position of the vortex core as a function of phase for the 20 points around the x = 6cm location. Phase was converted to time using the airfoil oscillation frequency, *f*. The vortex convection speed, U_c, was larger, by up to 35%, than the freestream speed, U_∞. The low freq

drag

$<\omega_p$

vort

spac

was

oscil

spac

The

velo

velo

V_{sw}

wher

V_{sw}

and i

found

Profil

throu

the p

frequency k = 4.1 cases show U_c less than U_∞. For the 2°, k = 5.2, 5.7, 6.4, the near zero drag cases, $U_c \approx U_\infty$.

The streamwise spacing, a, and the lateral spacing, b, between $<\omega_{peak,p}>$ and $<\omega_{peak,n}>$ were found directly from the spatial location for each vortex when the negative vortex was located at 6cm downstream of the trailing edge of the airfoil. The streamwise spacing, a, of the vortex cores decreased with increasing reduced frequency. This result was expected since the vortex spacing, or wavelength, was dependent upon the airfoil oscillation frequency. Increasing f reduced the wavelength (and therefore streamwise spacing). The lateral spacing showed a switch in the orientation for the A = 2°, k > 5.7. The vortex pattern was nearly aligned for the A = 2°, k = 5.7 case consistent with the mean velocity profile shown in Figure 3-6.

The peak azimuthal or swirl velocity, V_{sw}, is shown in Figure 3-30. The swirl velocity was calculated via the following formula:

$$V_{sw} = \frac{\Gamma}{2\pi r_c}\left(1 - e^{-r/r_c}\right) \qquad (17)$$

where V_{sw} occurs at $r = 1.12r_c$. Substituting the value for r into (17) yields:

$$V_{sw} = \frac{0.6382\Gamma}{2\pi r_c} \qquad (18)$$

and is shown in Figure 3-30 by the symbols with solid lines. The swirl velocity was also found, for comparison, from the measured velocities when the vortices were at x = 6cm. Profiles of the velocity were taken along the streamwise, v(x), and lateral, u(y), directions through the vortex core. The swirl velocity was taken to be the peak azimuthal velocity in the profile. The vortices were slightly asymmetric due the induced velocity of the

Figu
x=c/

neig
diffe
close
used
the d
steep
was s
reduc

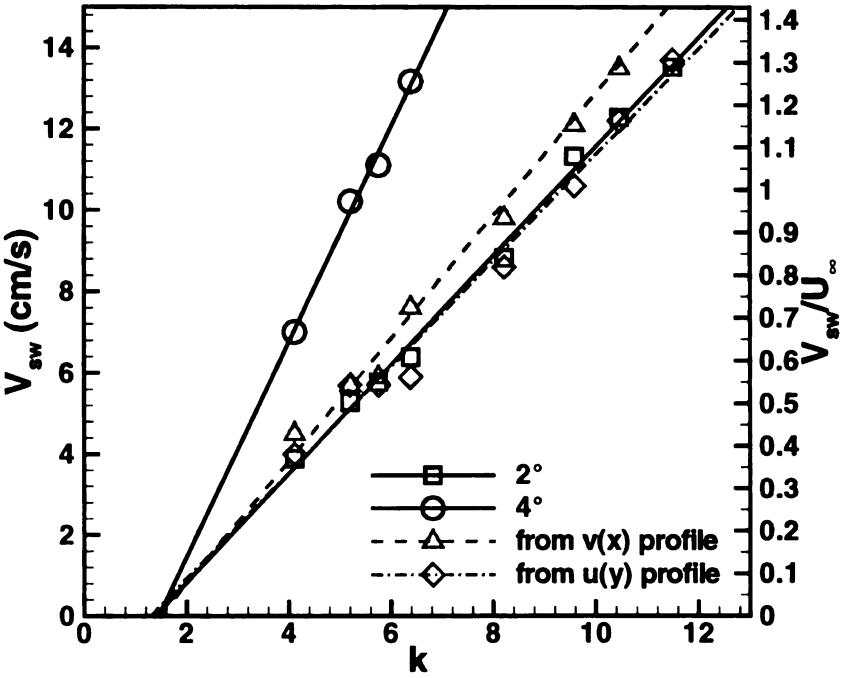

Figure 3-30: Maximum swirl velocity, V_{sw}, as a function of the reduced frequency at x=c/2, midspan.

neighboring vortices which caused the V_{sw} from the streamwise profile to be higher. The difference increased with increasing k. The was because the vortices were stronger and closer together increasing the induced velocity affect. The calculated swirl velocity was used for reference in this work given the good agreement with the measured values and the difficulty of obtaining velocity profiles through the center of the vortex because of the steep nature of the velocity profile. The swirl velocity showed the peak rotational velocity was significant for this study, exceeding the freestream and convection speeds for high reduced frequencies.

3.

pro

rac

3.2.5 Vortex/Cutting Wall Initial Conditions

The initial conditions for the axial flow study were taken from the vortex properties at x = 6cm. The results are summarized in Table 1. The initial vortex core radius, r_{ci} = 0.40 cm was used for the 2° cases, and r_{ci} = 0.47 for the A = 4° cases.

Table 1: Vortex Properties at x=6cm downstream of Airfoil Trailing Edge

A	k	ω_i (s^{-1})	Γ_i (cm^2/s)	V_{swi} (cm/s)
2°	**4.1**	**25**	**17.6**	**3.9**
2°	**5.2**	**45**	**21.1**	**5.3**
2°	**5.7**	**52**	**23.0**	**5.8**
2°	**6.4**	**61**	**24.6**	**6.4**
2°	**8.2**	**94**	**34.1**	**8.8**
2°	**9.6**	**118**	**43.7**	**11.3**
2°	**10.5**	**139**	**48.0**	**12.3**
2°	**11.5**	**156**	**54.1**	**13.5**
4°	**4.1**	**60**	**31.6**	**7.0**
4°	**5.2**	**91**	**46.9**	**10.2**
4°	**5.7**	**108**	**52.8**	**11.1**
4°	**6.4**	**129**	**62.7**	**13.2**

CHAPTER 4

VORTEX / SIDE-WALL INTERACTION

4.1 Vortex / End Wall Interaction

Axial flow develops within the vortex cores because of the interaction of the vortices with the side walls of the facility (Figure 4-1). Measurements of the axial flow due to this interaction provided a comparison for the cutting wall interaction measurements, which had different boundary conditions. Additionally, these results allowed the choice of placement of the cutting walls to minimize the effects of the vortex / side wall interaction. Single line tagging, as described in Section 2.4, was used to provide a measurement of the transverse velocity for this experiment. Images of a single tagged line were acquired at a spanwise location of z = 10 cm off of the centerline, nominally halfway between the tunnel centerspan and the airfoil assembly side walls, over a streamwise extent of $13 \leq x/r_{ci} \leq 113$ (5-45 cm). Note that the discussion now shifts to the

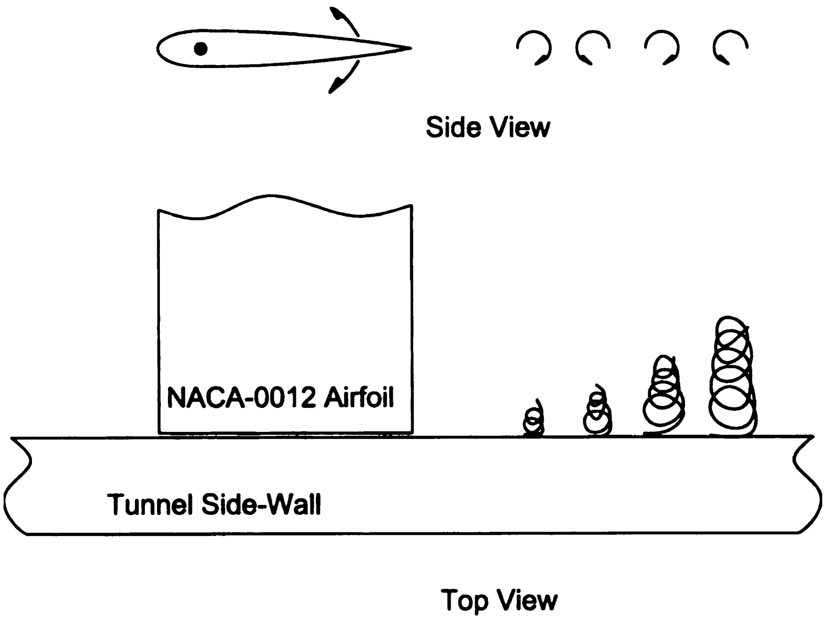

Figure 4-1: Schematic of the vortex / side wall interaction.

vort
and

freq
opti
expe
flow
tunn

the
case
prof
dist
was
by t
ima
wall

the
cont
vort
spat
axis

vortex axial flow development. The normalization variables switch from airfoil based (c and U_{∞}) to vortex based (r_{ci} and V_{swi}).

Flow conditioners were placed at the end of the tunnel test section to dampen low frequency oscillations in the tunnel freestream speed. These flow conditioners blocked optical view from the end of the tunnel and were removed, for the line tagging experiments only, to provide access for imaging during the line tagging experiments. The flow facility motor setting was adjusted to account for the nominally 30% increase in the tunnel freestream speed without these flow conditioners.

Figure 4-2 shows several representative images, at x=15 cm ($38r_{ci}$) downstream of the trailing edge and span location 10 cm from the center span, for the A = 2°, k= 11.5 case. These images show clear evidence of axial flow within the vortex core. Velocity profiles that are "Gaussian" were observed along with velocity profiles that were distinctly non-Gaussian, with multiple peaks. The line displacement method utilized here was a single component measurement technique and these data were therefore influenced by the strong lateral (v) velocity with some of the profile shapes due to that fact. These images also indicated that there was weak flow directed towards rather than away from the wall (i.e. "reverse" spanwise flow) present.

Figure 4-3 serves to orient the reader to the progression of the axial flow profile as the vortex convects past the measurement (i.e., laser line) location. White lines in the contour plot of Figure 4-3 represent the laser line (or line tag position) relative to the vortex position. It is important to remember that in Figure 4-3 the tagged line was fixed spatially and the vortex convected past which is represented in the figure by time on the x-axis. As the vortex entered the measurement region, Figure 4-3(a), the axial flow was low.

Fi
inc

In t

flov

reac

(Fig

axial

Typi

vorte

becan

revers

Figure

spatial

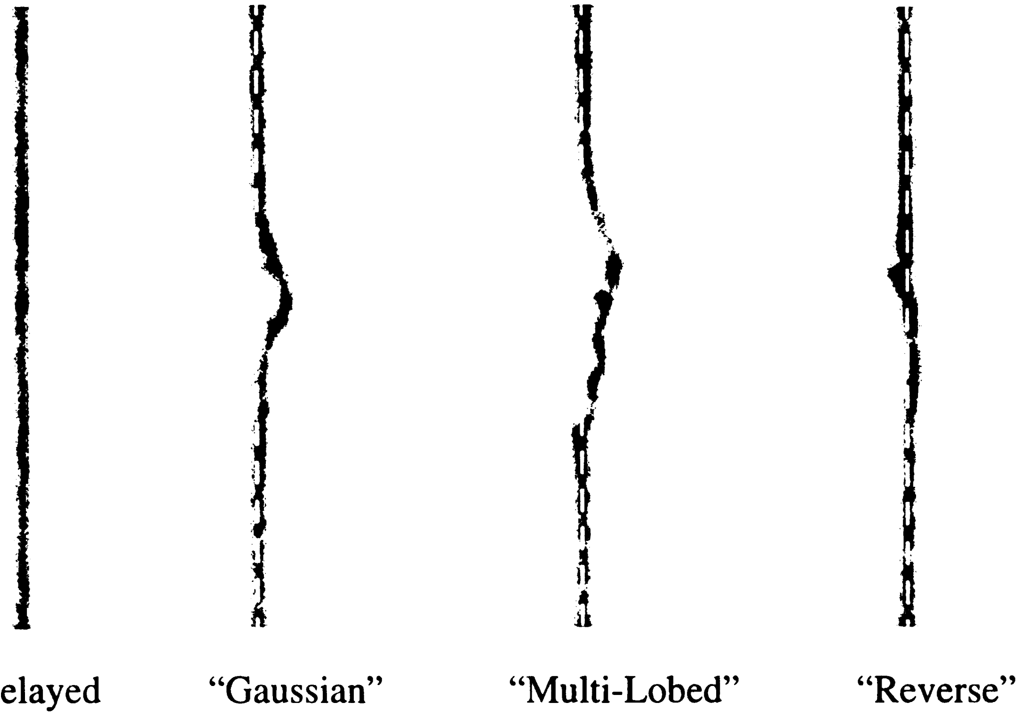

Figure 4-2: Sample line tagging imaged. A=2° k=11.5 x=38r_{ci}. Dashed white lines indicate undisplaced line center location for reference.

In this portion of the airfoil phase the reverse profiles in Figure 4-2 were found. The axial flow speed increased, Figure 4-3(b),(c), in magnitude until the center of the vortex was reached, Figure 4-3(d), when the peak axial flow was measured. The “Gaussian” profiles (Figure 4-2) were most typically found in the (d) portion (Figure 4-3) of the phase The axial flow level decreased as the vortex left the measurement location, Figures 4-3 (e)-(g). Typically the “multi-lobed” profiles in Figure 4-2 were found near the outer portion of the vortex cores (b)-(c) and (e)-(f) (Figure 4-3) though farther downstream the profiles became less Gaussian and more irregular for all phases. Figure 4-3 (f),(g) showed a reverse axial flow over a portion of the core. The spatial extent of the displaced fluid in Figure 4-2 was similar in size to the vortex core size in Figure 4-3 indicating that the spatial region of the spanwise flow was similar to the spatial extent for the vortex array.

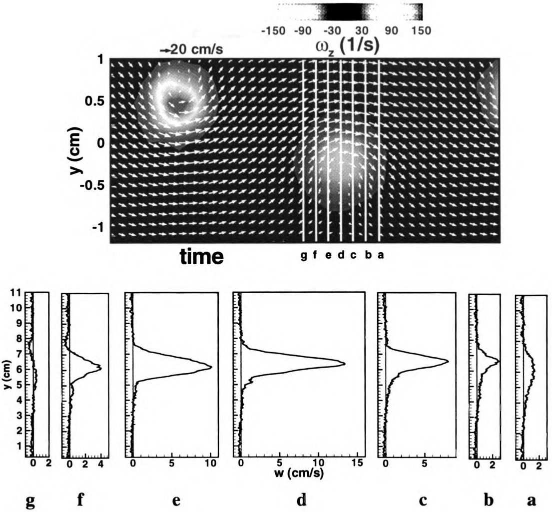

Figure 4-3: Schematic representation of axial flow profiles relative to vortex location. A=2°, k=11.5, x=38r_{ci}.

The relationship, spatially and temporally, of the axial flow to the vortex core can only be surmised using these data. Stereoscopic data in Chapter 5 will show that the reverse flow actually occurred outside of the vortex cores not within them and the strong spanwise flow away from the wall did occur within the vortex core.

The line tagging data were processed to provide the axial velocity profiles versus y. The peak axial flow level, both positive and negative, for each measurement location were recorded and plotted. Figure 4-4 shows $<w_{peak}>$ versus the downstream distance and

Figu
dow

the r

the r

meas

dime

dimer

nomir

and ap

that th

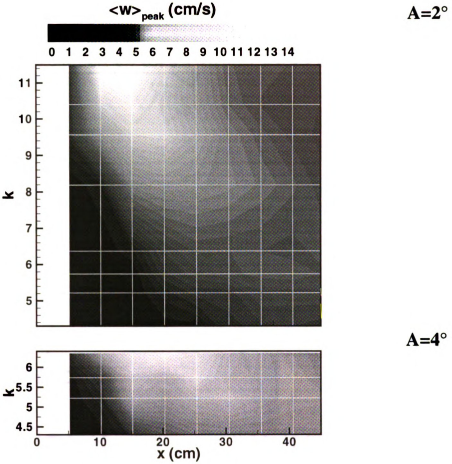

Figure 4-4: Local phase averaged peak spanwise flow, $\langle w \rangle_{peak}$, versus the downstream distance, x, and the reduced frequency, k. Data plotted dimensionally.

the reduced frequency plotted dimensionally. The grid shown on the contour map marks the measurement locations. The axial flow within the vortex core reached the z = 10cm measurement plane close to the trailing edge (i.e. for $x \approx 13r_{ci}$), for $k > 9.6$. The dimensional values show $\langle w \rangle_{peak} < 2$ cm/s at this location. The same data are shown non-dimensionalized by the vortex initial conditions in Figure 4-5. Axial flow levels were nominally equal to the swirl velocity for the highest reduced frequency (A = 2°, k = 11.5) and approached the swirl velocity for all other cases. The data in Figure 4-4 and 4-5 show that the peak axial core flow first increases, then decreases in magnitude. There were

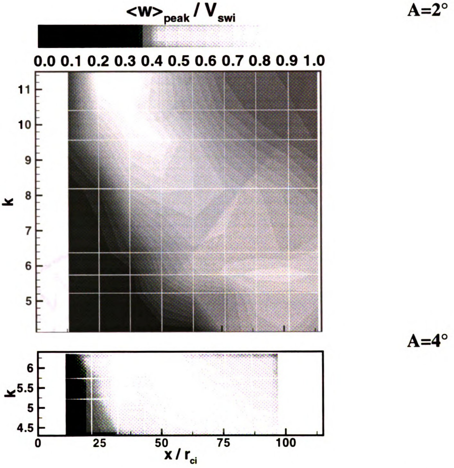

Figure 4-5: Local peak spanwise flow, $<w>_{peak}$, versus the downstream distance, x, and the reduced frequency, k. Data plotted non-dimensionally.

indications from the k = 11.5 case that $<w>_{peak}$ may approach a constant value or be slowly decreasing far downstream. An alternate spatial normalization, the vortex wavelength “a”, was tried and the results are plotted in Figure 4-6. The result of this spatial normalization was to make the downstream location of maximum spanwise flow occur nearer to the same location (between 2.5 and 4) indicating that the wavelength may be an important spatial length in this problem.

Figure 4-7 shows the peak spanwise velocity versus the x location for selected reduced frequencies. These data showed that if the reduced frequency is high enough (k >

Fi
ar

6.

Af

in

do

fre

mea

data

freq

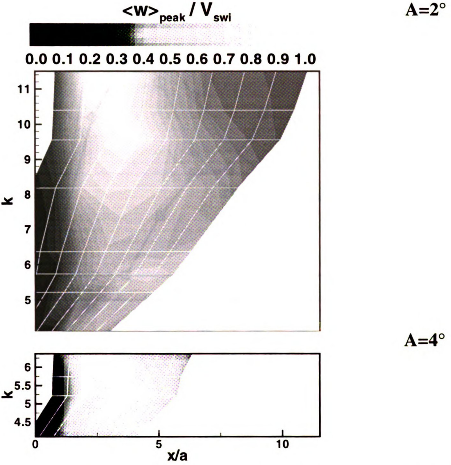

Figure 4-6: Local peak spanwise flow, <w>$_{peak}$, versus the downstream distance, x, and the reduced frequency, k. Distance normalized by vortex array wavelength, a.

6.7) the peak axial velocity level rapidly increased as a function of downstream distance. After the maximum was reached <w>$_{peak}$ first decreased with a high deceleration, similar in magnitude to the initial acceleration, followed by a slower deceleration. The downstream location of the maximum axial flow decreased with increasing reduced frequency. For k ≤ 6.7 the peak axial flow velocity did not decrease within the measurement extent, but remained nominally constant. The reverse axial flow, <w$_{rev}$>, data show that reverse flow had levels less than 0.1<w$_{peak}$> for the highest reduced frequency tested (Figure 4-8).

Fig
z=1

Fi
A=

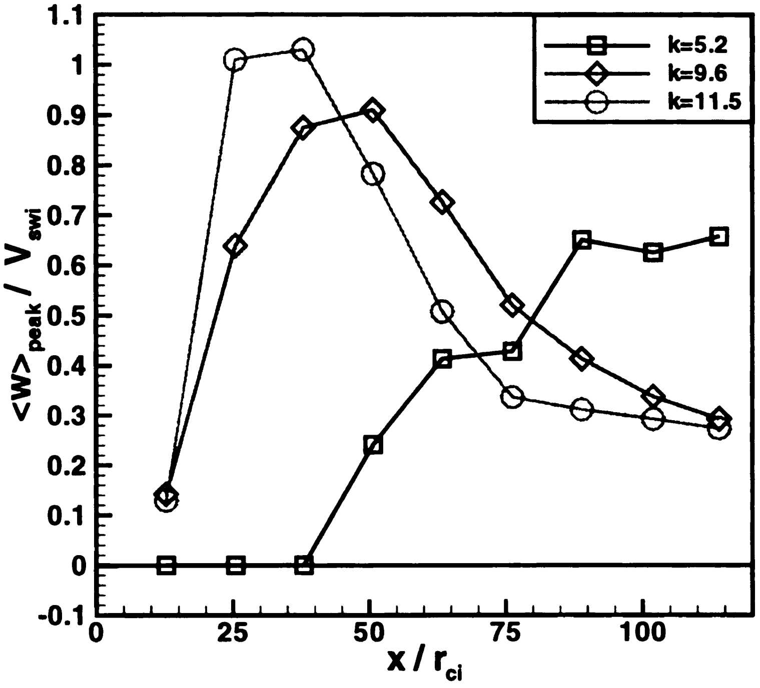

Figure 4-7: Peak axial flow speed, $<w>_{peak}$, versus the reduced frequency for A=2° at z=10cm off the centerspan.

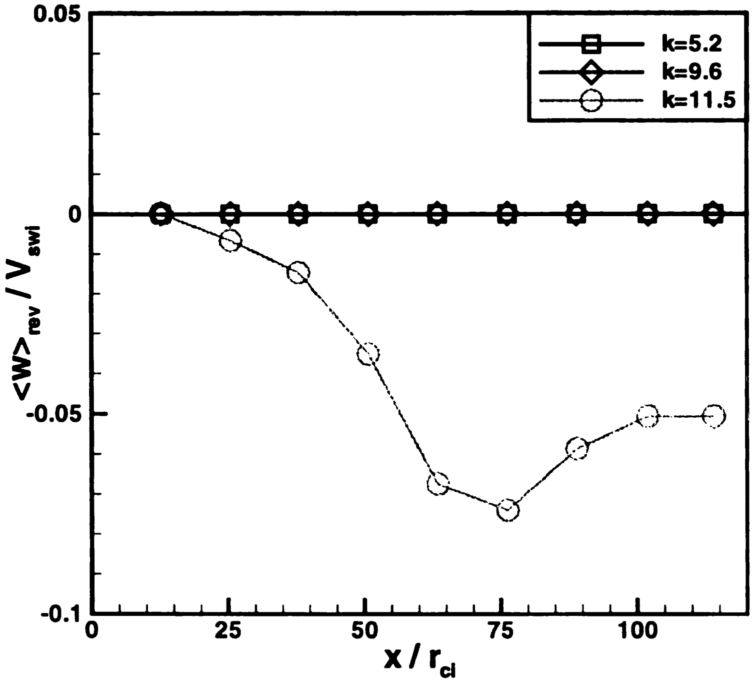

Figure 4-8: Peak reverse axial flow speed, $<w>_{rev}$, versus the reduced frequency for A=2° at z=10cm off the centerspan.

The maximum spanwise flow velocity in the measurement domain for each k (i.e. search through all measurements locations and find the highest magnitude spanwise flow for each k) was found using the data in Figure 4-4. The result is plotted in Figure 4-9 for the A = 2° cases. When the data were dimensional there was a nominally 700% increase in

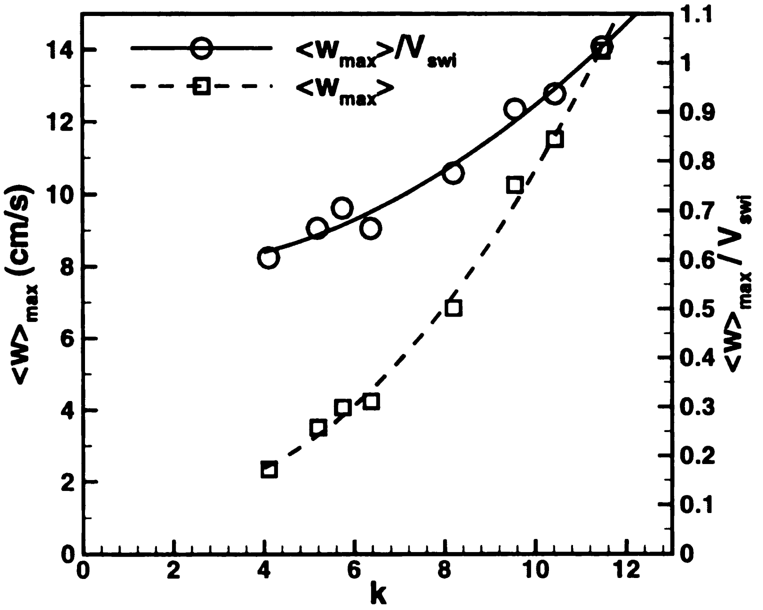

Figure 4-9: Maximum axial flow, $\langle w \rangle_{max}$, versus reduced frequency.

$\langle w_{max} \rangle$ from the lowest reduced frequency to the highest (2.3 cm/s to 14 cm/s). When the data were normalized with the swirl velocity, the difference was reduced to less than a 100% increase ($0.6V_{sw}$ to $1.0V_{sw}$). The curves plotted are 2nd order polynomial fits to the data and show good agreement over the reduced frequency range investigated.

The data from the line tagging experiments can be shown in contour form with y and phase being the axis variables (i.e., profiles as a function of phase). Figure 4-10 shows the data presented in this way for the A = 2° , k = 11.5 case at two downstream distances ($x = 38r_{ci}$, $88r_{ci}$). The spanwise flow show was confined to two isolated structures at the upstream location, that corresponded to the two vortices, for each phase at $x = 38r_{ci}$. The

**Figu
Dow
simu**

skev

line

shap

struc

sing

mag

wid

show

char

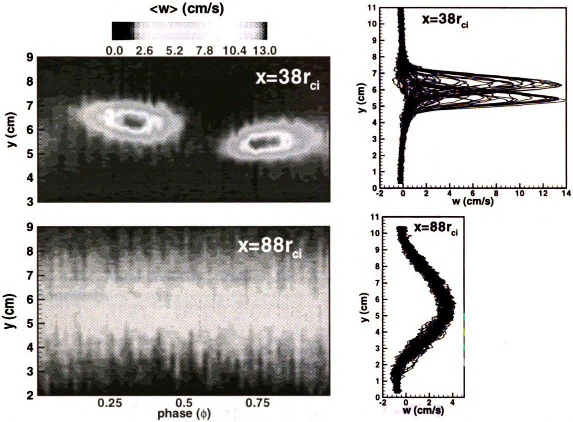

Figure 4-10: Spanwise flow versus vertical distance, y, and phase. A=2°, k=11.5. Downstream location indicated on figure. Line plots show all phases (i.e., y-profiles) simultaneously.

skewed shape of these structures was a result of the flow velocity parallel to the tagged line as discussed in Chapter 2. The velocity profiles in Figure 4-10 show Gaussian like shapes that corresponded isolated vortex cores. The two peaks correspond to the isolated structures in the vortex cores. Further downstream at x = 88r_{ci}, the axial flow was in a single diffuse band that spanned the entire phase rather than two isolated structures. The magnitude dropped significantly compared to the upstream case. The profile was also wider, and less steep than was observed at x = 38r_{ci}. The current discussion is intended to show that there was a change in the structure of the axial flow that implied a simultaneous change in the vortex structure. There were no vorticity data that accompany these

F
s

Fig
sim

mea

Figu

for k

the tr

not sh

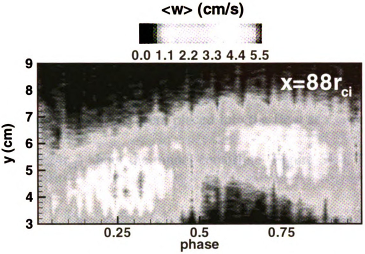

Figure 4-11: Axial velocity profiles for A=2°, k=9.6. Multiple phases shown simultaneously.

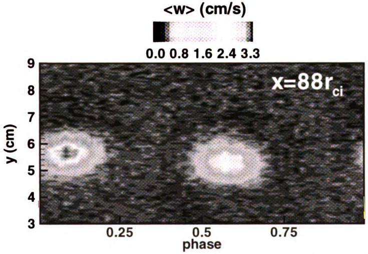

Figure 4-12: Axial velocity profiles for A=2°, k=5.2. Multiple phases shown simultaneously.

measurements, however the stereoscopic data in Chapter 5 do support the conjecture. Figure 4-11 shows the contour map of the transverse velocity versus y-location and phase for k=9.6. These data are from the furthest downstream measurement location and showed the transition from isolated structures. The same data for the k=5.2 case, Figure 4-12, did not show the transition.

b

e

g

F
lo

fo

th

m

th

CHAPTER 5

VORTEX / CUTTING WALL INTERACTION

The data in Chapter 3 and 4 (i.e. the "no-wall" experiments) presented the boundary conditions for the vortex/cutting wall interactions (i.e. the "cutting wall" experiments). The cutting walls were placed into the flow at x = 6cm (c/2, $15r_{ci}$), with a gap of ±9.5 cm ($\pm 24r_{ci}$) about the tunnel centerline (Figure 5-1). The coordinate system for this portion of the study is shown in Figure 5-1 and had an origin at the leading edge of the cutting walls. The wall location represents a compromise location. This was the minimum downstream location where the vortices were formed into isolated structures for the low reduced frequency (k = 5.2) case. The initial axial flow from the vortex/side wall

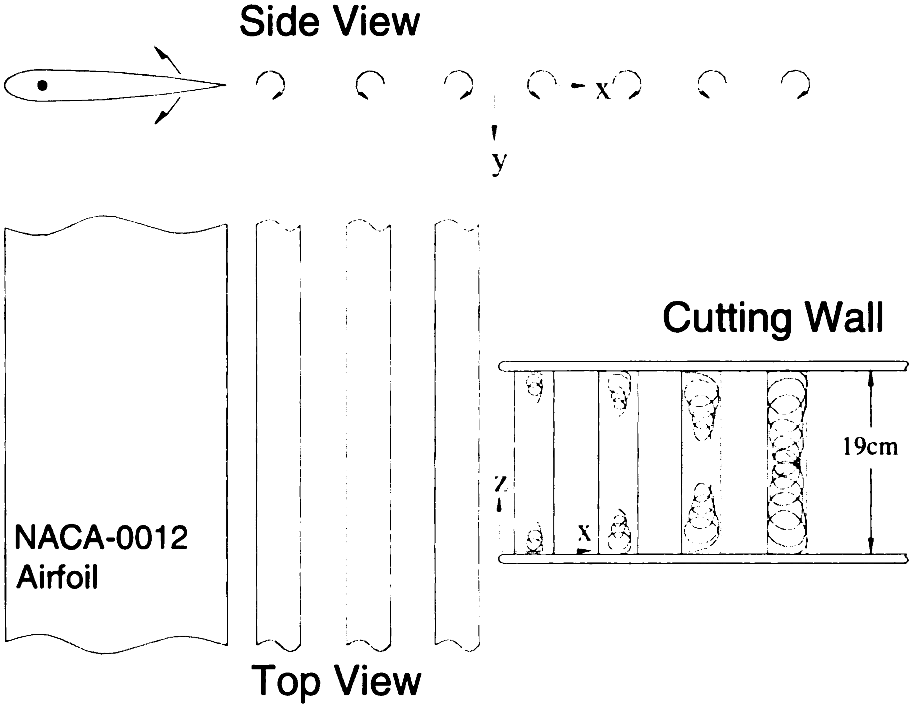

Figure 5-1: Schematic of flow field with cutting walls. Coordinate system origin is located at the cutting wall leading edge, as shown.

i

f

t

w

c

c

s

V

w

d

Fi

interaction has however already reached this span location for the highest reduced frequency cases (A = 2°, k = 9.6, 10.5, 11.5) with speeds of nominally 2 cm/s.

Marshal and Yalamanchili (1994) report that a cutting wall thickness greater than the vortex core radius results in distortion and bending of the vortex as it interacts with the wall. A wall thickness of r_{ci} or smaller results in no significant bending of the vortex. The cutting walls are made of 0.3 cm ($0.75r_{ci}$) thick clear acrylic to minimize effects from the cutting. The leading edge of the cutting walls were rounded to prevent separation around sharp edges. Marshall and Krishnamoorthy (1997) define the impact velocity, $V_i = U_c / V_{swi}$, and determined analytically that if $V_i > 0.25$ no separation on the cutting surface would occur before the vortex is cut. The impact velocity calculated from the midplane data is shown in Figure 5-2. All cases studied show $V_i > 0.25$ in this study.

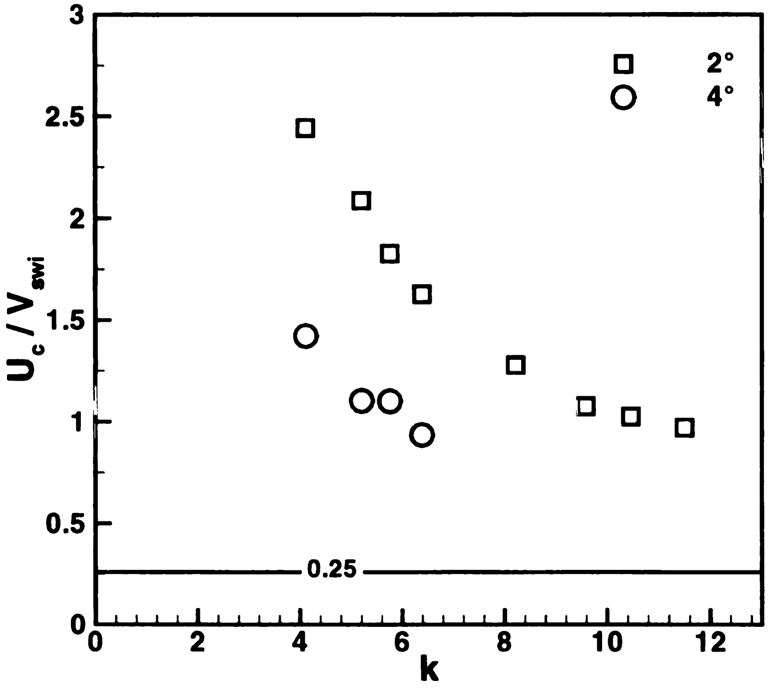

Figure 5-2: Impact speed, V_i, versus reduced frequency from the mid-span data.

The discussion in this chapter first centers on line tagging results with the cutting walls in place. These data were available for all cases and were used to determine which cases would be investigated in greater detail with stereoscopic MTV. Following those data the stereoscopic data for the k = 5.2, 9.6 and 11.5 (A = 2°) are presented. These data are organized around a discussion of the mean flow fields for all cases followed by the phase averaged flow fields with each case discussed individually. Finally a discussion of the data as it related to waves on vortex cores will be presented.

5.1 Line Tagging Results

Line tagging MTV was used initially to map out the extent and approximate magnitude of the spanwise flow for all cases. Measurements were taken at multiple span locations from $0.6r_{ci} \leq z \leq 25r_{ci}$ (0.24 - 10 cm) with an approximate spacing of $1.6r_{ci}$ (0.65 cm) and from $-13r_{ci} \leq x \leq 68r_{ci}$ (-5 - 27 cm) with steps of $2.5r_{ci}$ (1 cm). These data were processed in the same way as the data in Chapter 4 to provide the local peak spanwise flow and global maximum spanwise flow. Example velocity profiles for A = 2°, k = 11.5 at $x = 13r_{ci}$ for multiple span locations are shown in Figure 5-3. The phase of the peak axial flow (i.e. the velocity profile through the center of the vortex) is shown. Strong spanwise flow was measured, with significant reverse spanwise flow also observed near the wall. The peak spanwise flow increased in magnitude as z increased until the maximum was reached at $z \approx 4r_{ci}$. The spanwise axial flow then decreased as z increased. The reverse spanwise flow decreased away from the wall. The axial flow front had not reached the center of the cutting wall assembly at this downstream location.

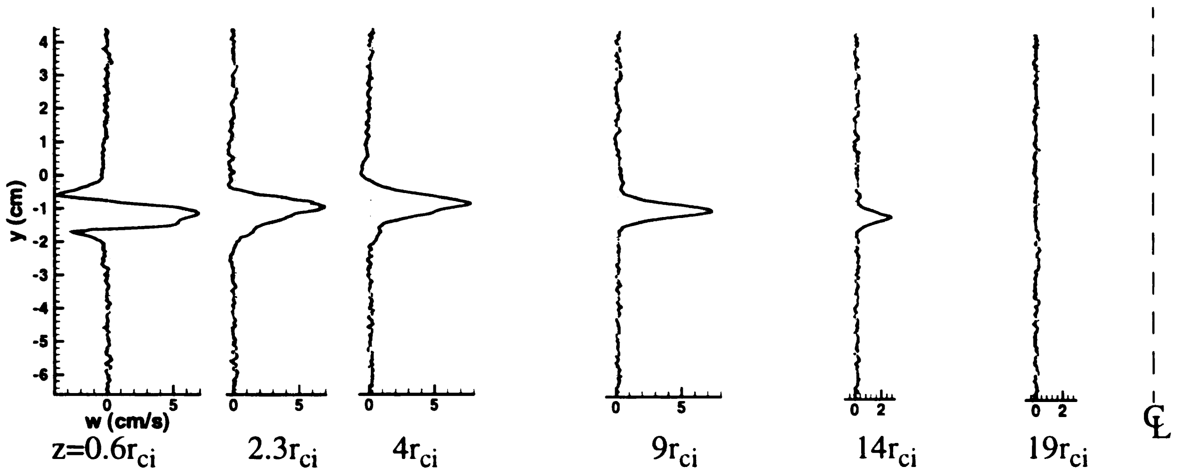

Figure 5-3: Example phase-averaged spanwise velocity profiles for A = 2°, k = 11.5, x = 13r$_{ci}$. Phase, ϕ, with the highest spanwise flow shown at each z location. Distance between profiles not shown to scale.

Contour maps of $<w>_{peak}$ over the entire spatial extent for k = 5.2 and 11.5 are shown in Figure 5-4 and 5-5. The reverse spanwise flow, $<w>_{rev}$, is also shown in Figures 5-4 and 5-5 and will be discussed later. Both cases show that the spanwise core flow begins near the wall and moves away towards the center of the tunnel with increasing downstream distance. No steady or constant axial flow condition was found after the axial flow was initiated. The axial flow "front" (i.e. the boundary between the spanwise flow / no-spanwise flow) advanced at a higher rate for the higher reduced frequency case.

When the axial flow versus the z-location was plotted as a function of downstream distance a local overshoot / undershoot or "spike" in the axial flow velocity with a peak to peak magnitude of $V_{os} = 0.19V_{sw}$ was observed near the axial flow front boundary (Figure 5-6). The velocity spike followed the front boundary as it progressed towards the center of the cutting wall. Spikes at the axial flow front boundary were observed for all k's (except k = 4.1, A = 2°) though the disturbance was weaker for lower k values (Figure 5-7). Stereopscopic data, presented later in this chapter, will show that this axial flow spike was

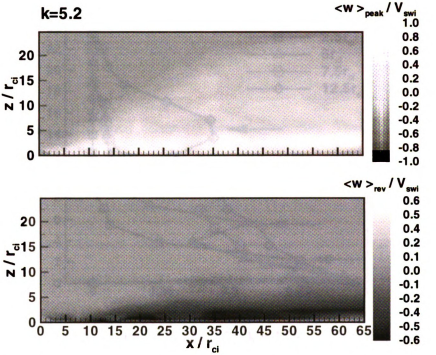

Figure 5-4: Peak spanwise flow speed for A = 2°, k=5.2.

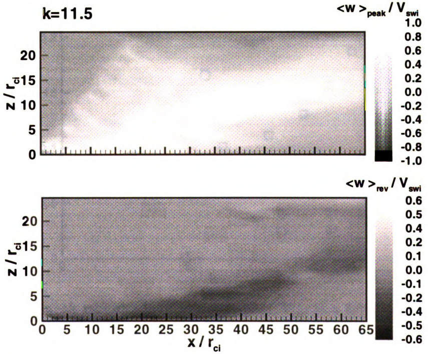

Figure 5-5: Peak spanwise flow speed for A = 2°, k = 11.5.

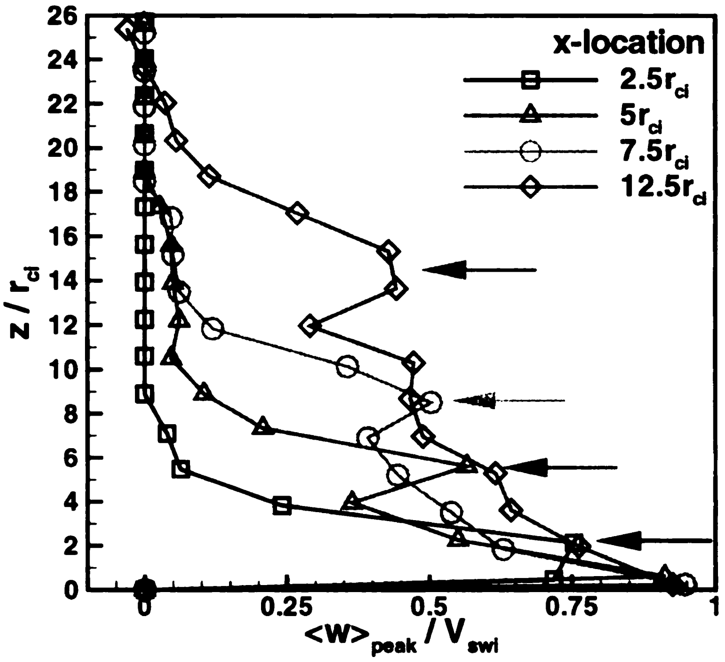

Figure 5-6: $<w>_{peak}$ versus spanwise location for k = 11.5.

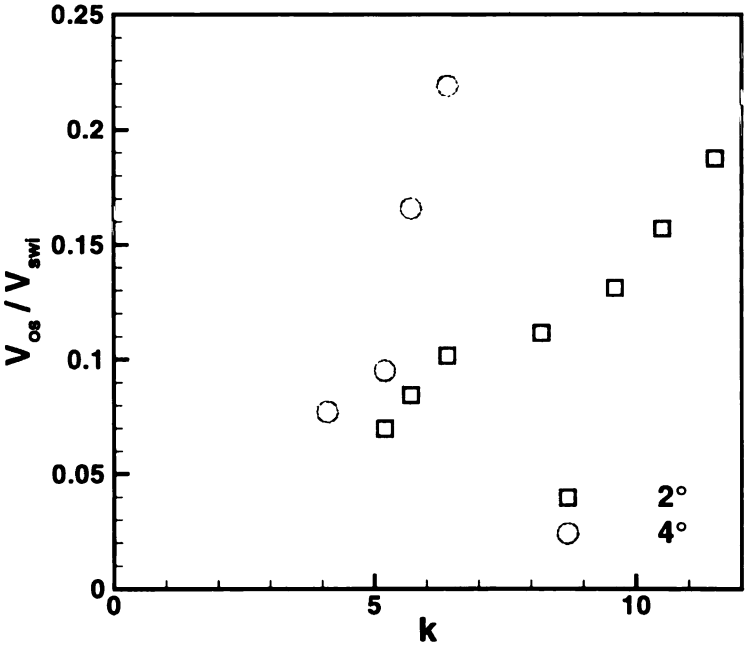

Figure 5-7: Peak to peak magnitude of velocity spike, V_{os}, as a function of reduced frequency.

associated with a local spike in the vorticity and for high k, a change in the vortex core area. These data are therefore initial evidence that area varying waves were present on the vortex. The $z = 12.5r_{ci}$ profile also showed evidence of other velocity spikes behind the axial flow front.

Two speeds were defined using the line tagging data. The front location was defined by the span location $\langle w_{peak} \rangle = 0.5$ cm/s. The threshold level was picked as it was relatively low, but above the measurement noise level. The front speed was determined by dividing the spanwise distance travelled, z, by the convection time (the midspan convection speed, U_c, multiplied by the downstream distance traveled, x). The speed of the spike was estimated by differentiating the span position of the peak level of the spanwise velocity spike by the convection time, as was done for V_f. Lundgren and Ashurst (1989) use the gas dynamics equations for an analogous description of the behavior of area varying waves on a vortex tube and define an equivalent "speed of sound" as:

$$c_e^2 = \frac{\Gamma^2}{8\pi A} \qquad (19)$$

The two wave speeds and the calculated values of c_e are also shown for the data in Figure 5-8. Both wave speeds increased as the reduced frequency increased. The speed of the spike, V_w, was less than the front speed, V_f, for all cases (Figure 5-8) which indicated that the axial flow front led the axial flow spike with an increasing distance. The sound speed, c_e, was higher than the wave speed, V_w, for low reduced frequencies. Equation (19), used to calculated c_e, was derived for a potential vortex with flat-topped axial flow. The stereoscopic data will show that the axial flow profile for the current work did not fit a

F
th

fl

w

th

Th

(Fi

≈ 4

cm

dist

inve

Thes

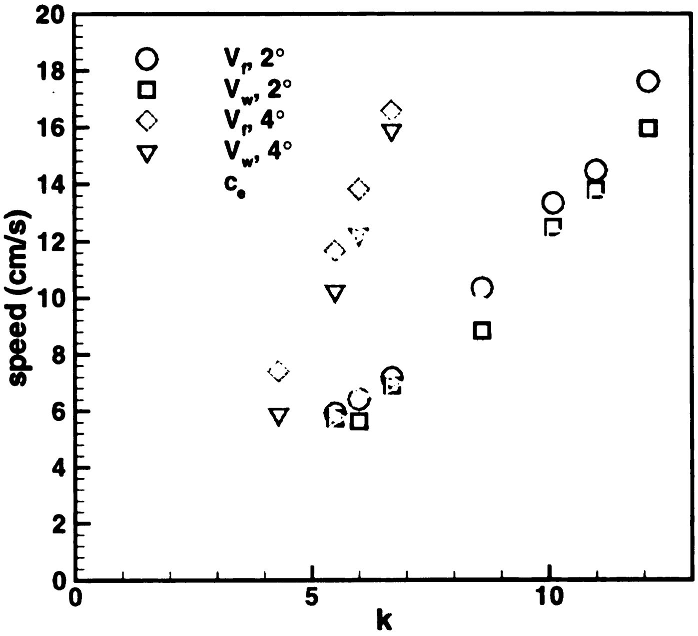

Figure 5-8: Comparison of the front speed, V_f, the wave spanwise flow speed, V_w, and the equivalent sound speed, c_e.

flat-top profile. The qualitative agreement was consistent with a small amplitude traveling wave on the vortex core.

The use of cutting walls placed symmetrically about the tunnel midspan means that the axial flow from the two sides meet at the midspan at some downstream distance. The axial flow generated from the symmetrically placed cutting wall was observed (Figures 5-4 and 5-5) when the axial flow front reached the cutting wall midspan plane, $x \approx 45r_{ci}$ for $k = 5.2$ and $x \approx 17r_{ci}$ for $k = 11.5$. The symmetry point was near $z \approx 23r_{ci}$ (9.5 cm) as expected.

The location of the peak axial flow moved away from the wall as the downstream distance increased. The global maximum spanwise flow observed over the spatial domain investigated, $<w_{max}>$, as a function of the reduced frequency is shown in Figure 5-9. These data showed good agreement with the no-wall cases for high reduced frequency

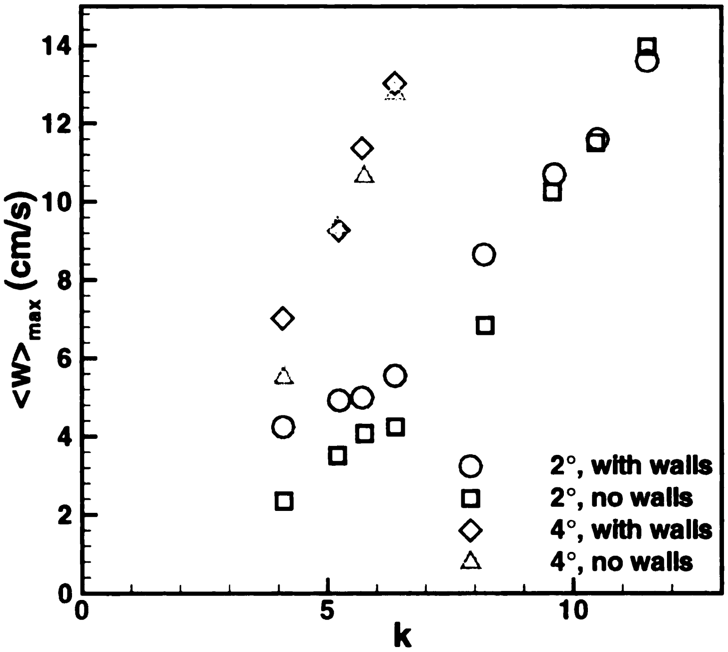

Figure 5-9: Maximum spanwise velocity, $<w>_{max}$ comparing no-wall and cutting wall experiments.

while at lower reduced frequencies $<w_{max}>$ for the no-wall experiments was lower. Figure 5-4, the low k case, indicated that while the maximum spanwise velocity occurred within $2.5r_{ci}$ of the wall. The maximum spanwise flow moved significantly farther away from the wall ($10r_{ci}$) for k = 11.5 (Figure 5-5). It was, therefore, not surprising that $<w_{max}>$ for the lower k no-wall experiments was smaller than the cutting wall cases since only a single z location, far away ($\sim 40r_{ci}$) from the side walls, was measured for the no-wall experiments.

The measurements revealed a significant reverse spanwise flow (Figure 5-4 and 5-5) with magnitudes of nominally half those for the axial core flow. The span location of the peak reverse, $<w_{rev}>$, flow for the k = 11.5 case was observed to move away from the cutting wall as was noted for $<w_{peak}>$. Maximum $<w_{rev}>$ levels are shown in Figure 5-10. The highest $<w_{rev}>$ measured for the A = 2° cases occurred for k=9.6 then decreased for

Figur

k=10.

satisfi

phases

observ

region

increas

approa

much h

flow fo

occurri

downst

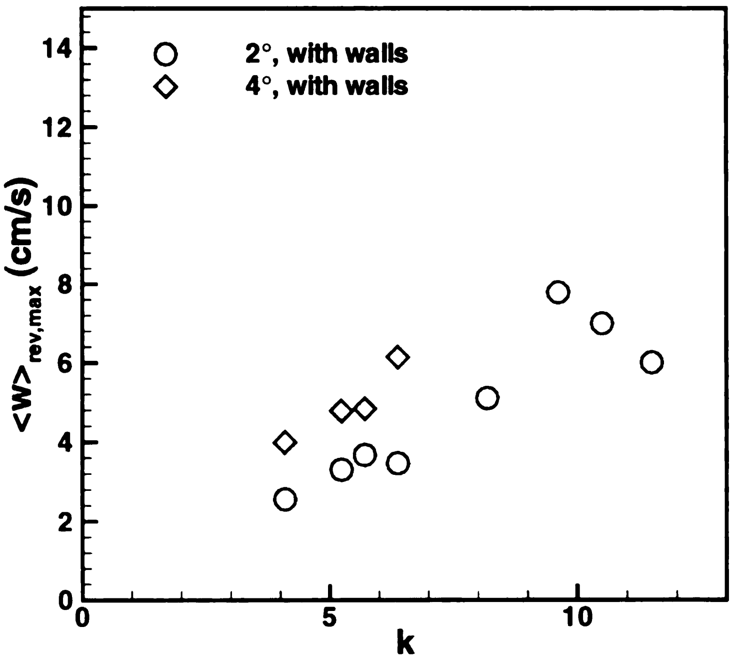

Figure 5-10: <w>$_{rev}$ as a function of the reduced frequency.

k=10.5 and 11.5. The presence of reverse spanwise flow is required so that continuity is satisfied (i.e. to balance fluid transported away from the cutting walls).

Figure 5-11 shows the spanwise velocity profiles for A = 2° k = 11.5, with all phases plotted, at $x = 58r_{ci}$. This figure provides a comparison with Figure 4-9. It was observed that for the no-wall cases the axial flow structure changed from two isolated regions per phase to a single band of spanwise flow as the downstream distance was increased. This was also observed with the cutting walls. Near the wall the axial flow approached zero ($z = 0.6r_{ci}$, Figure 5-5 and 5-11) though at an equivalent z-location it was much higher upstream (e.g. at $z = 0.6r_{ci}$, $x = 20r_{ci}$, Figure 5-5). A single band of spanwise flow for all phases was observed for $z < 4r_{ci}$ with a transition to two isolated structures occurring between $4r_{ci}$ and $9r_{ci}$. Multiple structures were observed for $z > 9r_{ci}$ at this downstream location. The less pronounced spanwise flow peaks in Figure 5-11 were a

F
pr

re

m

sp

no

str

inv

5.2

mo

The

wel

the

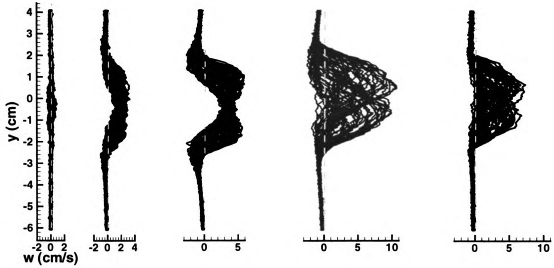

z=0.6r_{ci} 4r_{ci} 9r_{ci} 14r_{ci} 19r_{ci}

Figure 5-11: Spanwise velocity profiles for A = 2°, k = 11.5, x = 58r_{ci} all phases (i.e. y-profiles) shown.

result of the increased downstream distance of the data in Figure 5-11 compared to the multi-structure plot in Figure 4-9. These data were instructive in that the additional spanwise measurement locations indicated that the change in structure initiated near the no-slip boundary and propagated away from the wall. No transition from two to one structure was observed for the low reduced frequency case over the downstream range investigated.

5.2 Stereoscopic Results

The data in Section 5.1 were used to define the experimental parameters for the more detailed stereoscopic measurements. The cases chosen were A = 2° k = 5.2, 11.5. The k=5.2 and 11.5 cases were chosen because the represent the lowest vorticity level with well defined vortices at x = 6cm downstream (k = 5.2), and the highest vorticity value in the parameter range (k = 11.5). Four spanwise planes z = r_{ci}, 2r_{ci}, 10r_{ci}, 20r_{ci} (0.4cm,

0.
ec
10
ap
by
dis
an
up
op

wa
est
the
was
lase
mos
FO
imp
whe
desc
unce

sMT

0.8cm, 4cm, 8cm) were investigate. The z = r_{ci}, $2r_{ci}$ cases started upstream of the leading edge of the cutting wall and extended to approximately $50r_{ci}$ (20 cm) downstream. The z = $10r_{ci}$, $20r_{ci}$ cases began downstream of the cutting wall leading edge and also extended to approximately $50r_{ci}$ (20 cm) downstream. The initial portion of the data sets were affected by optical issues resulting from the leading edge of the cutting walls. The optical distortion resulted in erroneous data in those regions which was not used or shown in the analysis below with a single exception. The phase-averaged vorticity plots do include the upstream vorticity. The vorticity fields did not appear to be qualitatively affected by the optical issues, and so are shown for visual affect.

The stereoscopic data sets were taken with the laser sheet parallel to the cutting walls. There was a spatial uncertainty in the spanwise location of the laser sheet. It was estimated that at the measurement location the laser sheet was $0.13r_{ci}$ (0.05 cm) thick. For the z = r_{ci} (0.4 cm) measurement plane the spanwise gradients were large, and the data set was affected by the uncertainty in the laser sheet placement. This was because of finite laser sheet thickness (~ 0.5 mm) and the method used for beam placement. This error was most apparent in the mean data which did not show good agreement between the small FOV's. The data from this measurement plane were included here because they provide important information about the flow field near to the cutting wall but care must be taken when analyzing the data given the additional source of measurement uncertainty described. The remaining planes did not show the effect of the laser sheet placement uncertainty.

A comparison of the spanwise velocity component between the line tagging and sMTV data sets is shown in Figure 5-12. The sMTV data (lines in Figure 5-12) show clearly the initial local spike in the spanwise flow already discussed. In addition these data also show multiple secondary spikes in the peak spanwise flow. The line tagging data do not show the secondary spikes. This may be due in part to the data density in the streamwise distance for the line tagging data which was coarse compared to the stereoscopic data. Figure 5-12 is instructive because these data show excellent agreement between the data sets which allows later discussion using the information from the different the data sets.

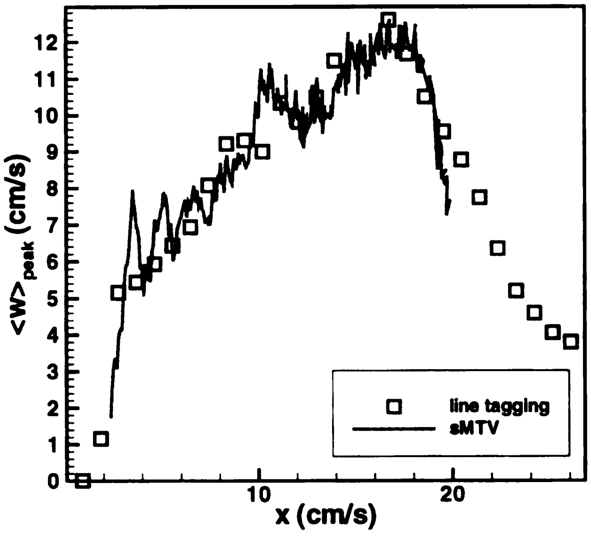

Figure 5-12: Comparison of the peak spanwise velocity between the line tagging and sMTV data.

5.2.1 Mean Flow Field, k=5.2, 11.5

A comparison of the average streamwise velocity fields near the tunnel midspan is show in Figure 5-13 for k = 11.5. These data show the repeatability of the mean streamwise flow field was to within 2% near the centerline (y=0), and better than 0.5% for the freestream between the no-wall and cutting wall experiments. Good agreement between the no-wall experiments and cutting wall experiments (near the midspan) was

Fi
mi

als

wa

no

ap

bo

in

ve

th

ar

re

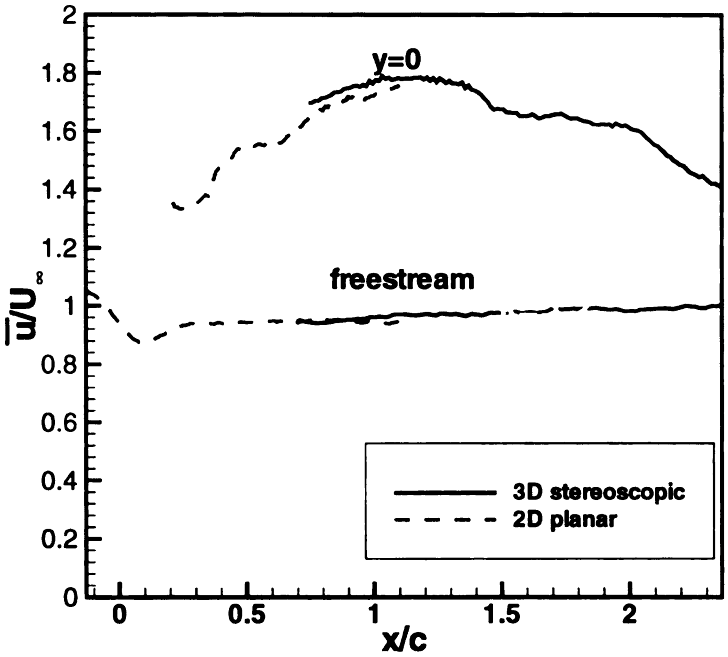

Figure 5-13: Comparison of the planar (midplane) and stereoscopic (z=8cm, near midplane) measurements of the mean streamwise velocity, $\bar{u}$, for k=11.5.

also observed (but not shown here) in the mean flow data. These data indicate the cutting walls did not change the base flow field significantly from the no-wall experiment.

The freestream showed an acceleration for the cutting wall experiment that was nominally uniform for all cases and span locations considered. The speed increased approximately 4% over the 20cm streamwise experimental fetch. Laminar flat plate boundary layer analysis on the facility walls (cutting and side) predicted a 2% velocity increase over the same range because of boundary layer growth. The remainder of the velocity increase was accounted for by the non-planar shape of the thin acrylic walls (i.e. there was a bulge in the cutting walls) near the middle of the plate which decreased the area and increased the mean flow speed.

The mean streamwise velocity fields for k = 5.2 are shown in Figure 5-14. The low reduced frequency case showed an decreasing wake thickness as a function of the distance

Fig

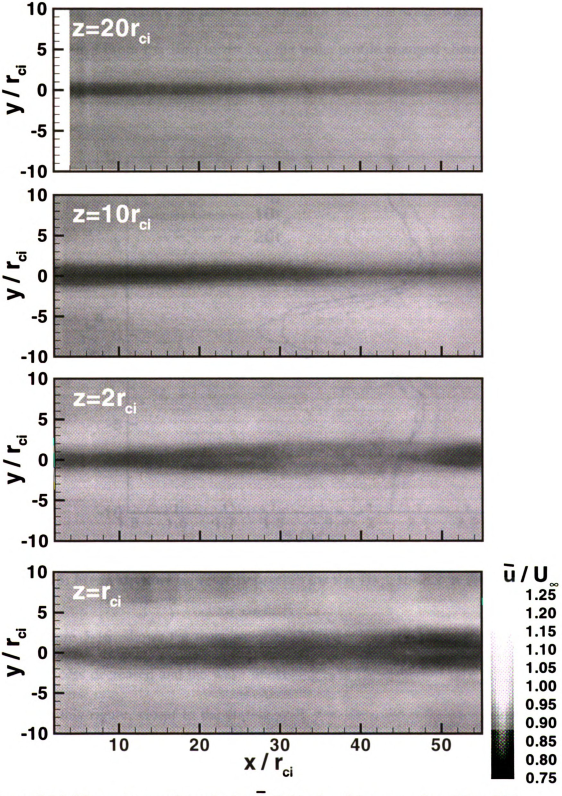

Figure 5-14: Mean streamwise velocity, $\bar{u}$, fields, k = 5.2, z = r_{ci}, $2r_{ci}$, $10r_{ci}$, $20r_{ci}$.

1

(

2

r

F

ve

st

be

re

from the wall. Mean velocity profiles at x = $11r_{ci}$ (Figure 5-15) show that the velocity deficit increased and formed an increased overshoot while the wake widened from z = $20r_{ci}$ to z = $10r_{ci}$. From z = $10r_{ci}$ to z = $2r_{ci}$ the wake profile changed character with the mean velocity becoming flat across the wake.

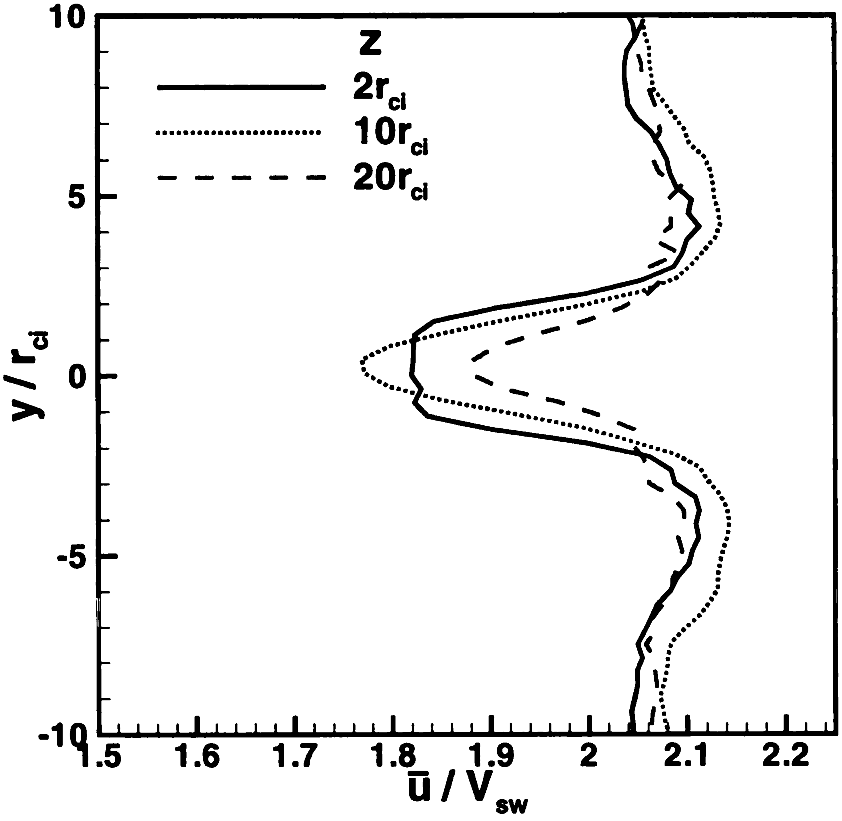

Figure 5-15: Mean streamwise velocity profiles for x = $11r_{ci}$, k = 5.2 at different z's.

Figure 5-16 shows the mean velocity fields for k = 11.5. The mean flow field velocity excess decreased and the wake thickening near the centerline (z = $20r_{ci}$). More striking in this figure, closer to the cutting wall, z = $10r_{ci}$, the wake showed the same behavior until x ≈ $45r_{ci}$ when the wake changed from a velocity excess split into two regions with a velocity deficit between. While the split of the wake was more evident at z

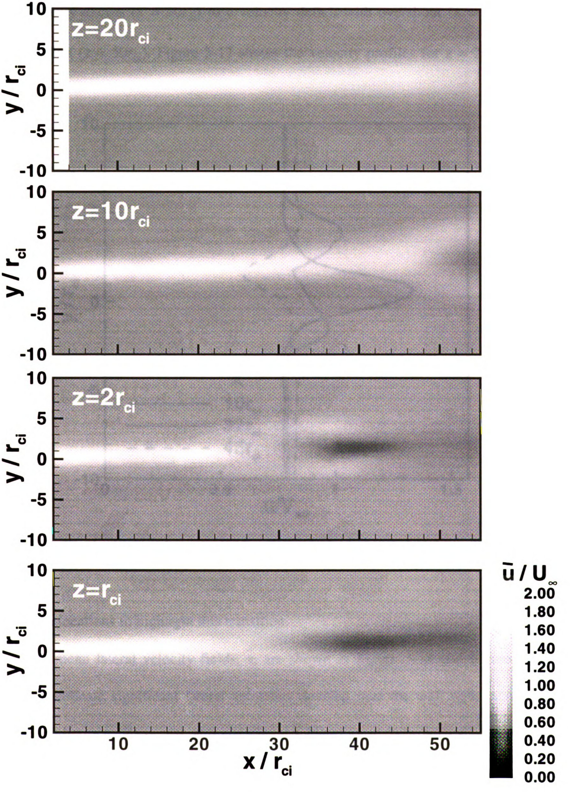

Figure 5-16: Mean streamwise velocity, $\bar{u}$, fields, k = 11.5, z = r_{ci}, $2r_{ci}$, $10r_{ci}$, $20r_{ci}$.

= r_{ci} and $2r_{ci}$, these locations continue to develop and show the wake profile transitions from a velocity excess ($x = 10r_{ci}$) to a velocity deficit with overshoot ($x = 39r_{ci}$) to a velocity deficit ($z = 50r_{ci}$). Figure 5-17 shows the velocity profiles for $z = 2r_{ci}$ at three

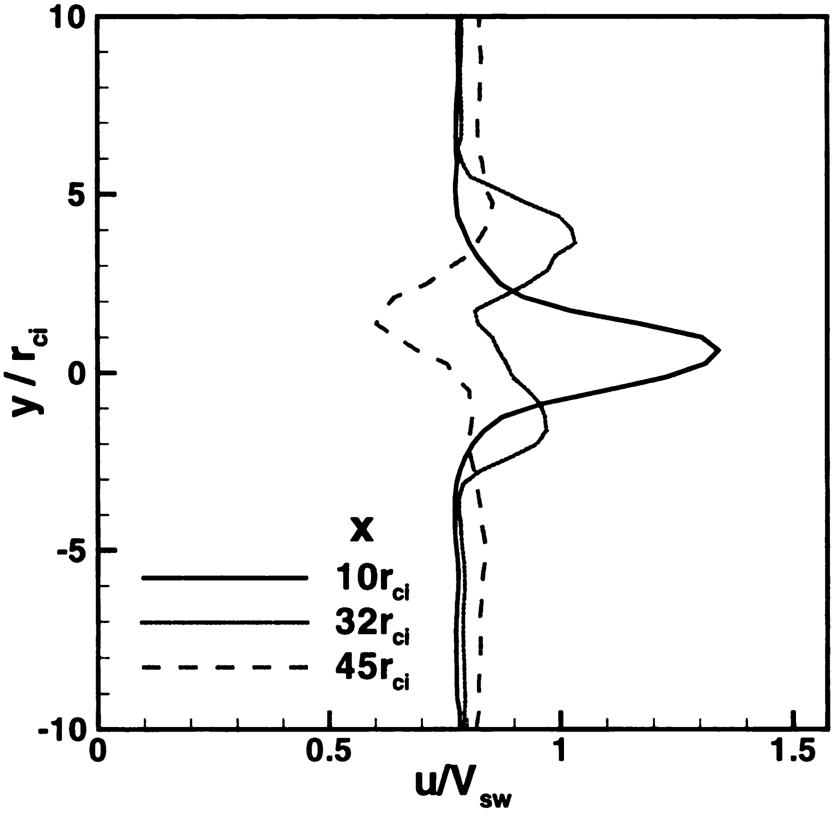

Figure 5-17: Mean streamwise velocity profiles for three downstream positions at $z = 2r_{ci}$, $k = 11.5$.

downstream locations to highlight this transition.

The mean lateral velocity fields, $\overline{v}$, are shown in Figure 5-18 and Figure 5-19. These data indicate significant lateral velocities develop near the wall with increasing downstream distance. There was also significant $\overline{v}$ found away from the wall. This was a significant departure from $\overline{v} = 0$ measured at the midspan in the no-cutting wall experiment.

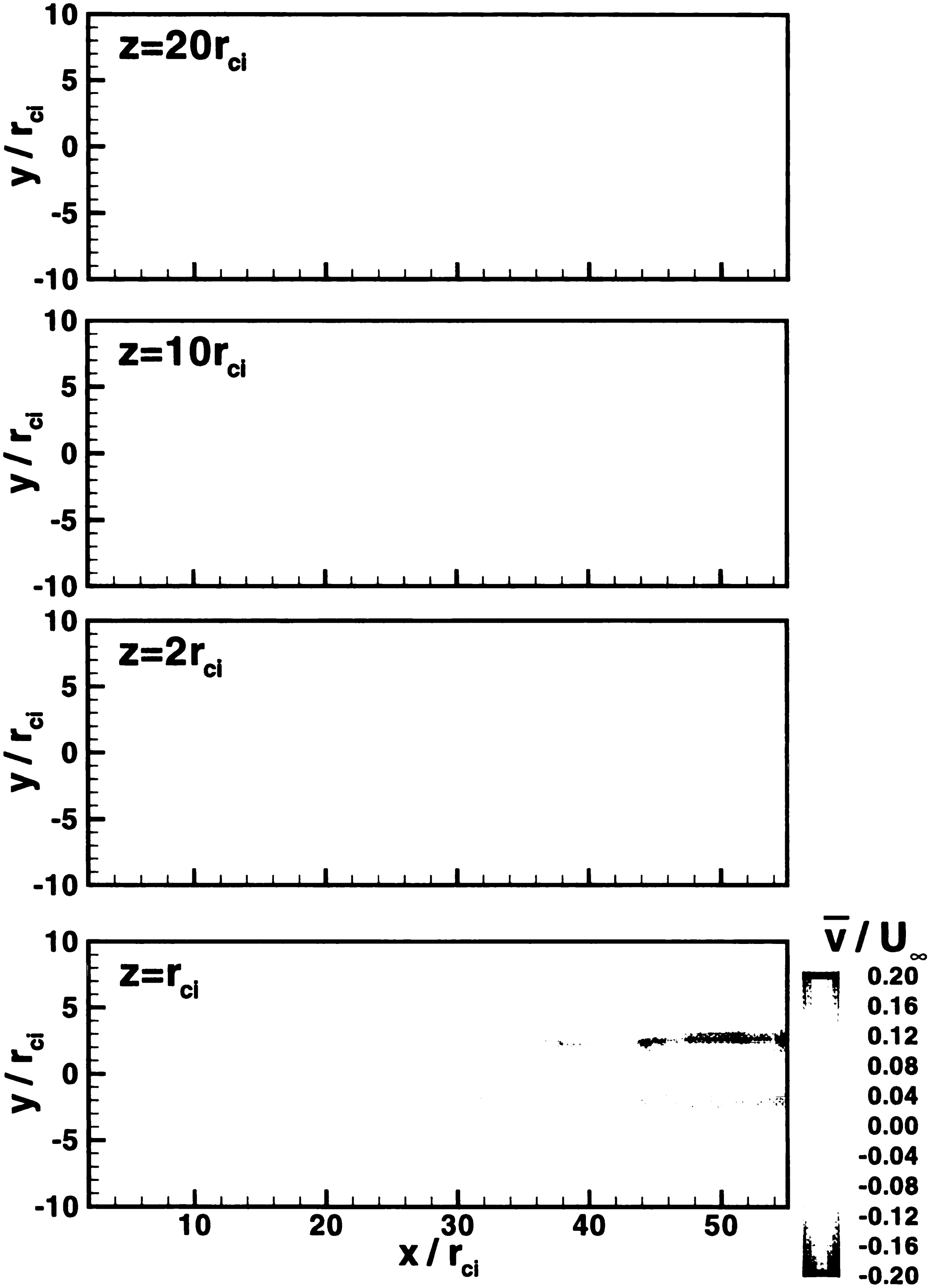

Figure 5-18: Mean lateral velocity, $\bar{v}$, fields, k = 5.2, z = r_{ci}, $2r_{ci}$, $10r_{ci}$, $20r_{ci}$.

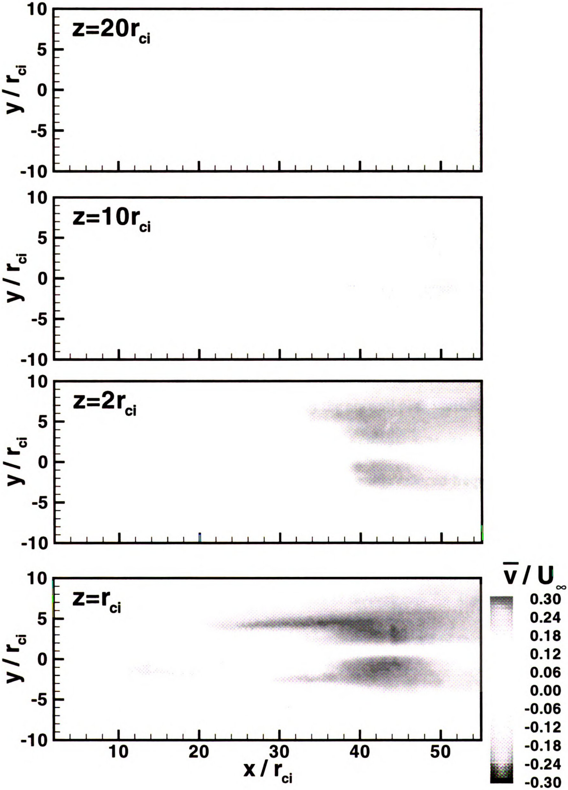

Figure 5-19: Mean streamwise velocity, $\bar{v}$, fields, k = 11.5, z = r_{ci}, $2r_{ci}$, $10r_{ci}$, $20r_{ci}$.

The mean vorticity field for the low reduced frequency case, k=5.2, is shown in Figure 5-20. The mean vorticity field near the centerline, $z = 20r_{ci}$, was nearly uniform in thickness and magnitude for $x < 35r_{ci}$ after which the lateral separation between the two signs of vorticity increase slightly. At $z = 10r_{ci}$ the vorticity field was noticeably thicker, though still of nominally uniform thickness as a function of x. The vorticity field at $z = 2r_{ci}$ was qualitatively similar to that observed at $z = 10r_{ci}$ for $x < 15r_{ci}$. The two signs of vorticity separated laterally for $x > 15r_{ci}$, with no mean vorticity between the layers consistent with the flat region in the mean velocity profile showing (Figure 5-14). For $x > 45r_{ci}$ the layers thickened and the lateral spacing decreased. The mean vorticity field at $z = r_{ci}$ showed multiple regions of non-zero mean vorticity indicating that multiple vortical structures must be present at this span location.

The mean spanwise vorticity, normalized by the no-wall peak vorticity (Table 4-1), for the high reduced frequency case, k = 11.5, is shown in Figure 5-21. The orientation of the mean spanwise vorticity field reversed orientation for this reduced frequency case at all span locations except $z = 20r_{ci}$. Close to the wall, $z = r_{ci}$ and $2r_{ci}$, the orientation of the vorticity changes between 25 and $30r_{ci}$, consistent with the mean velocity field (Figure 5-16). The $z = 10r_{ci}$ case also shows the reversal farther downstream for $x > 45r_{ci}$. At $z = 20r_{ci}$ the vorticity layer was beginning to switch orientation at the end of the measurement extent.

The mean spanwise velocity fields for the low and high reduced frequency cases are shown in Figure 5-22 and Figure 5-23. The spanwise flow from the vortex cores entered into the flow field for $x > 0$ and $10r_{ci}$ ($z = r_{ci}$ and $2r_{ci}$ respectively). At $z = 10r_{ci}$ the

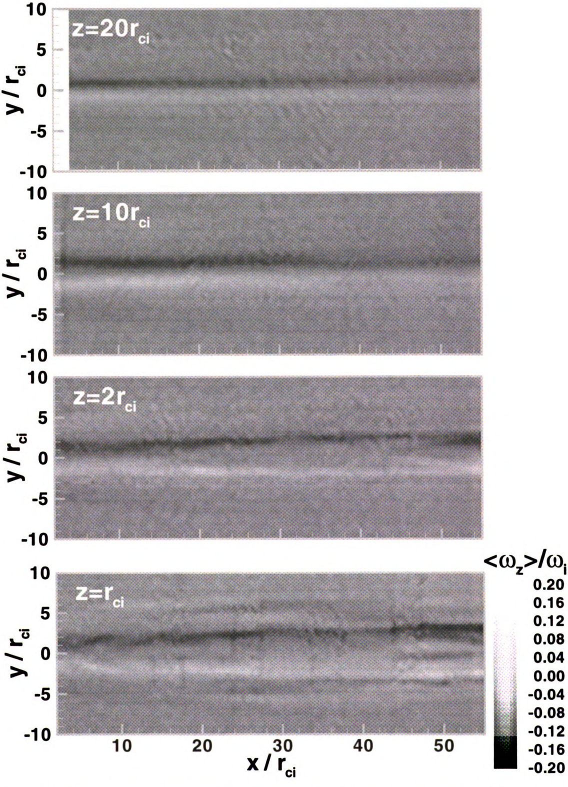

Figure 5-20: Mean spanwise vorticity, $\overline{\omega}_z$ fields, k = 5.2, z = r_{ci}, $2r_{ci}$, $10r_{ci}$, $20r_{ci}$.

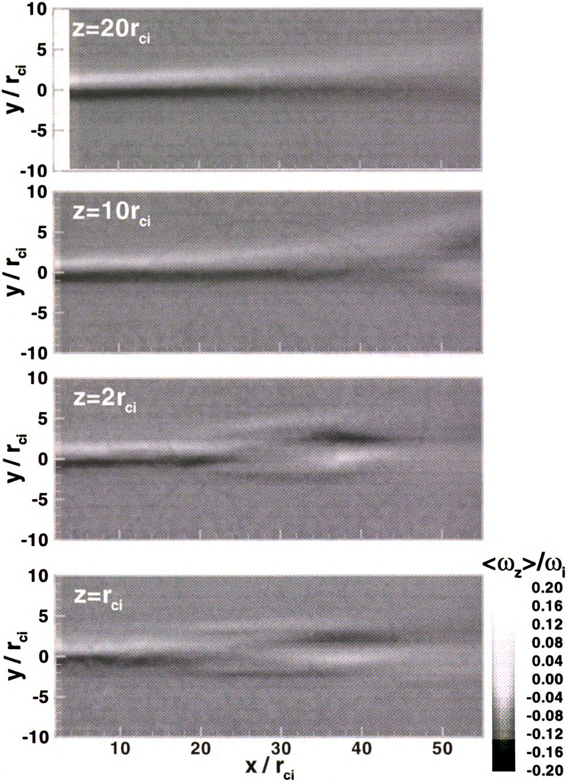

Figure 5-21: Mean spanwise vorticity, $\overline{\omega}_z$ fields, k = 11.5, z = r_{ci}, $2r_{ci}$, $10r_{ci}$, $20r_{ci}$.

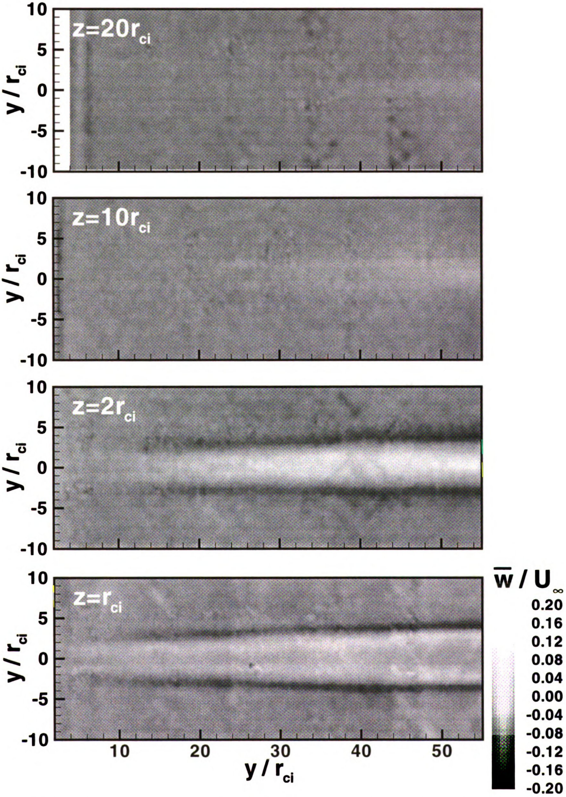

Figure 5-22: Mean spanwise velocity, $\overline{w}$, fields, k = 5.2, z = r_{ci}, $2r_{ci}$, $10r_{ci}$, $20r_{ci}$.

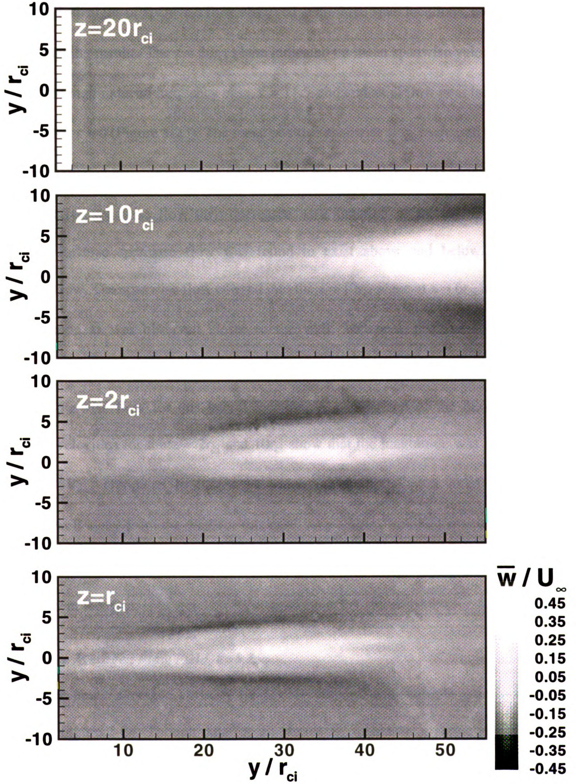

Figure 5-23: Mean spanwise velocity, $\overline{w}$, fields, k = 11.5, z = r_{ci}, $2r_{ci}$, $10r_{ci}$, $20r_{ci}$.

axial flow was observed for $x > 40r_{ci}$. The magnitudes were about 30% of those measured at $z = r_{ci}$. Both signs of spanwise flow observed at all three span locations, consistent with the line tagging results. The $z = 20r_{ci}$ plane indicated no mean spanwise velocity.

The high reduced frequency case, $k = 11.5$, showed axial flow near the wall, $z = r_{ci}$ and $2r_{ci}$, for $x \approx 0$ (Figure 5-23). The mean positive spanwise flow increased in magnitude for increasing downstream distance until the peak level which occurred near $x = 35r_{ci}$. The mean positive spanwise flow then decreased as a function of increasing downstream distance. Reverse spanwise flow was found to exist above and below the positive spanwise flow. The spanwise flow entered into the $z = 10r_{ci}$ plane at $x \approx 6r_{ci}$ and increased in magnitude as was observed closer to the wall. The peak positive spanwise flow occurred at $x \approx 46r_{ci}$. Reverse spanwise flow was also observed above and below the positive spanwise flow for this lateral location. A comparison of the maximum mean spanwise velocities for the $z = 2r_{ci}$ and $10r_{ci}$ show that the magnitude was largest at $z = 10r_{ci}$ ($0.35V_{swi}$ compared to $0.26V_{swi}$) which indicated the peak axial flow speeds occurred well away from the wall for this case. At $z = 20r_{ci}$ minimal spanwise flow was observed until $x \approx 30r_{ci}$. No significant reverse spanwise flow was observed at this measurement location.

5.2.2 Phase Averaged Flow Field, k=5.2.

The phase averaged vorticity field, $<\omega>$, for $\phi=0$ and multiple span locations is shown in Figure 5-24. Though data for all phases are available, a single phase, $\phi=0$, is shown as being representative of the "instantaneous" vorticity and velocity fields. These data show the downstream and spanwise development of the vorticity field. Close to the

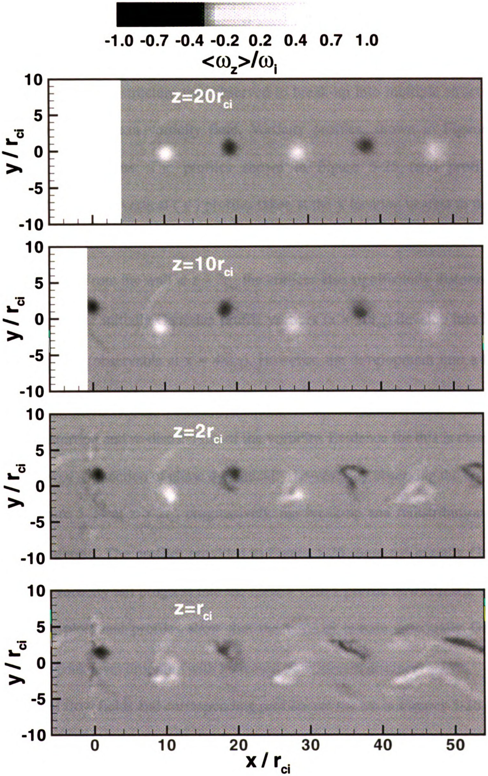

Figure 5-24: Phase-averaged vorticity, <ω>, for φ=0 at multiple span locations. k=5.2.

cutting walls ($z = r_{ci}$) the vorticity quickly looses its initial shape ($x \approx 0$) with distributed multiple, rather than a single, peaks ($x \approx 10r_{ci}$). The vortices continue to deform as the downstream distance increased with skewed, highly stretched rather than round structures formed. The initial single structure was observed to break-up into multiple structures as was inferred from the mean vorticity field. Vorticity profiles, shown in Figure 5-25, confirm these observations. The profiles shown in Figure 5-25 (and profiles for subsequent sections) were vertical (y) profiles taken at the x-location nearest to the peak vorticity location.

Farther away from the wall at $z = 2r_{ci}$ the vortices also significantly distorted from their initial shape. The initially Gaussian profile vortices ($x \approx 10r_{ci}$) develop into hollow core profile vortices (observable at $x \approx 48r_{ci}$). However, the development into a hollow vortex was not as a result of the decrease in the central peak vorticity of the Gaussian profile, but a distortion and re-distribution of the vorticity. Evidence for this is clear when the data are viewed as function of phase dynamically, however by observing the regions of vorticity in Figure 5-24 at $z = 2r_{ci}$ progressively, the break-up and redistribution of the vortex can be inferred. The profiles provided in Figure 5-25 show the initially Gaussian profile with the vorticity tail progress into the hollow vortex profile downstream. The $z = 10r_{ci}$ and $20r_{ci}$ plots and profiles show that the vortices remain essentially Gaussian shaped with the peak level dropping with increased downstream distance.

The axial flow fields and corresponding profiles are shown in Figures 5-26 and 5-27 respectively. Note the profiles shown in Figure 5-27 (and subsequent profile figures) correspond to the same spatial location of the vorticity profiles shown in Figure 5-25. At $z = r_{ci}$ the axial flow profiles do not have a Gaussian distribution or even round shape,

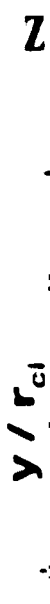

Fi
0.

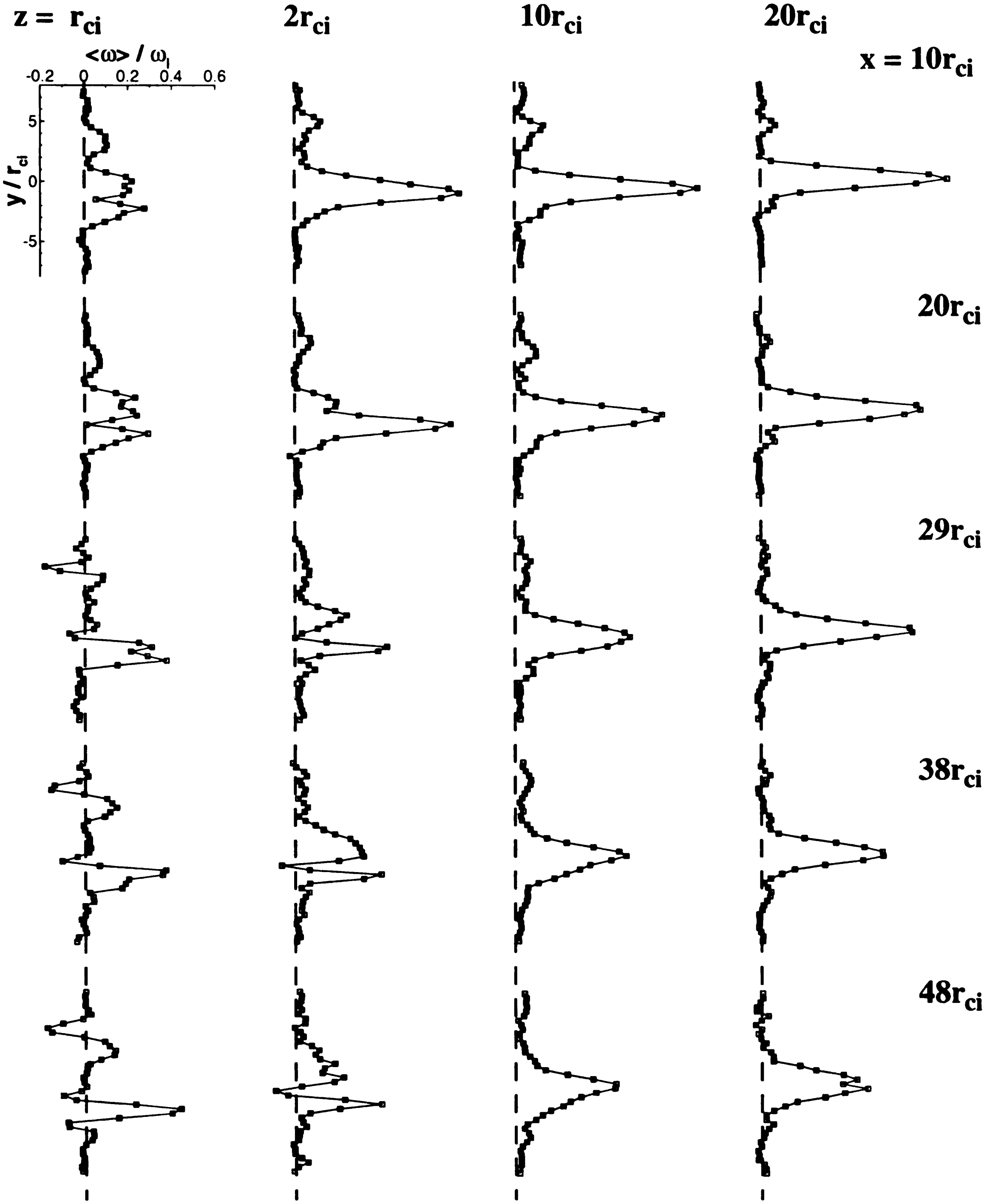

Figure 5-25: Phase-averaged vorticity, <ω>, profiles for k = 5.2. Dashed lines <ω> = 0. Spacing of profiles in figure not to scale.

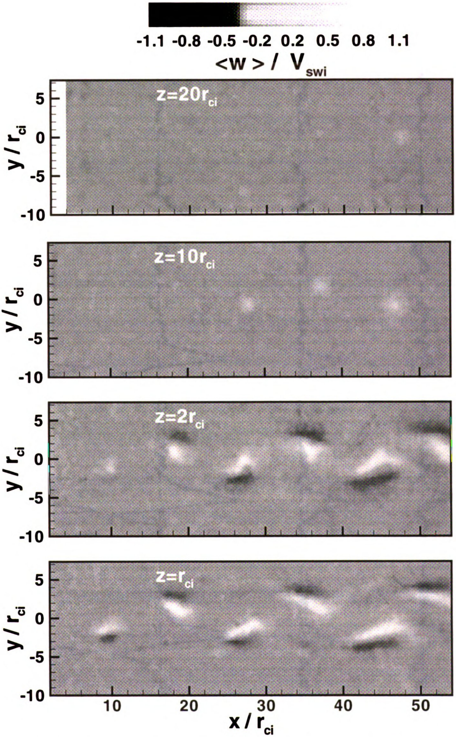

Figure 5-26: Phase-averaged spanwise velocity, <w>, for $\phi=0$ at multiple span locations. k=5.2.

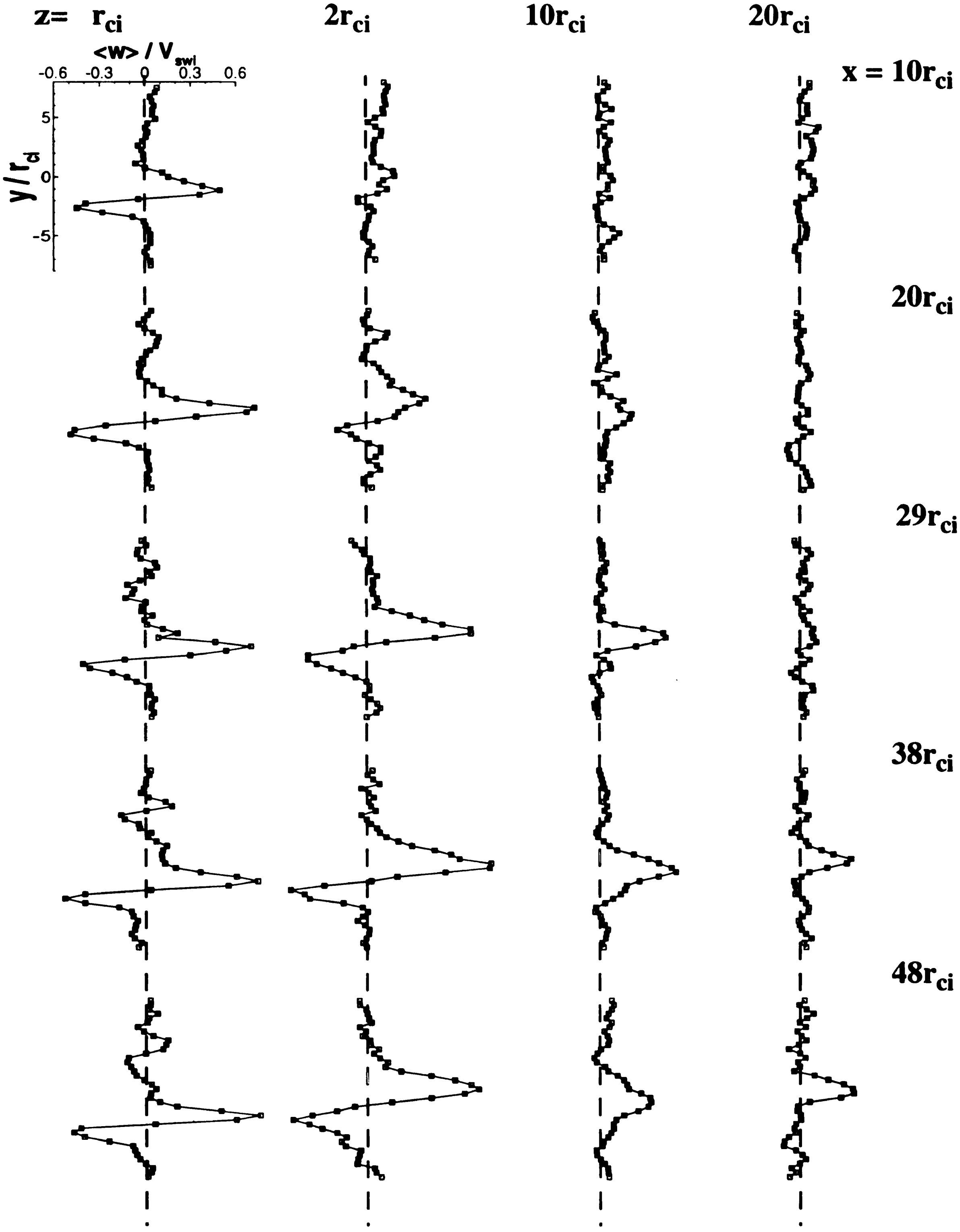

Figure 5-27: Phase-averaged spanwise flow, <w>, profiles for k = 5.2. Dashed lines <w> = 0. Spacing of profiles in figure not to scale.

rather a local maximum and minimum spanwise flow level is observed. The positive and negative spanwise flows were nearly equal in magnitude. As the downstream distance increased the spanwise flow profiles were similar, though the peak levels changed. The contour data of Figure 5-26 indicate that the spanwise flow field also skewed into oblong structures shaped qualitatively similar to the vorticity structures at the same downstream distance. At $z = 2r_{ci}$ the spanwise velocity was near zero initially and developed a profile similar to the $z = r_{ci}$ profiles. Peak levels were higher at this span location compared to the $z = r_{ci}$ location.

The spanwise flow fields for $z = 10r_{ci}$ and $20r_{ci}$ were significantly different from those observed for $z = r_{ci}$ and $2r_{ci}$. At $z = 10r_{ci}$ the spanwise flow was near zero for $x < 15r_{ci}$ after which a single peak, Gaussian like profile was observed. The peak level increase until $x \approx 40r_{ci}$ after which it decreased. No significant reverse spanwise flow was observed. For $z = 20r_{ci}$ the same trend was observed, but the development was further downstream.

The vortex parameters were determined by tracking the vortex through its downstream evolution as discussed in section 3.2.4. Figure 5-28 shows a comparison of several vortex parameters between the no-wall midspan data and the cutting wall $z = 20r_{ci}$ (the span location closest to the midspan) data. These data show good agreement between the two data sets. The circulation was lower, by nominally 2 cm^2/s, for the cutting wall data. This difference was near to the previously discussed uncertainty level in that measure.

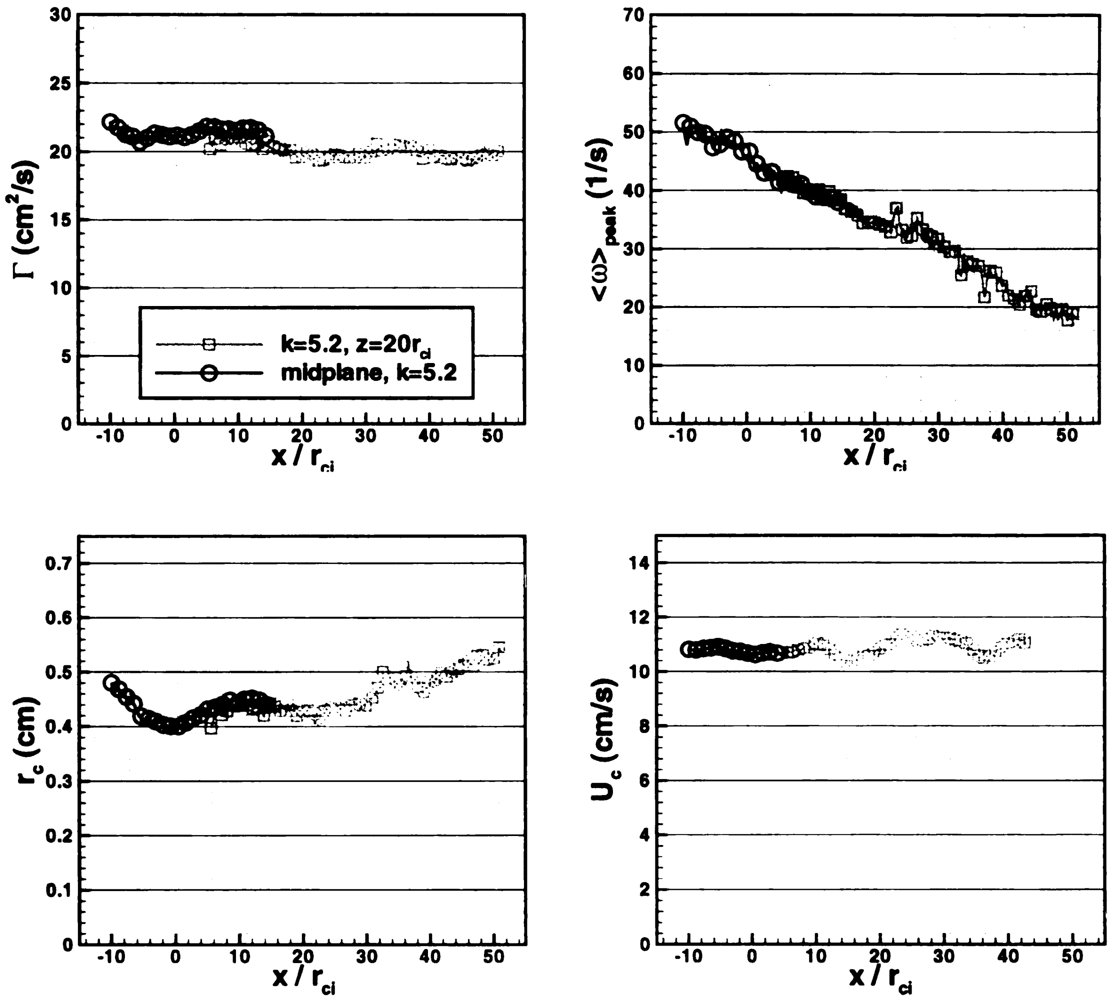

Figure 5-28: Comparison of vortex parameters (Γ, $<\omega>_{peak}$, r_c, U_c) from no-wall midspan data and cutting wall, $z = 20r_{ci}$ (near midspan) data. $k = 5.2$. Symbols common.

The vortex parameters for the $k = 5.2$ case are shown in Figure 5-28 for multiple z-locations. The local vortex parameters, Γ, $<\omega>_{peak}$, r_c, U_c, and $<w_{peak}>$ are shown normalized by the initial vortex parameters, Γ_i, ω_i, r_{ci}, V_{swi} from the no-wall data respectively. There was a nominally 5% difference in the circulation values comparing the midspan and off center values. This was accounted for by day to day variability in the water tunnel freestream speed which showed a 4% peak to peak variation. The effect of

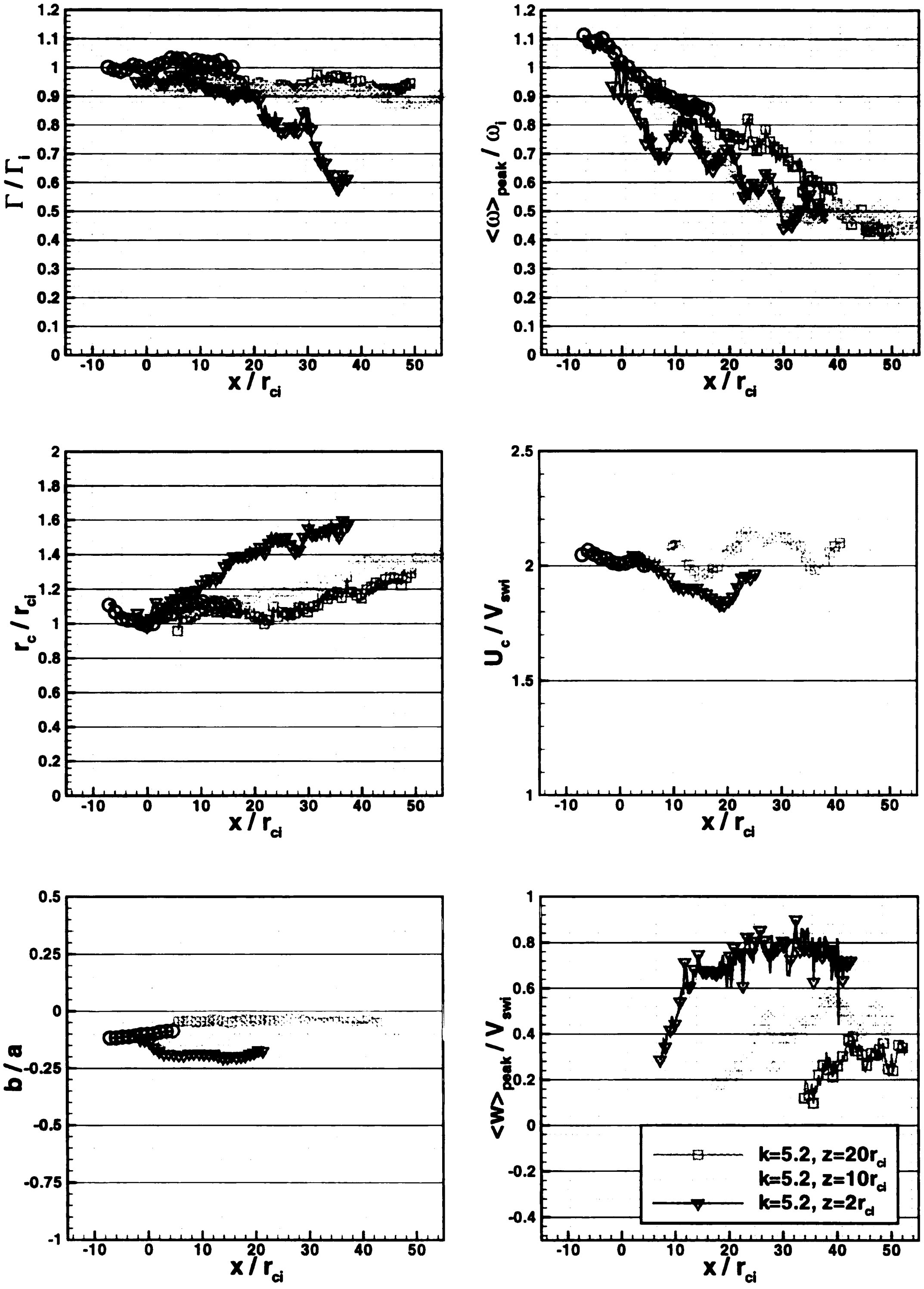

Figure 5-29: Vortex parameters (Γ, $<\omega>_{peak}$, r_c, U_c, $<w>_{peak}$, b/a) for multiple span locations. k=5.2. Symbols common.

free stream speed was to change the actual reduced frequency. Figure 3-29 shows the effect of reduced frequency on the circulation for the midspan data and indicated that the circulation will be lower for lower reduced frequencies. The circulation was nearly constant as a function of downstream distance for $z = 10r_{ci}$ and $20r_{ci}$. For $z = 2r_{ci}$ the circulation was initially constant, then decreased for $x > 20r_{ci}$. This decrease was caused by the expansion of the vortex, and vorticity leaving the circulation calculation radius.

The peak vorticity showed significantly different downstream characteristics depending upon the span location. At $z = 2r_{ci}$ the initial rate of decrease in $<\omega>_{peak}$ was higher than the no-wall decrease. Several local maximums in $<\omega>_{peak}$ were observed at $x = 12r_{ci}$, $20r_{ci}$, $27r_{ci}$, and $34r_{ci}$. There are two possible explanations for this phenomena. First, a variation in the vortex area (i.e. a vortex stretching effect) would increase or decrease the vorticity levels. There was no measurable change in the vortex core radius at the spatial locations of the local maximums of minimums which suggested this was not the cause. A second possible explanation was that the deformation and re-organization of the vortices created increases and decreases in the peak vorticity level. Given the dynamic break-up of the vortex observed at $z = 2r_{ci}$ (Figure 5-23) this seams to be a more plausible explanation. The $z = 10r_{ci}$ data indicated that peak vorticity initially followed the same decreasing rate of the midspan data. However for $x > 10r_{ci}$ the rate of decease was again higher until $x \approx 25r_{ci}$ after which $<\omega>_{peak}$ was nearly constant. At $z = 20r_{ci}$ $<\omega>_{peak}$ followed the midspan trends though the rate of decrease was higher for $x > 30r_{ci}$. Core radius measurements show that the core radius increases at all span locations with the rate of increase being higher closer to the wall. The vortex spacing ratio b/a was nominally constant at $z = 20r_{ci}$ and slightly increasing at $z = 10r_{ci}$. Recall that the vortex location was defined by the location of the centroid of the vorticity, which better accounts for vortices like those observed in Figure 5-24 at $z = 2r_{ci}$. At $z = 2r_{ci}$ the spacing first decreases then was nominally constant as the axial flow developed in the vortex core. The peak spanwise flow initially increased from zero. Small overshoots in $<w_{peak}>$ were observed after the axial flow was initiated at all three measurement locations. The highest spanwise flow was measured at $z = 2r_{ci}$.

The relative location of the centroid of the vorticity, x_c, and spanwise flow, x_w, is shown in Figure 5-30. This figure shows that the relative locations were within a core radius with a maximum difference observed at $z = 2r_{ci}$. The relative locations at $z = 10r_c$ were nearly zero for $x < 30r_{ci}$ after which the relative locations were no longer coincident, though to a lesser degree than was observed for $z = 2r_{ci}$. The relative locations were nearly zero for $z = 20r_{ci}$.

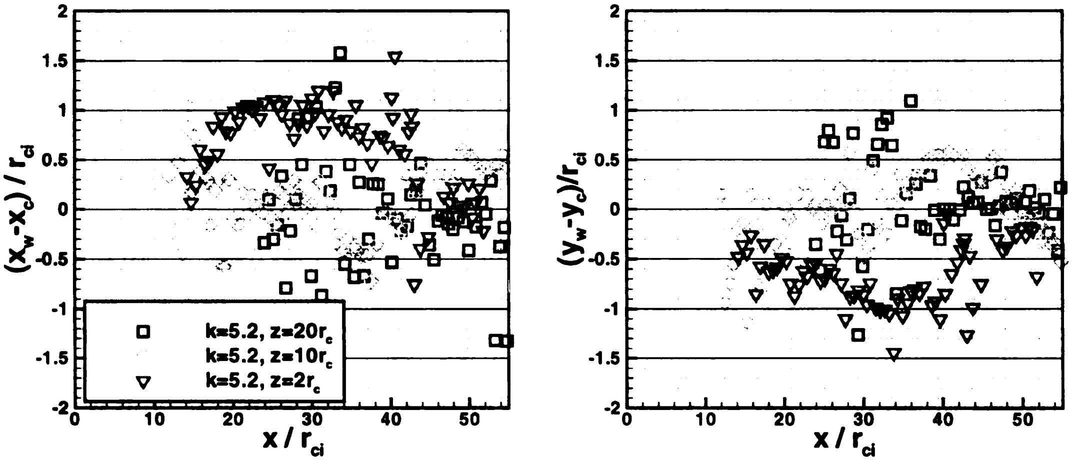

Figure 5-30: Relative location of the peak vorticity to the peak spanwise flow, k = 5.2.

5.2.3 Phase Averaged Flow Field, k=11.5.

Contour plots of the phase averaged peak vorticity, <ω>, and corresponding line profiles are shown in Figure 5-31 and Figure 5-32 respectively. At $z = r_{ci}$ and $2r_{ci}$ the vortices changed from Gaussian ($x < 0$), to non-Gaussian ($x > 0$) and then break-up into multiple regions of vorticity ($x > 15r_{ci}$). Further away from the wall at $z = 10r_{ci}$ and $20r_{ci}$ the vortices also change from Gaussian to non-Gaussian profiles with the break-up of the vortices was observed for the $z = r_{ci}$ and $2r_{ci}$, also observed further downstream for $z = 10r_{ci}$. The peak levels at $z = 20r_{ci}$ decreased with increasing downstream distance and the size of the vortices appeared to expand.

The spanwise flow field, <w>, is shown in contour form in Figure 5-33 with lines profiles in Figure 5-34. The structure change from isolated to "single band" for $z = r_{ci}$, $2r_{ci}$ and $10r_{ci}$. Of particular note is that the spanwise flow was nearly zero for $x > 48r_{ci}$ at $z = r_{ci}$. At $z = 20r_{ci}$ the spanwise flow enters the flow field with Gaussian like profiles, but change to multi-lobed profiles for $x > 30r_{ci}$. This may be a result of influence of the axial flow from the far cutting wall and the proximity to the midspan of the plane. Reverse spanwise flow was measured at all span locations except $z = 20r_{ci}$ with the highest levels close to the wall. The spanwise velocity profiles in Figure 5-34 showed good qualitative agreement with profiles from the line tagging experiments. An example is the velocity profile at $x = 19r_{ci}$ and $z = r_{ci}$ of Figure 5-34 compared to the near wall profile ($z = 0.6r_{ci}$) of Figure 5-3.

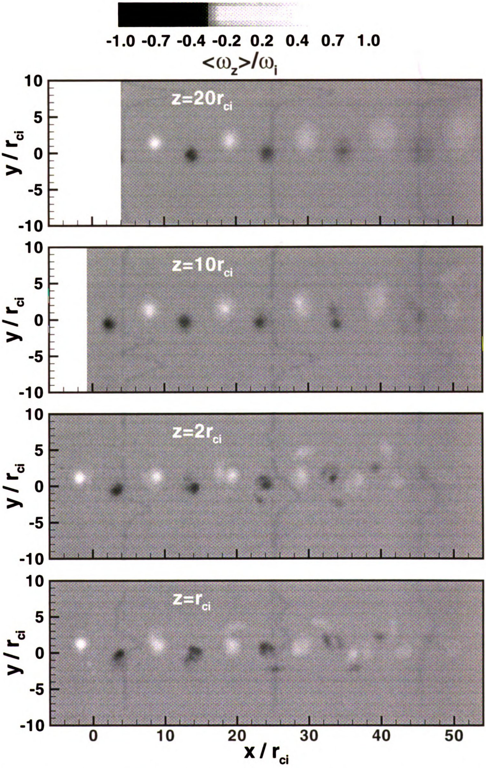

Figure 5-31: Phase-averaged vorticity, <ω>, for ϕ=0 at multiple span locations. k=11.5.

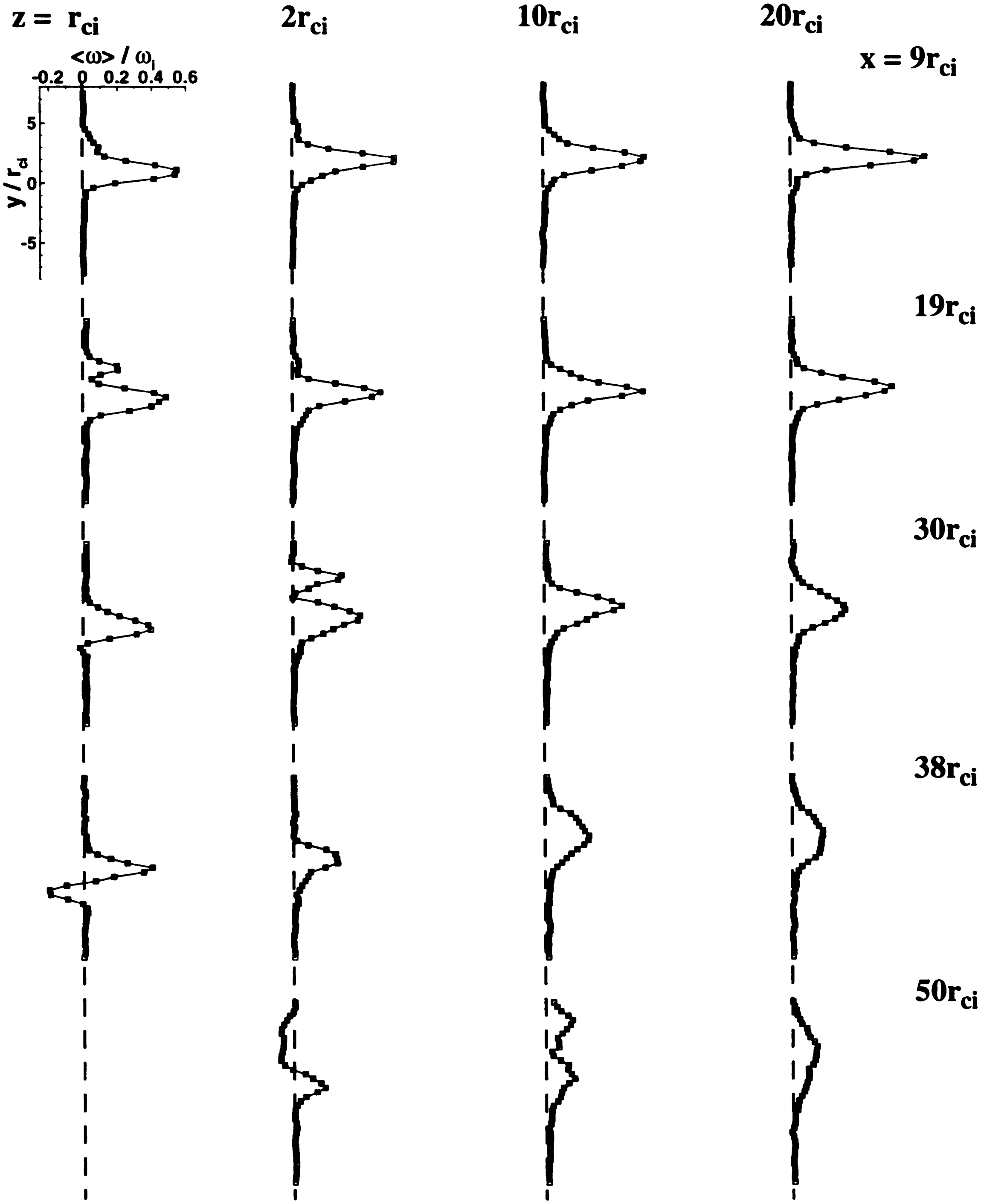

Figure 5-32: Phase-averaged vorticity, <ω>, profiles for k = 11.5. Dashed lines <ω> = 0. Spacing of profiles in figure not to scale.

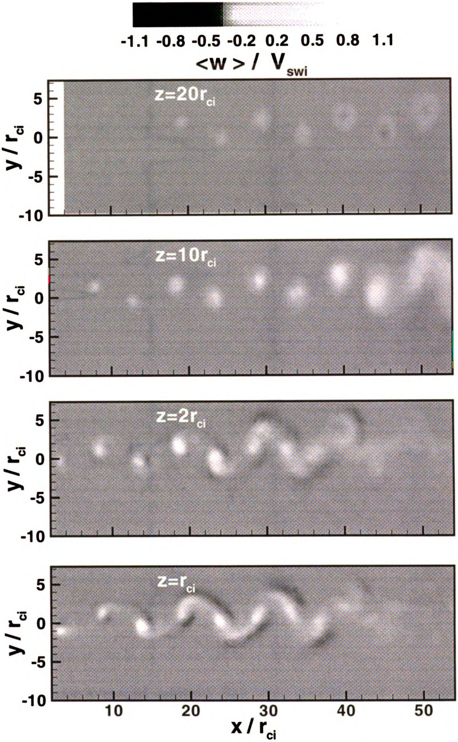

Figure 5-33: Phase-averaged spanwise velocity, <w>, for ϕ=0 at multiple span locations. k=11.5.

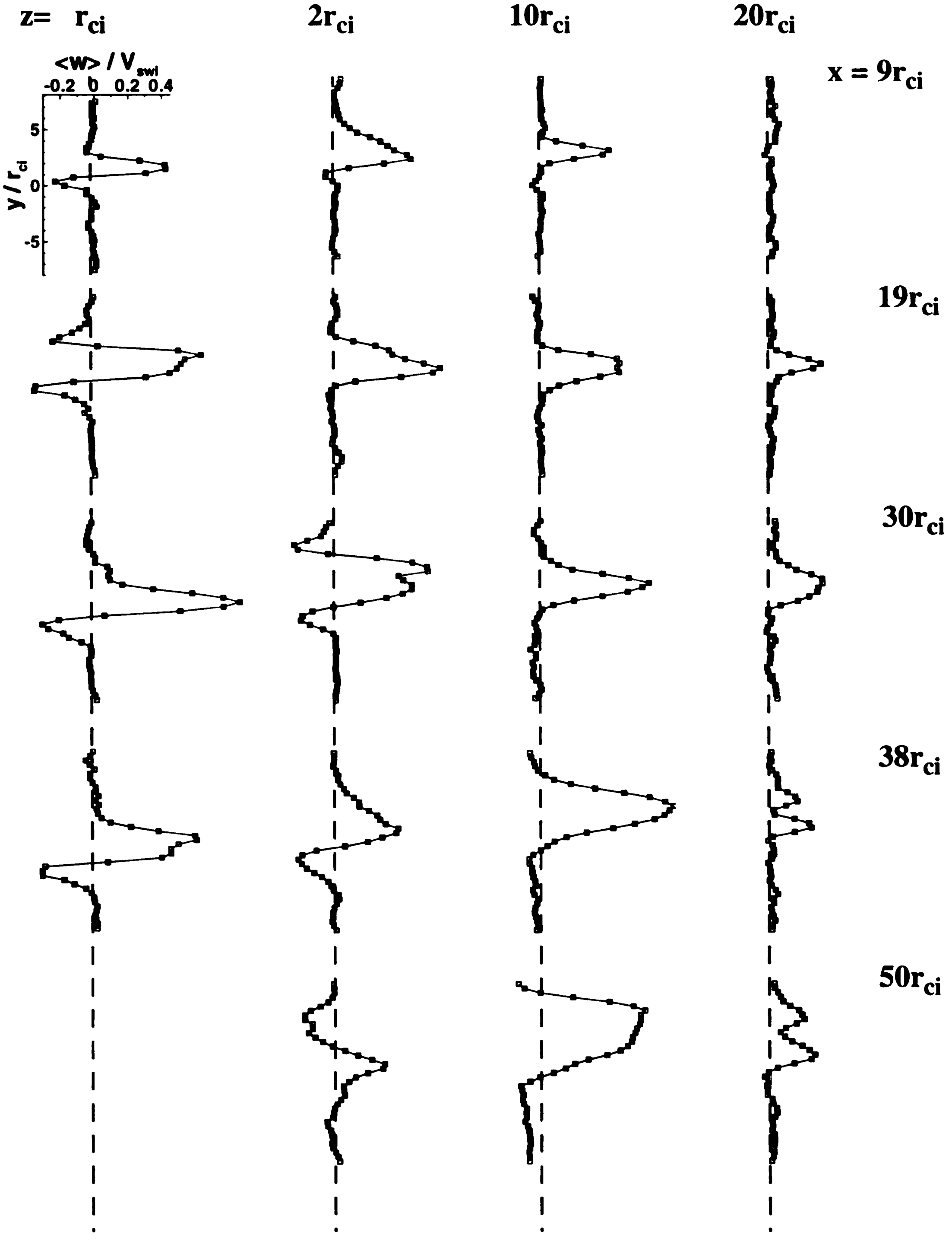

Figure 5-34: Phase averaged spanwise flow, <w>, profiles for k = 11.5. Dashed lines <w> = 0. Spacing of profiles in figure not to scale.

a
c
5
b
C
s
a
f
v

a
o
o
m
b
s
z

di
=
al
in

A comparison of the vortex parameters between the midspan no-wall experiments and near center span ($z = 20r_{ci}$) cutting wall experiments are shown in Figure 5-35. The data show good agreement between the data sets. The peak vorticity levels differ by about 5%. It was expected that the peak vorticity level would be smaller for the cutting wall data because the data density was slightly smaller in the cutting wall data sets. However, from Cohn and Koochesfahani (2000) this difference was expected to be less than 3%. It was shown in section 3.2.4 that vortex stretching due to a small spanwise flow gradient did affect the peak vorticity level significantly and it is possible that for this high reduced frequency case, the effects of the axial core flow were already apparent in the peak vorticity at this location.

The vortex parameters are shown in Figure 5-36. The normalization parameters are the same as used in the $k = 5.2$ discussion. The circulation data showed lower values of the circulation in the initial region (over-lapping with the midspan data) as was observed for the $k = 5.2$ case for the same reasons. The circulation decreased over the measurement extent for $z = 2r_{ci}$. The rapid decrease in circulation for $x > 20r_{ci}$ was caused by the break-up of the vortices into multiple structures, and the subsequent motion of the smaller structures away from the tracked largest structure. The break-up of the vortices at $z = 10r_c$ was indicated by the decrease in circulation for $x > 35\ r_{ci}$.

Peak phase averaged streamwise vorticity decreased with increasing downstream distance at all span locations. The peak vorticity showed local maximums, or spikes, for $z = 2r_{ci}$ as was observed for the $k = 5.2$ case, however, for this reduced frequency there were also local peaks for $z = 10r_{ci}$ and $20r_{ci}$ span locations. Discussion on this point to follows in the next paragraph. The local vortex core radius, r_c, increased with increasing

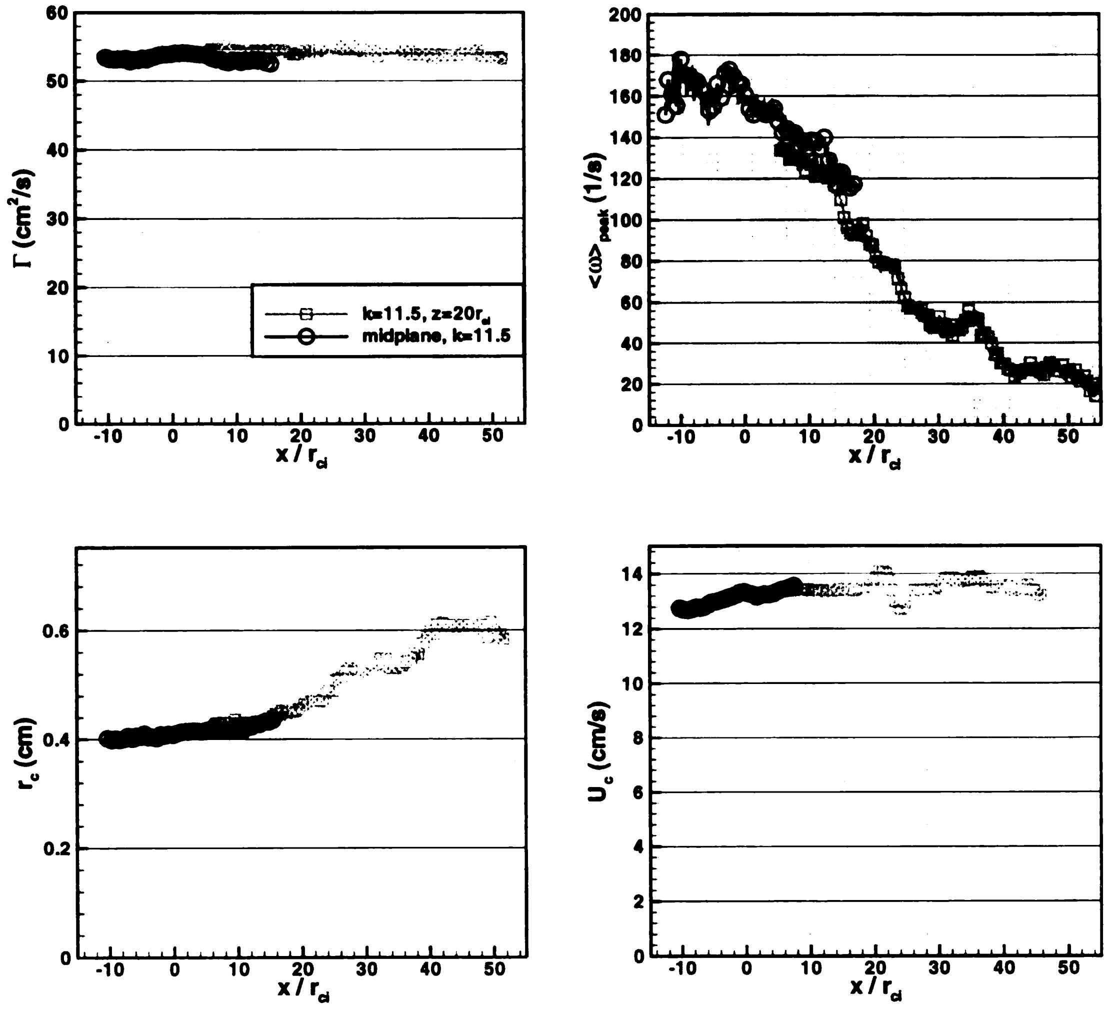

Figure 5-35: Comparison of vortex parameters (Γ, $\langle\omega\rangle_{peak}$, r_c, U_c) from no-wall midspan data and cutting wall, z = $20r_{ci}$ (near midspan) data. k = 11.5. Symbols common.

downstream distance with the rate of increase higher closer to the wall. The drop in the core radius for $z = 2r_{ci}$ at $x = 15r_{ci}$ was caused by the break-up of the vortex into multiple structures as noted for the circulation recalling the core radius was calculated using (16).

The spacing ratio b/a showed an initial roughly constant region for all three span locations. At $x = 15r_{ci}$ b/a decreased and eventually changed sign for the $z = 2r_{ci}$ measurement plane. This sign change indicated a change in origin of the vortex array,

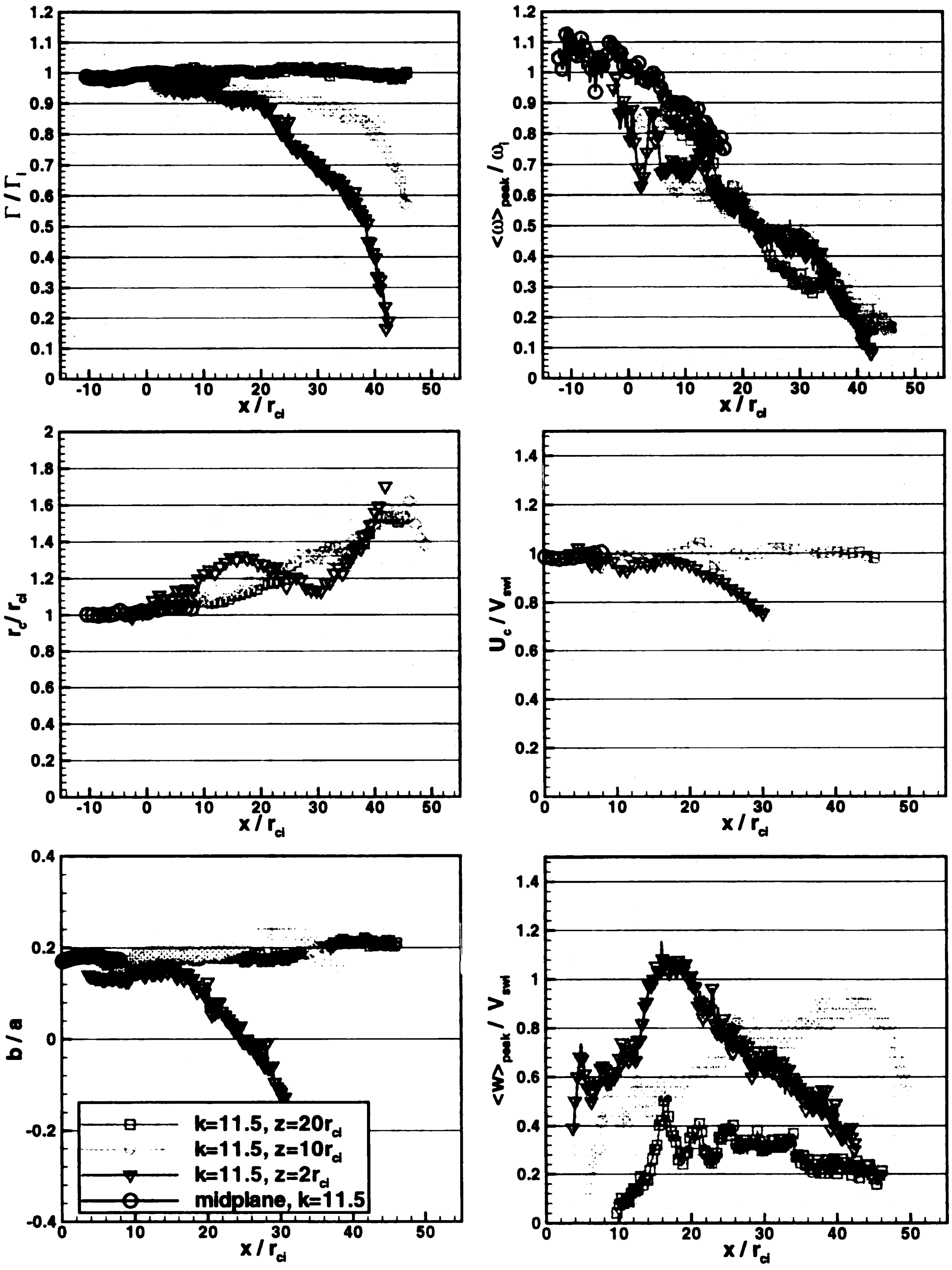

Figure 5-36: Vortex parameters (Γ, $\langle\omega\rangle_{peak}$, r_c, U_c, $\langle w\rangle_{peak}$, b/a) for multiple span locations. k = 11.5. Symbols common.

switching from a velocity excess to a velocity deficit consistent with the $\bar{u}$ and $\bar{\omega}$ data in section 5.2.1. Careful observation of the phase resolved data in Figure 5-31 also show this trend. Further from the wall for $z = 10r_{ci}$ the vortex array orientation switch was initiated at $x = 35r_{ci}$ indicating that further downstream the array would also change orientation. The peak spanwise velocity showed the characteristic overshoot in $\langle w \rangle_{peak}$ as the spanwise flow was initiated. The highest level was measured at $z = 2r_{ci}$, though the levels were still increasing for $z = 10r_{ci}$.

The local spikes in $\langle \omega \rangle_{peak}$ are show in Figure 5-37 for $z = 2r_{ci}$ and $10r_{ci}$. Two local spikes (indicated by the arrows pointing to solid lines solid lines) were observed at both span locations. A weaker spike (indicated by the arrows pointing to the dashed lines) was also observed. These data indicated the local vorticity spikes were not isolated

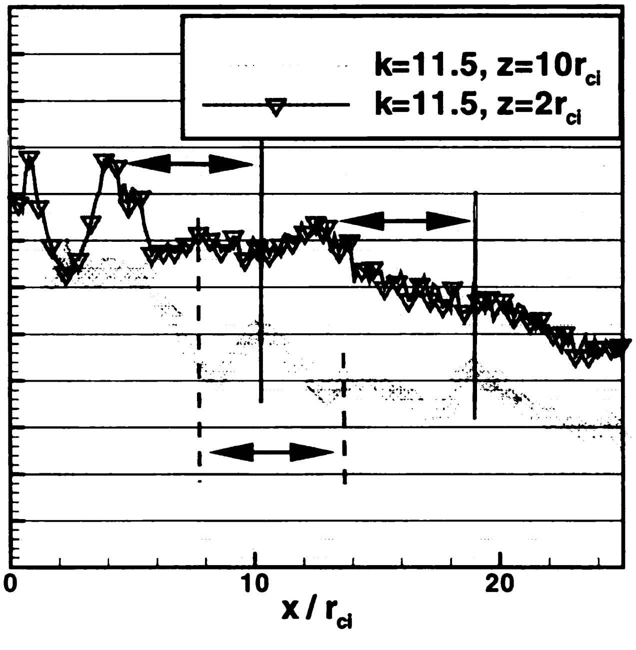

Figure 5-37: Peak vorticity, $\langle \omega \rangle_{peak}$, as a function of downstream distance for k = 11.5. Curves shown are vertically offset to allow simultaneous viewing.

incidents but events that convected away from the wall through multiple measurement planes.

Figure 5-38 shows r_c, $<w>_{peak}$ and U_c plotted on the same figure along with $<\omega>_{peak}$ for $z = 2r_{ci}$, $10r_{ci}$ and $20r_{ci}$. The vertical axis of the curves are offset to allow the curves to be displayed on the same figure without significant overlapping. At $z = 2r_{ci}$ the first local minimum in the peak vorticity (solid line) corresponds to an increased vortex area, the characteristic spike in the spanwise flow velocity, and a decrease in the convection speed. The following spike in the vorticity (dashed line) correlated spatially with the undershoot in the spanwise flow, a decrease in the vortex area and a positive spike in the convection speed. The correlation for the subsequent vorticity spikes was less clear, however, at $z = 10r_{ci}$ the spatial correlation was evident for the first three vorticity spikes. The vortex core radius was least likely to show correlated local maximums and minimums. The core radius variation for the first local peak was relatively small, 4% or 0.02 cm. This level was significant, but near to the noise level in the radius estimation. The subsequent vorticity peaks were less intense, and the corresponding area change was also less making it more difficult to observe. At $z = 20r_{ci}$ the correlation between the vorticity and spanwise velocity was clear for the first two vorticity spikes. A surge in the convection speed appeared to lag spatially behind the initial vorticity and spanwise flow spikes. No change in the vortex core radius could be reliably detected at this span location.

The relative spatial locations of the vortex core (defined by the centroid of the vorticity) and $<w>_{peak}$ is shown in Figure 5-39. The locations were initially coincident, but separated as the downstream distance was increased. There were small oscillations in

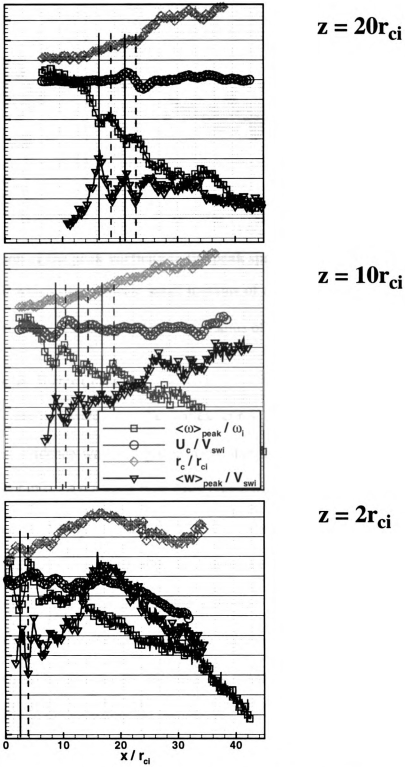

Figure 5-38: Spatial correlation of initial local vorticity peak to r_c, U_c, $<w>_{peak}$, k=11.5. Vertical major grids are 0.1 apart. Magnitudes for the vertical axis can be found on Figure 5-36.

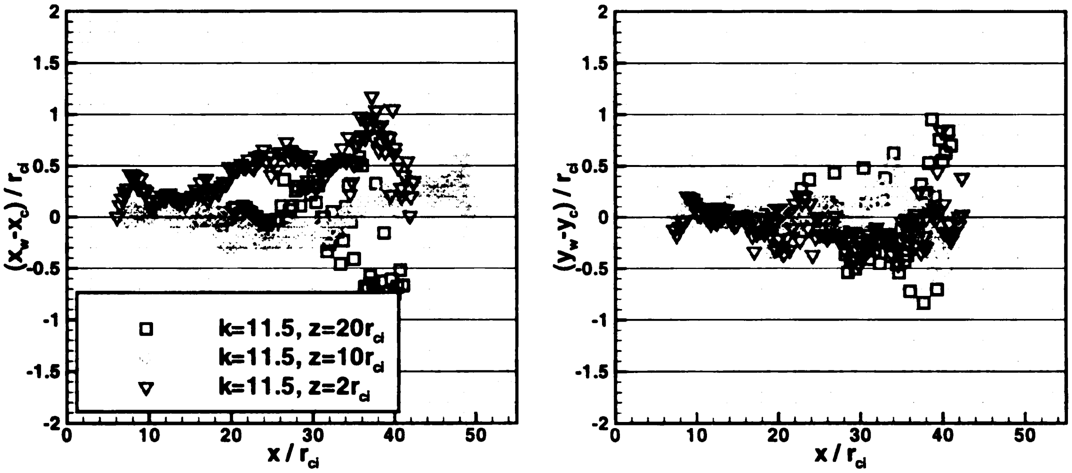

Figure 5-39: Relative location of the peak vorticity to the peak spanwise flow, k=11.5.

the spatial location observed which may indicate small motions of the axial flow within the vortex core though the locations remained within a core radius of each other.

5.2.4 Area Varying Waves on the Vortex Cores

Evidence for area varying waves on the vortex cores has been presented throughout this chapter. This evidence was first given in the line tagging data with the spanwise velocity spikes that followed the axial flow front boundary. These data showed waves were present for all reduced frequency cases except the lowest (A = 2°, k = 4.1). The trends in the wave speed were consistent with the calculated equivalent speed of sound. The more detailed stereoscopic data showed the spanwise velocity spikes were correlated to spikes in the peak vorticity and a change in the vortex core radius of 5% for the high k case. The low reduced frequency case did not show evidence of area variation or spikes in the vorticity to within the measurement resolution.

As already discussed, Lundgren and Ashurst (1989) presented equations for area varying waves on a vortex core that were analogous to the gas dynamics equations. In that work, the wave propagation speed, V_w, was defined as:

$$V_w = w_1 + c_e\left(\ln\frac{A_2}{A_1}\right)(1 + A_1/A_2)^{-\frac{1}{2}} \tag{20}$$

where w_1 is the velocity in front of the wave relative to the velocity behind the wave (i.e. the velocity change across the wave). A_1 and A_2 are the vortex areas downstream and upstream of the wave. For small disturbances $A_1 \approx A_2$ and equation (20) simplifies to:

$$V_w = w_1 + c_e \tag{21}$$

where c_e is the previously defined "equivalent speed of sound". In the limit of no axial flow upstream of the wave $w_1 = 0$ and $V_w = c_e$. The low reduced frequency case was consistent with this equation (i.e. there was no change in the vortex area observed and the wave speed was approximately equal to the equivalent sound speed).

The high reduced frequency case, $k = 11.5$, showed an area variation of nominally 5%. The wave speed was calculated using (20) by substituting experimental values for the area ratio, speed of sound, and relative upstream axial flow velocity. For the high reduced frequency case $c_e = 15.1$ cm/s, $A_1/A_2 = 0.95$ and $w_1 = 0.65$ cm/s. Using (20) $V_w = 16.16$ which compares well to the $V_w = 15.95$ (from the line tagging data) and $V_w = 16.4$ (from the stereoscopic data). The analytic work does, therefore, appear to describe the experimental data to first order.

The high reduced frequency data also showed a correlation between the area varying waves and a change in the vortex convection speed, U_c. In this work U_c was calculated by differentiating the downstream vortex core location versus time. A local maximum (or minimum) in the convection speed is also the same as a local surge (or lag) in the downstream location of the vortex core. Maxworthy et al. (1983) indicates that an area varying wave with area ratio greater than 20% will cause an unstable helical or spiral disturbance behind the wave to be generated. For smaller area ratios a series of decreasing amplitude waves will exist. For k = 11.5 (area ratio of 5% rather than 20%), the first primary wave was followed by a series of smaller amplitude disturbances consistent with the results of Maxworthy et al. (1983). The line tagging data, for cases with waves, and stereoscopic data, high k case, also appeared to have smaller axial flow spikes (i.e. waves) behind the initial wave consistent with the Maxworthy et al. (1983) conclusions. Additionally, a small amplitude displacement, evidenced by the local maximums and minimums in the convection speed, was generated. This kink in the vortex is consistent with schematics of axisymmetric waves in Maxworthy et al. (1983) and may be the precursor to the unstable waves discussed.

Chapter 6

CONCLUSIONS

In this work the velocity and vorticity fields in the wake of an oscillating NACA-0012 airfoil were measured with the goal of better understanding the development of a vortex array with and without axial flow, as well as the characteristics of the axial flow if present. Molecular tagging techniques were the primary experimental tool for this purpose.

Planar MTV was used to detail the flow field (from which the vorticity field was calculated) at the tunnel midspan, from the trailing edge of the airfoil through the first chord of development. Cutting walls were placed into the flow field half a chord downstream of the trailing edge of the airfoil to initiate spanwise flow within the core of the vortices (axial core flow). Single and multiple line tagging experiments were performed to detail the spanwise flow with and without cutting walls. Stereoscopic MTV was developed and used for the first time in this work. This technique allowed the complete velocity vector, in the plane of the laser sheet, to be measured which in turn allowed the axial core flow and vorticity field to be measured simultaneously.

Results from the planar midspan data without cutting walls showed several interesting features. The unsteady Kutta condition was found to not be valid for high reduced frequencies in this flow field. Reverse flow along the surface of the airfoil was observed using molecularly based flow visualization techniques. The vortex array switched vertical spatial orientation with increasing reduced frequency indicating a switch from mean drag to mean thrust for the oscillating airfoil. Mean force calculations from the data show that the use of the mean streamwise velocity field overestimated the mean thrust force. The vortices in the array were aligned for $k \approx 6$, which would signify a zero net thrust/drag using the mean profile only. The zero net thrust case was found to exist for $k \approx 8$ using a more complete calculation of the thrust force developed from the Navier-Stokes equations.

The formation and development of the vortex array was governed, in part, by the reduced frequency. For $k = 4.2$ the boundary layer vorticity left the trailing edge of the airfoil and then formed isolated vortices downstream. For $k > 5$ the vortices were formed at, and possibly upstream of the airfoil trailing edge. Fluid from one surface was transported to the other surface during the formation process. The peak vorticity, circulation, and convection speed were functions of the reduced frequency and airfoil peak oscillation amplitude while the vortex core radius was nominally a function of angle of attack only.

Results of the line tagging data without cutting walls showed that spanwise flow was generated because of the vortex / tunnel side-wall interaction. The magnitude of the spanwise velocity was on the order of the swirl velocity. The spanwise flow was initially distributed in two isolated structures for each phase. The structure changed into a single band of spanwise flow through the entire phase for moderate to high reduced frequencies. No transition from multiple to single structures was observed for the lower reduced frequency cases.

Line tagging data were also taken for the cutting wall case. These data showed that the axial flow from the vortex cutting wall interaction propagates away from the cutting walls. Area varying waves were also present near the axial flow front and were also found to propagate away from the cutting walls. The speed of the area varying waves was found to be slower than the front speed indicating the area varying waves increasingly lag the front boundary. The span location of the highest spanwise flow at given downstream distance was found to move away from the wall with increasing downstream distance. The peak spanwise velocity showed an overshoot after the front passed. Reverse spanwise flow was measured for all reduced frequency cases investigated. The structure change observed for the no-wall case was also observed for the cutting wall case.

Two reduced frequency cases, k = 5.2 and 11.5, were investigated using stereoscopic MTV. These data revealed many details of the flow field with the cutting walls. The mean streamwise flow field was found to change from a velocity excess to a velocity deficit for increasing downstream distance in the wake for the high reduced frequency case. The structure of the vortices near the wall broke up into multiple regions of vorticity with the profile becoming non-Gaussian and asymmetric. Hollow vorticity profiles were found for several conditions, though the evolution from Gaussian to hollow was not a result of decreasing peak vorticity, but a distortion and re-distribution of the vorticity. Further away from the wall the vortices remained somewhat Gaussian with a decreasing peak level.

Spanwise flow in the core of the vortices was observed with reverse spanwise flow measured outside of the vortex core. The distribution of the spanwise flow within the vortex core was significantly different depending upon the span location and varied from Gaussian like, to multi-lobed, to non-specific. The transition of the axial flow structure from isolated to band like, as was noted in the line tagging data, was also observed in the sMTV data for the high reduced frequency cases. The sMTV data showed that this change in structure occurred over the same region as the break-up of the vortices was observed. Spikes in the peak vorticity were observed to move away from the cutting walls as the vortices convected downstream. These spikes appeared to be well correlated to spikes in the peak spanwise core flow and the convection speed which also moved away from the cutting walls. A change in the vortex core radius accompanied the first spike in the peak vorticity for the highest reduced frequency cases indicating that an area varying wave was initiated along with the axial core flow. A characteristic signature of the initiation of axial flow within the vortex core was found to be a local decrease, followed by increase, in the vortex core convection speed.

Chapter 7

REFERENCES

Anderson, J.M., Streitlien, K., Barrett, D.S., Triantafyllou, M.S., "Oscillating Foils of High Propulsive Efficiency", *Journal of Fluid Mechanics*, vol 360, pp. 41-72, 1998.

Bödewadt, U.T., Die Drehströmung Uber Festem Grund, *ZAMM*, Vol. 20, 1941

Burggraf, O.R., Stewartson, K., Belcher, R., "Boundary Layer Induced by a Potential Vortex", *Physics of Fluids*, Vol. 14, No. 9, pp.1821-1833, 1971.

Cohn, R,K, *Effects of Forcing on the Vorticity Field in a Confined Wake*, Ph.D. Dissertation, Michigan State University, 1999.

Cohn, R., Koochesfahani, M., "Effect of Boundary Conditions on Axial Flow in a Concentrated Vortex Core", *Physics of Fluids A*, Vol.5 No.1, pp.280-282, January 1993.

Cohn, R., Koochesfahani, M., "The Accuracy of Mapping Irregular Spaced Velocity Data onto a Regular Grid and the Calculation of Vorticity", *Experiments in Fluids*, S61-S69, 2000.

Conlisk, A.T., "Modern Helicopter Aerodynamics", *Annual Review of Fluid Mechanics*, Vol.29, pp. 515-567, 1997.

Donaldson, C., *Solutions of the Navier-Stokes Equations for Two and Three Dimensional Vortices*, Ph.D. Dissertation, 1956.

Donaldson, C., Sullivan, R., "Examination of the Solutions of the Navier-Stoke Equations for a Class of Three-Dimensional Vortices Part I: Velocity Distributions for Steady Motion", *AFOSR TN 60-1227*, 1960.

Gendrich, C.P., *Dynamic Stall of Rapidly Pitching Airfoils: MTV Experiments and Navier-Stokes Simulations*, Ph.D. Dissertation, Michigan State University, 1999.

Gendrich, C.P., and Koochesfahani, M.M., "A Spatial Correlation Technique for Estimating Velocity Fields Using Molecular Tagging Velocimetry (MTV)", *Exp. Fluids*, vol. 22, 1996, pp. 67-77.

Gendrich, C.P., Koochesfahani, M.M., and Nocera, D.G., "Molecular Tagging Velocimetry and Other Novel Applications of a New Phosphorescent Supramolecule", *Exp. Fluids*, vol. 23, 1997, pp. 361-372.

Giesing, J. P., "Vorticity and Kutta Condition for Unsteady Multi-energy Flow," *Transactions of ASME, Journal of Applied Mechanics*, Vol. 36, pp. 608-613, 1969.

Hagen, J., Kirosaka, M., "Corewise Transport in Hairpin Vortices- The 'Tornado Effect'", *Physics of Fluids A*, Vol.5 No.12, pp.3167-3174, 1993.

Hassan, A.A, Tung, C., Sankar, L.N., "Euler Solution for Self-Generated Rotor Blade-Vortex Interactions", *International Journal for Numerical Methods in Fluids*, Vol. 15, pp. 427-452, 1992.

Hill, R.B., Klewicki, J.C., "Data Reduction Methods for Flow Tagging Velocity Measurements", *Experiments in Fluids*, Vol. 20, pp.142-152, 1996.

Hirsa, A., Lopez, J.M., Kim, S., "Evolution of Initially Columnar Vortex Terminating Normal to a No-Slip Wall", *Experiments in Fluids*, Vol.29, pp.309-321, 2000.

Kármán, T. von, "Über Laminare und Turbulente Reibung, *ZAMM*, Vol. 1, pp. 233-252, 1921.

Katz, J., Weihs, D., "Wake Rollup and the Kutta Condition for Airfoils Oscillating at High Frequency", *AIAA Journal*, Vol. 19, No. 12, pp. 1604-1606, 1981.

Khalid, A., "Pressure and Drag Force Determination on an Oscillating Airfoil Submerged in Fluid", Masters Project Research Report, Michigan State University, 2001.

Koochesfahani M.M., "Molecular Tagging Velocimetry (MTV): Progress and Applications", 30th AIAA Fluid Dynamics Conference AIAA99-3786, June 28 - July 1, Norfolk, Virginia, 1999.

Koochesfahani, M.M., "Vortical Flow in the Wake of a Pitching Airfoil", International Conference on Engineering Applications of Mechanics, June 1992.

Koochesfahani, M.M., "Vortical Patterns in the Wake of an Oscillating Airfoil", *AIAA Journal*, Vol.27, No.9, pp. 1200-1205, Sept. 1989.

Koochesfahani M.M., Cohn, R.K., Gendrich, C.P., Nocera, D.G. "Molecular Tagging Diagnostics for the Study of Kinematics and Mixing in Liquid Phase Flows", *Proceeding of the Eighth International Symposium on Applications of Laser Techniques in Fluid Mechanics*, July 8-11, 1996, Lisbon, Portugal

Kotidis, P.A., "Unsteady Radial Transport in a Transonic Compressor Stage", *MIT Gas Turbine Lab Report #199*, September, 1989.

Kuo, H.L., "Axisymmetric Flows in the Boundary Layer of a Maintained Vortex", *Journal of the Atmospheric Sciences*, Vol. 28, pp.20-41, January, 1971.

Krishnamoorthy, S., and Marshall, J., "An Experimental Investigation of 'Vortex Shocks'", *Physics of Fluids*, Vol. 6, No. 11, pp. 3737-3741, 1994

Laursen, T.S., Rasmussen, J.J., Stenum, B., Snezhkin, E.N., "Formation of a 2D Vortex Pair and its 3D Breakup: an Experimental Study", *Experiments in Fluids*, Vol.23, pp.29-37, 1997.

Lighthill, J., *Mathematical Biofluiddynamics*, SIAM, Philadelphia, 1975.

Lopez, J.M., "Axisymmetric Vortex Breakdown Part 1. Confined Swirling Flows", *Journal of Fluid Mechanics*, Vol. 221, pp.553-576, 1990.

Lundgren, T.S., Ashurst, W.T., "Area-varying Waves on Curved Vortex Tubes with Application to Vortex Breakdown", *Journal of Fluid Mechanics*, Vol. 200, pp. 283-307, 1989.

Marshall, J., Krishnamoorthy, S., "On the Instantaneous Cutting of a Columnar Vortex With Non-Zero Axial Flow", *Journal of Fluid Mechanics*, 1997.

Marshall, J., Yalamanchili, R., "Vortex Cutting by a Blade, Part II: Computations of Vortex Response", *AIAA Journal*, Vol. 32, No. 7, pp.1428-1436, 1994.

Maskell, E. C., "On the Kutta-Joukowski Condition in Two-Dimensional Unsteady Flow," unpublished note, Royal Aircraft Establishment, Farnborough, England, 1972.

Maxworthy, T., "On the Structure of Concentrated, Columnar Vortices", *Astronautica Acta*, Vol. 17, pp. 363-374, 1972.

Maxworthy, T., "A Vorticity Source for Large-Scale Dust Devils and Other Comments on Naturally Occurring Columnar Vortices", *Journal of Atmospheric Sciences*, Vol.30, pp.1717-1722, 1973.

Maxworthy, T., Mory, M., Hopfinger, E.J., "Waves on Vortex Cores and Their relation to Vortex Breakdown", *AGARD CPP-342*, paper 29, 1983.

McCrosky, W. J., "Unsteady airfoils," *Annual Review of Fluid Mechanics*, Vol. 14, pp. 285-311, 1982.

Platzer, M., Neace, K., "Aerodynamic Analysis of Flapping Wing Propulsion", *AIAA Paper 93-0484*, 1993.

Poling, D.R., Telionis, D.P., "The Response of Airfoils to Periodic Disturbances- The Unsteady Kutta Condition", AIAA Journal, Vol. 24, No. 2, pp. 193-199, 1986.

Rockwell, D., "Vortex Body Interactions", *Annual Review of Fluid Mechanics*, 1998.

Rott, N., Lewellen, W.S., "Boundary Layers and Their Interactions in Rotating Flows", *Progress in Aeronautical Sciences*, Pergamon Press, Vol. 7, pp.111, 1966.

Schlichting, H., *Boundary Layer Theory*, McGraw-Hill Book Company, 1960.

Solof, S.M., Adrian, R.J., and Liu, Z-C, "Distortion Compensation for Generalized Stereoscopic Particle Image Velocimetry", *Measurement and Science Technology*, 8, 1997, pp.1441-1454.

Stanek, M. J. and Visbal, M. R., "Study of the Vortical Wake Patterns of an Oscillating Airfoil," *AIAA Paper No. AIAA-89-0554*, 1989.

Streitlien, K., Triantafyllou G.S., "On Thrust Estimates For Flapping Airfoils", *Journal of Fluids and Structures*, Vol. 12, pp. 47-55, 1998.

Wan, C.A., Chang, C.C., "Measurement of the Velocity Field in a Simulated Tornado Like Vortex Using a Three Dimensional Velocity Probe", *Journal of the Atmospheric Sciences*, Vol. 29, pp.116-127, January 1972.

Westerweel J., and Nieuwstadt F.T., "Performance Tests on 3-Dimensional Velocity Measurements with a Two Camera Digital Particle Image Velocimeter", *Laser Anemometry*, Vol. 1, 1991, pp.349-355.

Wiegand, A., *The Response of a Vortex Ring to a Transient Cut*, Ph.D. Dissertation, University of California Sandiego, 1993.

Wilder, M.C., Mathioulakis, D.S., Poling, D.R., Telionis, D.P., "The Formation and Internal Structure of Coherent Vortices in the Wake of a Pitching Airfoil", *Journal of Fluids and Structures*, Vol. 10, 1996, pp.3-20.

APPENDIX A

MEAN FORCE EQUATION DEVELOPMENT

Given a submerged body in a flow field, determine an equation that can be used to calculate the mean force from the velocity field. For this analysis the flow is assumed to be incompressible, 2-D, and steady in the mean. Figure A.1 shows the control volume used for the following formulation. The integral linear momentum equation can be written as:

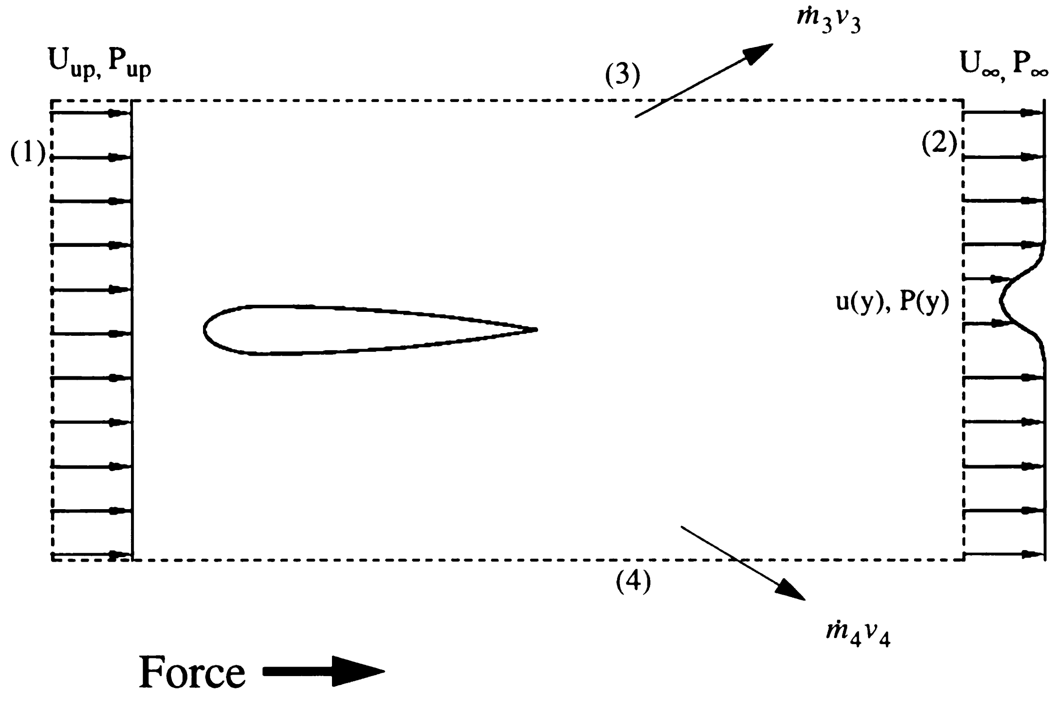

Figure A-1: Airfoil mean drag formulation control volume.

$$\frac{\partial}{\partial t}\int_{CV} \vec{V}\rho dV + \int_{CS} \vec{V}\rho(\vec{V}\cdot\hat{n})dA = \sum F \qquad \text{(A1)}$$

For this problem the x-component is considered and the forces are composed of the drag force and the pressure forces on the control surfaces:

$$\sum F_x = D + \int_{CS} P ds \qquad \text{(A2)}$$

Consider first the left hand side of (A1). If the flow is steady (i.e. the mean flow is not changing with time), the first term in (A1) is zero. The second term can be expanded to for the four control surfaces indicated as:

$$\int_{CS} \vec{V}\rho(\vec{V}\cdot\hat{n})dA = \int_1 U_{up}^2 \rho dA_1 - \int_2 u^2(y)\rho dA_2 - \int_3 U_3 \rho V_3 dA_3 - \int_4 U_4 \rho V_4 dA_4 \qquad \text{(A3)}$$

Assume that U_{up}, U_3, V_3, U_4, V_4 are constants and that $V_3 = -V_4$, $U_3 = U_4$. The mass flux across the top and bottom surfaces is defined as

$$\dot{m}_3 = \rho V_3 A_3 \qquad \text{(A4)}$$

$$\dot{m}_4 = \rho V_4 A_4 \qquad \text{(A5)}$$

The mass flux across the upstream and downstream surfaces is defined as:

$$\dot{m}_1 = \int_1 \rho b U_{up} dy \qquad \text{(A6)}$$

$$\dot{m}_2 = \int_2 \rho b u(y) dy \qquad \text{(A7)}$$

Since the flow is assumed to be 2-D, the span length may be removed from the areas and differential areas. The conservation of mass for this control volume indicates that

$$\dot{m}_1 = \dot{m}_2 + \dot{m}_3 + \dot{m}_4 \qquad \text{(A8)}$$

Combining (A4)-(A8) and (A3) and simplifying yields:

$$\int_{CS} \vec{V}\rho(\vec{V}\cdot\hat{n})dA = \rho b\left(\int_{1} U_{up}^{2}dy - \int_{2} U^{2}(y)dy + \left(-\int_{1} U_{up}dy - \int_{2} u(y)dy\right)U_{3}\right) \tag{A9}$$

It is further assumed that $U_3 \approx U_{up}$, therefore

$$\int_{CS} \vec{V}\rho(\vec{V}\cdot\hat{n})dA = \rho b\left(\int_{2} U_{up}u(y)dy - \int_{2} u^{2}(y)dy\right) = D_{TM} \tag{A10}$$

Equation (A10) is important in that if $U_{up} = U_{\infty}$ and the contribution from the fluctuating velocities are not important (A10) is the force as noted. The force coefficient is

$$C_{FM} = \frac{2}{c}\int\left(\frac{u(y)}{U_{up}}\right)\left(\frac{u(y)}{U_{up}} - 1\right)dy \tag{A11}$$

With the current data set, the 2-D flow field is know. The mean and RMS quantities for U and V can be calculated and used to formulate a more complete thrust coefficient. Let the velocity be broken into a mean and fluctuating portion as:

$$u(t)=(\bar{u}+u') \tag{A12}$$

The fluctuating quantities enter into the drag formula via (A10) (u_{RMS}) and the pressure in (A2) (v_{RMS}). Consider first the effects of u_{RMS}. Substituting (A12) into the RHS of (A10) and taking the average yields

$$\int_{CS} \vec{V}\rho(\vec{V}\cdot\hat{n})dA = \rho b\left(\int_{2} U_{up}u(y)dy - \int_{2} u^{2}(y)dy - \int_{2} u_{RMS}^{2}(y)dy\right) \tag{A13}$$

The vertical pressure distribution, P(y) is composed of the hydrostatic pressure distribution plus the dynamic pressure. Since the hydrostatic pressure distribution is the same for surfaces (1) and (2) it is neglected in the following analysis. Using the y-component Navier-Stokes (N-S) equations a formula the y-pressure distribution can be found. The y component N-S can be written as:

$$\frac{\partial v}{\partial t}+u\frac{\partial v}{\partial x}+v\frac{\partial v}{\partial y}+w\frac{\partial v}{\partial z} = -\frac{1}{\rho}\frac{\partial P}{\partial y}+\upsilon\left(\frac{d^2v}{dx^2}+\frac{d^2v}{dy^2}+\frac{d^2v}{dz^2}\right) \tag{A14}$$

It was shown in Khalid (2001) that contributions from the x derivatives are small. The flow is assumed to be 2-D and steady which simplifies (A14) to:

$$v\frac{\partial v}{\partial y} = -\frac{1}{\rho}\frac{\partial P}{\partial y}+\nu\left(\frac{d^2v}{dy^2}\right) \tag{A15}$$

Let $v(t)=(\bar{v}+v')$ and substituting into (A15) yields:

$$\frac{\partial}{\partial y}(\bar{v}^2+2\bar{v}v'+v'^2) = -\frac{1}{\rho}\frac{\partial P}{\partial y}+\nu\left(\frac{\partial^2}{\partial y^2}\bar{v}+\frac{\partial^2}{\partial y^2}v'\right) \tag{A16}$$

The mean of (A16) is

$$\frac{\partial P}{\partial y} = \mu\frac{\partial^2}{\partial y^2}\bar{v}-\rho\frac{\partial}{\partial y}(\bar{v}^2+v_{RMS}^2) \tag{A17}$$

Since $\bar{v} \approx 0$, the (A17) reduces to

$$\frac{\partial P}{\partial y} = -\rho\frac{\partial}{\partial y}(v_{RMS}^2) \tag{A18}$$

Integration of (A18) gives the pressure distribution in the y-direction on surfaces (1) and (2) of the control volume. For surface (1) v_{RMS} is small so that $P \approx$ const. Integration of (A18) from the freestream to an arbitrary y location on surface (2) yields:

$$P(y)-P_\infty = -\rho(v_{RMS}^2(y)-v_{RMS,\infty}^2) \tag{A19}$$

Assuming that the freestream RMS level is small the pressure distribution is:

$$P(y) = P_\infty-\rho v_{RMS}^2(y) \tag{A20}$$

Equation (A20) can be substituted into (A2) and (A10) to get

$$D_{FP} = \rho b\left(\int_2 U_{up}u(y)dy - \int_2 u^2(y)dy - \int_2 u_{RMS}^2(y)dy - \int_2 (v_{RMS}^2(y) - \Delta P)dy\right) \quad \text{(A21)}$$

where ΔP is the pressure difference between the freestream pressure for surface (1) and (2). For this work, that pressure difference is significant since the measurements do not extend to where the freestream returns to the upstream speed. ΔP is found using the Bernoulli Equation by:

$$\Delta P = \frac{\rho}{2}({U_{up}}^2 - {U_\infty}^2) \quad \text{(A22)}$$

Note that ΔP is a constant. Finally the force coefficient is:

$$C_{FP} = \frac{2}{c}\left(\int\left(\frac{u(y)}{U_{up}}\right)\left(\frac{u(y)}{U_{up}} - 1\right)dy + \int\frac{u_{RMS}^2(y)}{U_{up}^2}dy - \int\frac{(v_{RMS}^2(y) - \Delta P)}{U_{up}^2}dy\right) \quad \text{(A23)}$$